

**Magneto-Transport
Investigations on
Multi-Electron Quantum Dots:
Coulomb Blockade, Kondo Effect,
and Fano Regime**

Vom
Fachbereich Physik an der Universität Hannover
zur Erlangung des Grades
Doktor der Naturwissenschaften
- Dr. rer. nat. -
genehmigte Dissertation
von

Dipl.-Phys. Claus Fühner
geboren am 6. Dezember 1971 in Meppen

2002

Referent: Prof. Dr. R. J. Haug
Koreferent: Prof. Dr. M. Oestreich

Tag der Promotion: 25.11.2002

As far as the laws of mathematics refer to reality, they are not certain, and as far as they are certain, they do not refer to reality.

A. Einstein

Abstract

This thesis covers different regimes of electronic transport through single-electron tunnelling transistors (SETs). The SETs are fabricated in split-gate technique from a GaAs/AlGaAs heterostructure using a combination of optical and electron beam lithography. We employ electronic transport measurements at low temperatures. The conductance of the samples exhibits Coulomb, Kondo and Fano resonances depending on the tunnel coupling between quantum dot and leads.

The Coulomb regime is characterized by a weak tunnel coupling between quantum dot and leads. We determine the relevant parameters of our samples by temperature dependent and nonlinear conductance measurements. We find a number of electrons confined on the quantum dot of $N \approx 150$. This number is varied by $\Delta N = 75$ by tuning the plunger gate voltage. After finishing the characterization we employ magneto-transport spectroscopy. In high magnetic fields, the electrons on the quantum dot are organized in Landau levels similar to the quantum Hall effect in two-dimensional systems. After isolating the influence of the emitter Fermi level on the magneto-conductance we observe redistributions of electrons between the Landau levels as a function of magnetic field. We determine the filling factor of the quantum dot from these measurements. After reaching filling factor one at high magnetic fields, the redistribution of charge between Landau levels stops and we observe infrequent transitions between maximum and lower density droplet states. We observe an effective spin polarization of the emitter leading to a modulation of the conductance as a function of the electron spin.

At strong coupling between dot and leads the Kondo effect dominates transport. This phenomenon gives rise to a finite conductance in Coulomb-blockade valleys with a characteristic temperature dependence. It is due to correlations between an unpaired electron on the quantum dot and electrons in the leads. We investigate the Kondo effect in our SETs as a function of bias voltage and temperature and find the characteristic fingerprints. We observe a modulation of the Kondo effect as a function of magnetic field B and electron number N . Between filling factor 3 and 4 this modulation leads to an extremely regular, chessboard-like magneto-conductance. The Kondo effect is found to be modulated by the addition of single magnetic flux quanta to the

quantum dot. In contrast to previous studies we observe a Kondo effect in high- as well as in low-conductance tiles of the chessboard-like magneto-conductance. The modulation is given only by its splitting. The structure of the Kondo effect in this regime is more complicated than expected for a single unpaired electron with spin $1/2$, demonstrating that the electronic state of the dot is governed by many-particle correlations. In addition, we have shown for the first time that the modulated Kondo effect vanishes when the emitter becomes spin polarized.

We have demonstrated that a SET may exhibit tunable Fano resonances instead of Coulomb or Kondo resonances. In our sample these resonances were exceptionally stable and reproducible which enabled their thorough investigation. We interpret our Fano resonances in a simple two-channel model as an interference phenomenon between a resonant transmission channel based on Coulomb blockade and an alternative, non-resonant conductance channel. We quantitatively analyze the properties of both channels as functions of temperature, magnetic field, plunger gate and bias voltage. This analysis confirms that the resonant channel is due to Coulomb blockade. The non-resonant channel depends on the plunger gate voltage in a non-continuous way and is not influenced by the other parameters. We find the interference pattern to be robust with respect to decoherence introduced by a finite bias voltage or an increased temperature $T \leq 1$ K. We discuss the origin of the non-resonant transmission channel and find two alternative explanations. It is either due to a second subband in the heterostructure or due to a rapid ballistic traversal of the quantum dot not respecting charging energy. The latter could be a consequence of the low charging energy in the extremely strong coupling regime.

The observation of Coulomb, Kondo and Fano regimes in a single device demonstrates the wide and continuous tunability of split-gate SETs. This has allowed to control and study a correlated, mesoscopic many-electron system. After being the objective of active research for the last years, in the future the Kondo effect might increasingly become a tool to gain further insight into the structure of such systems. The Fano regime of SETs has been neglected for a long time but might open new opportunities to study the transmission phase of electronic wave functions in addition to the established amplitude measurements.

Zusammenfassung

In dieser Arbeit werden verschiedene elektronische Transportregimes in Einzelelektronen-Tunneltransistoren (engl.: single-electron tunnelling transistors, kurz SETs) untersucht. Die Split-Gate SETs werden mit einer Kombination aus optischer und Elektronenstrahl-Lithographie aus einer GaAs/AlGaAs Heterostruktur hergestellt und bei tiefen Temperaturen vermessen. Abhängig von der Stärke der Tunnelkopplung zwischen dem Quantenpunkt und seinen Zuleitungen werden in der Leitfähigkeit Coulomb-, Kondo- und Fanoresonanzen beobachtet.

Das Coulomb-Regime ist durch eine schwache Tunnelkopplung zwischen Quantenpunkt und Zuleitungen gekennzeichnet. In diesem gut verstandenen Transportregime werden zunächst die relevanten Probenparameter durch temperaturabhängige und nichtlineare Messungen bestimmt. Die Anzahl der Elektronen auf dem Quantenpunkt liegt bei $N \approx 150$ und kann im gesamten Gatespannungsbereich um $\Delta N = 75$ variiert werden. Nach der Charakterisierung wird der Quantenpunkt in Magneto-Transportmessungen spektroskopisch untersucht. Analog zum Quanten-Halleffekt in zweidimensionalen Systemen bilden sich innerhalb des Quantenpunktes Landauniveaus. Nach Isolation des Einflusses des Emitter-Ferminiveaus wird eine Umverteilung von Ladungen zwischen den Landauniveaus in Abhängigkeit vom Magnetfeld beobachtet und daraus der Füllfaktor des Quantenpunktes bestimmt. Die Umverteilung von Elektronen zwischen den Landauniveaus endet mit Erreichen des *Maximum density droplet*-Zustandes, der bei weiter erhöhtem Magnetfeld in *Lower density droplet*-Zustände zerfällt. Außerdem konnte für bestimmte Magnetfelder eine effektive Spinpolarisation des Emitters beobachtet werden, die zu einer Modulation der Probenleitfähigkeit in Abhängigkeit vom Elektronenspin führt.

Eine erhöhte Kopplung zwischen Quantenpunkt und Zuleitungen führt zur Beobachtung eines Kondoeffektes, hervorgerufen durch die Streuung von Zuleitungselektronen an einem einzelnen, ungepaarten Spin auf dem Quantenpunkt. Vorspannungs- und Temperaturabhängigkeit des Kondoeffektes werden eingehend untersucht. Bei endlichen Magnetfeldern B wird zwischen den Füllfaktoren 3 und 4 eine Modulation dieses Effektes in Abhängigkeit von B und der Anzahl N der Elektronen auf dem Quantenpunkt beobachtet. Der resultierende Verlauf der Leitfähigkeit erinnert als Funktion von B und N an ein

Schachbrettmuster. Dessen Periode in Richtung des Magnetfeldes konnte zu einem magnetischen Flussquant bestimmt werden. Zwischen hellen und dunklen Feldern des Schachbrettmusters wird im Gegensatz zu früheren Untersuchungen nicht das Auftreten des Kondoeffektes selbst sondern seine Aufspaltung moduliert. Dies deutet darauf hin, dass am Zustandekommen des Kondoeffektes auf dem Quantenpunkt statt eines einzelnen Elektrons ein korrelierter Vielelektronen-Zustand beteiligt ist. Zudem konnte erstmals gezeigt werden, dass der Kondoeffekt bei einer Spinpolarisation des Emitters verschwindet.

Bei noch weiter erhöhter Kopplung zwischen Quantenpunkt und Zuleitungen schließlich treten Fanoresonanzen an die Stelle der Coulomb- bzw. Kondoresonanzen. Diese konnten eingehend untersucht werden, da sie in den verwendeten Proben außerordentlich stabil und reproduzierbar sind. Sie werden im Rahmen eines einfachen Zweikanal-Modells als Interferenz von einem resonanten, auf Coulombblockade basierenden Transmissionskanal mit einem zweiten nichtresonanten Kanal interpretiert. Eine quantitative Analyse der Eigenschaften beider Kanäle in Abhängigkeit von Temperatur, Magnetfeld, Gate- und Vorspannung bestätigt, dass der resonante Kanal auf Coulombblockade basiert. Der nichtresonante Kanal zeigt ein diskontinuierliches Verhalten in Abhängigkeit von Gatespannung und Magnetfeld, von den anderen Parametern wird er nicht beeinflusst. Die Interferenz beider Kanäle ist stabil gegenüber Dekohärenz durch eine endliche Vorspannung oder eine erhöhte Temperatur $T \leq 1$ K. Aus einer abschließenden Diskussion des Ursprungs des zweiten Transmissionskanals gehen eine Besetzung eines zweiten Subbandes in der Heterostruktur und ein schnelles ballistisches Durchqueren des Quantenpunktes als wahrscheinliche Kandidaten hervor.

Die Beobachtung von drei verschiedenen Transportregimes in einer einzigen Probe demonstriert die weite und kontinuierliche Einstellbarkeit der verwendeten SETs. So konnte ein korreliertes mesoskopisches Vielelektronen-System kontrolliert und untersucht werden. Nachdem der Kondoeffekt in den letzten Jahren selbst Gegenstand aktiver Forschung gewesen ist, könnte er sich in Zukunft zu einem Analysewerkzeug für solche Systeme entwickeln. Das Fano-Regime von SETs ist lange vernachlässigt worden, könnte aber nun neue Möglichkeiten zur Messung der Phase elektronischer Wellenfunktionen in Ergänzung zu den etablierten Amplitudenmessungen eröffnen.

Keywords

single electron tunnelling transistor, Kondo effect, Fano resonances

Schlagworte

Einzelelektronen-Tunneltransistor, Kondoeffekt, Fanoresonanzen

Contents

1	Introduction	1
2	Quantum dots and single-electron tunnelling	5
2.1	Quantum dots	6
2.1.1	Charge quantization	7
2.1.2	0D-Quantization: Electronic level spectrum	7
2.1.3	Quantum dot Hamiltonian	9
2.1.4	Experimental realizations of semiconductor quantum dots	10
2.2	Quantum dots in high magnetic fields	11
2.2.1	Free electron in a magnetic field	11
2.2.2	Confined electron in a magnetic field: Fock-Darwin spectrum	12
2.2.3	Interacting and confined electrons in a magnetic field	14
2.3	Single-electron tunnelling	17
2.3.1	Electrostatic capacitance model	17
2.3.2	Constant-interaction model	19
2.3.3	Coulomb-blockade measurements	20
2.3.4	Excitation spectroscopy	24
2.3.5	Cotunnelling	26
2.4	Coulomb-resonance lineshape	27
3	Experiment	31
3.1	Heterostructures	31
3.2	Patterning of the 2DES	33
3.3	Measurement setup	34

4	Coulomb-blockade regime	37
4.1	Linear conductance measurements	37
4.2	Temperature dependence of Coulomb oscillations	39
4.3	Nonlinear conductance measurements	41
4.3.1	Charging energy and total capacitance	42
4.3.2	Determination of dot-gate and dot-contact capacitances	43
4.3.3	Excitation spectrum	44
4.4	Magneto-transport spectroscopy	46
4.4.1	Magneto-oscillations of the emitter Fermi level	48
4.4.2	Spectroscopy of the quantum dot	50
4.4.3	Filling factor of the quantum dot	56
4.4.4	Maximum density droplet	59
4.5	Conclusions	62
5	Kondo regime	65
5.1	Introduction to the Kondo effect	65
5.1.1	Low-temperature resistivity in the presence of magnetic impurities	66
5.1.2	Anderson impurity model in quantum dots	68
5.1.3	Estimation of the Kondo temperature	72
5.1.4	Kondo resonances with lifted degeneracy	73
5.1.5	Kondo effect for odd and even electron numbers	74
5.1.6	Deviations from the spin-1/2 Anderson model	75
5.2	Quantum dot parameters	76
5.3	Kondo effect at zero magnetic field	77
5.3.1	Nonlinear conductance	77
5.3.2	Temperature dependence	79
5.4	Kondo effect at finite magnetic fields	82
5.4.1	Overview of the magneto-modulated Kondo conductance	82
5.4.2	Modulated Kondo effect at low magnetic fields	85
5.4.3	Modulated Kondo effect at high magnetic fields	87
5.5	Coulomb-peak positions and amplitudes in the Kondo regime	93
5.5.1	Absence of spin blockade	94
5.5.2	Spin blockade and vanishing Kondo effect	95

5.6	Conclusions	98
6	Fano regime	101
6.1	Introduction to Fano resonances	101
6.1.1	General properties of Fano resonances	104
6.1.2	Fano resonances in a realistic SET experiment	105
6.1.3	Two-channel model of Fano resonances in SETs	106
6.2	Measurements on a quantum dot in the Fano regime	110
6.2.1	Tuning the SET into the Fano regime	110
6.2.2	Analysis of the Fano lineshapes	111
6.2.3	Nonlinear and temperature dependent conduc- tance	115
6.2.4	Tuning Fano resonances in small magnetic fields	123
6.3	Background transmission channel	126
6.3.1	Model calculations of Fano resonances	126
6.3.2	Origin of the non-resonant transmission channel	130
6.4	Conclusions	136
7	Summary and conclusions	137
A	Symbols and notations	141
B	Sample fabrication and handling	145
B.1	Electron beam lithography	146
B.2	Mounting	149
B.3	Sample handling	149
C	Parameters of heterostructure 1129	151
C.1	Characterization of the heterostructure	151
C.2	Self-consistent Poisson-Schrödinger band structure cal- culation	152
D	Additional data on sample 1129-8-7.3	155
D.1	Coulomb peaks in high magnetic fields	155
D.2	Transitions in the chessboard Kondo conductance	155
	Bibliography	160

List of Tables

4.1	Data extracted from Coulomb blockade for two characteristic SETs	62
4.2	Results from magneto-transport spectroscopy	63
6.1	Parameters from the nonlinear conductance diamonds in the Fano regime	119
C.1	Parameters for the band structure calculation	152

List of Figures

1.1	Coulomb, Kondo and Fano resonances in quantum dots	3
2.1	A quantum dot embedded between two reservoirs	6
2.2	Excitation spectrum	8
2.3	Experimental realizations of semiconductor quantum dots	10
2.4	Fock-Darwin spectrum	13
2.5	Charge density of a quantum dot in high magnetic fields	15
2.6	Formation of edge states	16
2.7	Electrostatic capacitance model of a quantum dot	18
2.8	Scheme of Coulomb blockade	21
2.9	Coulomb-blockade diamonds schematically	23
2.10	Scheme of excitation spectroscopy	25
2.11	Cotunnelling	26
2.12	Temperature dependent Coulomb oscillations	27
2.13	Coulomb-peak height and width	28
3.1	Layer sequence of heterostructure 1129	32
3.2	SEM micrograph and simulated potential of the sample	33
3.3	Measurement setup	35
4.1	Coulomb-blockade oscillations	38
4.2	Temperature dependent Coulomb oscillations	40
4.3	Evolution of lever arm and intrinsic linewidth with temperature	41
4.4	Coulomb-blockade diamonds	42
4.5	Slopes of the Coulomb diamonds	44
4.6	Excitation spectrum in Coulomb diamonds	45

4.7	Magneto-conductance and Hall measurements up to $B = 13$ T	47
4.8	Steps in the resonance voltage V_G due to jumps in the 2DES chemical potential	49
4.9	2DES chemical potential dependent on filling factor	50
4.10	Coulomb-peak position and amplitude variation in B	51
4.11	Coulomb-peak position and amplitude variation in B	52
4.12	Scheme of the magneto-conductance in a quantum dot	53
4.13	Effective spin polarization of the emitter	54
4.14	Quantum dot magneto-conductance for a spin polarized emitter	55
4.15	Coulomb-peak positions and amplitudes at $V_G \sim -1.1$ V	57
4.16	Coulomb-peak positions and amplitudes at $V_G \sim -0.5$ V	58
4.17	Dots at different filling factors, MDDs	60
4.18	Maximum density droplet	61
5.1	Kondo effect in magnetic alloys	66
5.2	Sketch of the Anderson impurity model	68
5.3	Schematic spectral density in the Anderson impurity model	71
5.4	Dependence of the Kondo temperature T_K on Anderson model parameters	72
5.5	Kondo resonance with lifted degeneracy	74
5.6	Schematic energy diagram of the quantum dot used in the Kondo experiments	77
5.7	Coulomb diamonds exhibiting a Kondo resonance	78
5.8	Temperature dependence of a Kondo resonance	80
5.9	Linear Kondo conductance in a magnetic field	83
5.10	Tile periodicity in magneto-conductance	84
5.11	Kondo effect and magneto-conductance: Honeycomb regime	86
5.12	Kondo effect and magneto-conductance: Regular chessboard regime	88
5.13	Kondo effect in nonlinear magneto-conductance	89
5.14	Schematic nonlinear conductance in the chessboard regime	90
5.15	Temperature dependent linear and nonlinear Kondo conductance	92
5.16	Temperature dependent chessboard Kondo conductance	93

5.17	Coulomb-peak position and amplitude in the Kondo regime: Absence of spin blockade	94
5.18	Coulomb-peak position and amplitude in the Kondo regime: Spin blockade	95
5.19	Modulation of the Kondo effect by spin polarizing the emitter	97
5.20	Suppression of the Kondo effect due to a spin-polarized emitter	98
6.1	Scheme of Fano resonances in two-channel scattering . .	103
6.2	Interference of two transmission channels leads to Fano resonances	107
6.3	Dependence of the Fano symmetry parameter q on back- ground phase shift φ_{nr}	109
6.4	Overview of Fano resonances in linear conductance . . .	111
6.5	Fits to all Fano resonances from regions (1)–(3)	112
6.6	Parameters of the two-channel Fano model determined from fits	114
6.7	Fano resonances with asymmetry $q < 0$	115
6.8	Symmetric Fano anti-resonances, $q = 0$	117
6.9	Fano resonances with asymmetry $q > 0$	118
6.10	Temperature dependent Fano anti-resonances	121
6.11	Two-channel model parameters from temperature de- pendent Fano anti-resonances	122
6.12	Fano resonance amplitudes as a function of temperature	123
6.13	Fano anti-resonances in a small magnetic field	124
6.14	Evolution of Fano resonances in a magnetic field	125
6.15	Model calculation (1) of Fano (anti-) resonances	128
6.16	Model calculation (2) of Fano (anti-) resonances	129
6.17	Simulated band structures showing an occupation of the second subband	133
6.18	Distances between resonances in the Fano regime	134
6.19	Rapid ballistic electron trajectories traversing the dot . .	135
B.1	Optical lithography mask	145
B.2	Electron beam lithography patterns	146
B.3	Overview of the sample	147

B.4	Sample in a chip-carrier	149
B.5	Sample destroyed by electrostatic discharge	150
C.1	Quantum Hall effect in heterostructure 1129	151
C.2	Self-consistent band structure and wave functions in heterostructure 1129	153
D.1	Coulomb-peak positions in high magnetic fields	156
D.2	Transitions between chessboard Kondo tiles	157
D.3	Analysis of the transition between chessboard Kondo tiles	159

1 Introduction

To experimentally study quantum mechanics at a basic level, physicists have always been seeking for quantum systems which could be manipulated in a well-defined and controlled way. Quantum dots [1, 2] are nearly ideal candidates for such systems: They confine typically between one and a few hundred electrons in a region small enough to make quantization effects a prominent feature similar to the situation in *real* atoms. Therefore quantum dots are often called *artificial* atoms [3]. Compared to their real counterparts they offer the advantage of greater tunability. The experimentalist is able to virtually freely design the electronic confinement potential either when fabricating the devices or – depending on the type of quantum dot used – while performing the experiment. The level spectrum as well as the number of the confined electrons and their spin are tuned by external parameters like gate voltages and magnetic field. This fulfills the physicists’ desire to engineer quantum states and might even lead to the realization of powerful quantum computers [4, 5, 6].

A suitable material in which to realize quantum dots are GaAs/Al-GaAs semiconductor heterostructures [7]. These enable the fabrication of very clean, defect-free two-dimensional electron systems with a large de-Broglie wavelength of several ten nanometers [8, 9]. The comparably large electronic wavelength allows to still consider structures of about a hundred nanometers as zero-dimensional and dot-like. It puts the controlled fabrication of zero-dimensional structures at the very edge of modern lithography, making the fabrication process a challenging but feasible task. This field is at the frontier of both, technology and science alike.

Optical as well as electronic transport methods provide ways to probe and manipulate wave function and level spectrum of quantum

dots. While optical experiments focus on isolated quantum dots, transport experiments are applied to single-electron tunnelling transistors (SETs). The latter devices consist of a quantum dot tunnel coupled to two electron reservoirs. While transport is dominated by properties of the pure quantum dot in the so-called Coulomb regime at weak tunnel coupling, additional correlation phenomena at stronger coupling lead to new transport regimes due to the increased overlap of dot and reservoir wave functions.

The Kondo effect [10] in SETs [11, 12] is an example for such a correlation phenomenon studied in transport experiments [13, 14, 15, 16]. At sufficiently low temperatures, the formation of spin singlets between an unpaired electron on the quantum dot and reservoir electrons gives rise to distinct features in the conductance of SETs. Instead of a single unpaired spin, more complicated states on the dot might enable the emergence of more sophisticated Kondo effects [17, 18].

Another transport regime of strong tunnel coupling between dot and leads is the Fano regime [19, 20, 21]. Here the coupling is so large that the tunnelling barriers are nearly transparent, and an alternative, non-resonant transport channel emerges in addition to the resonant Coulomb-blockade channel. The interference of electronic wave functions transmitted through both channels is again reflected in characteristic features of transport measurements.

Outline

In the present work quantum dots are investigated in the Coulomb, Kondo and Fano regimes. Figure 1.1 illustrates their distinction by the strength of the tunnel coupling between dot and leads:

- The **Coulomb-blockade regime** is characterized by a weak tunnel coupling between dot and leads. The electronic multi-particle states on the quantum dot are virtually undisturbed by the presence of the leads.
- The **Kondo regime** at strong tunnel coupling is governed by correlations between the electrons on the dot and in the leads, leading to transport even in Coulomb-blockade valleys.

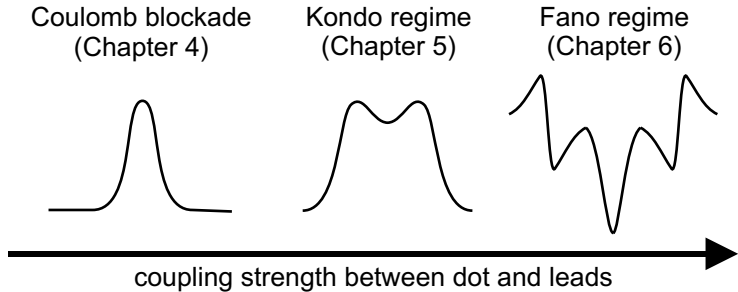


Figure 1.1: In this work, quantum dots are studied in three different transport regimes. Coulomb, Kondo and Fano resonances – depicted here with their characteristic V_G - G -lineshapes – are observed in transport measurements at different tunnel couplings of a quantum dot to the leads.

- At further increased tunnel coupling the **Fano regime** is reached. Here a second transport channel through the dot is opened which interferes with the first channel.

In detail, this thesis is organized as follows:

Chapter 2 gives a concise introduction to single-electron transistors in the Coulomb-blockade regime. It focuses on those single-electron transport phenomena important to understand the other chapters. Special attention is paid to the electronic level spectrum of quantum dots in a magnetic field.

In **Chapter 3**, we give a brief outline of the fabrication and preparation of our single-electron tunnelling transistors. We introduce the measurement techniques employed to study electronic transport at low temperatures.

The quantum dots are investigated in the Coulomb-blockade regime in **Chapter 4**. First, we characterize our quantum dots in conventional linear and nonlinear conductance measurements. The temperature is varied to gain additional information on the involved energy scales. Then we examine the influence of a magnetic field on the emitter Fermi level and on the ground state of the interacting multi-electron system on the dot. We show that at certain magnetic fields transport depends

on the spin of the tunnelling electron. The results described in this chapter are essential for the interpretation of our further experiments.

The Kondo regime of a multi-electron quantum dot which is strongly tunnel coupled to leads is explored in **Chapter 5**. After an introduction to Kondo physics we experimentally characterize the Kondo effect found in our quantum dot at zero magnetic field. Finally we examine its modulation and modification due to a magnetic field. We demonstrate that the Kondo effect is suppressed if the emitter becomes spin polarized.

Chapter 6 is devoted to the Fano regime of quantum dots. After summarizing Fano theory, we develop a model to describe the formation of Fano resonances in a SET as interference of two transport channels. Our measurements are interpreted in terms of this model. We analyze the importance of decoherence introduced by a finite bias voltage or temperature. We investigate how the Fano resonances in our dot are influenced by a magnetic field. Finally, based on the previous results we discuss the origin of the second transport channel.

Chapter 7 gives a summary of the results and the most important conclusions.

2 Quantum dots and single-electron tunnelling

As quantum dots by now have been the objective of vivid interest for more than ten years, this work cannot examine every aspect of this field. This introductory chapter provides those properties and concepts of quantum dots which are relevant to the later experimental part. For more exhaustive reviews the reader is referred to the numerous books and papers on quantum dots: Ref. [1] covers nearly the complete topic and gives a good overview. The early experiments are described in Ref. [3]. Ref. [22] is very helpful in analyzing experimental data while Ref. [23] focuses extensively on the electrostatics of quantum dots. Ref. [24] provides a selection of important papers on the field. A less specialized, broader audience is addressed in References [25, 26, 27].

This chapter focuses on the conventional regime of *weak* coupling between quantum dot and leads. After introducing the basic concepts of charge- and 0D quantization we discuss the Hamiltonian of an isolated quantum dot. Thereafter some experimental realizations of quantum dots are compared. We summarize the influence of a magnetic field on dots. Moreover, the electrostatic capacitance and constant-interaction models are introduced. The sections on Coulomb blockade, excitation spectroscopy and cotunnelling are of particular importance for the later analysis of our experimental data, as is the final section on the temperature dependence of Coulomb-resonance lineshapes.

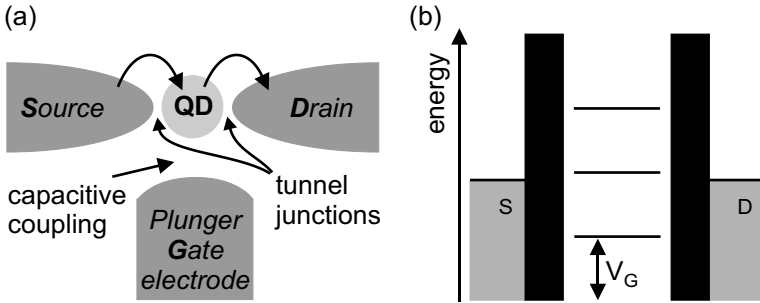


Figure 2.1: A quantum dot embedded between two reservoirs and controlled via a gate electrode: (a) Electrons tunnel from the *source* reservoir to the quantum dot *QD* and from there into the *drain* contact. The island energy levels are capacitively controlled using a plunger gate electrode *G*. (b) Energy diagram of a quantum dot with its levels tuned by the plunger gate voltage V_G . High tunnelling barriers (black) separate the dot from reservoirs (grey) with chemical potentials μ_S and μ_D .

2.1 Quantum dots

Quantum dots are small, conducting regions defined in insulating surroundings. On these islands, electrons are confined. In this aspect, quantum dots closely resemble atoms with their electrons confined in the attractive potential of their nuclei. Quantum dots are also named *artificial atoms* because of this similarity [25]. Unlike real atoms, the spectra of quantum dots cannot only be probed and manipulated by adsorption and emission of electromagnetic radiation but also in transport experiments. Electronic leads tunnel coupled to a quantum dot allow to probe its spectrum in current-voltage measurements. Such a system is depicted in Figure 2.1(a): The quantum dot is embedded between two leads named *source* and *drain*. These act as electron reservoirs and are tunnel coupled to the island. An additional "plunger" gate electrode capacitively coupling to the quantum dot is used to electrostatically manipulate the dot energy levels. Hence, as the conductance can be controlled via a gate electrode, this setup is called

single-electron transistor (SET).

A typical energy diagram of a SET is shown in Figure 2.1(b) with some discrete levels in the quantum dot and continuous spectra in the source and drain reservoirs. The discreteness of quantum dot spectra will become clear in the next sections. Here, it is important to understand that the plunger gate is used to shift the internal dot levels.

2.1.1 Charge quantization

Assuming that there is no coupling between the quantum dot island and its surroundings, it contains an integer number of electrons and its charge Q is quantized, $Q = Ne$. At finite tunnel coupling to the leads, charge quantization still holds if two requirements are met:

1. To put an extra charge e on an island with capacitance C , the charging energy $U = e^2/C$ has to be overcome. For charge quantization the thermal energy $k_B T$ must not exceed this Coulomb energy,

$$e^2/C \gg k_B T. \quad (2.1)$$

2. The tunnel barriers between dot and leads must be sufficiently opaque such that the electrons are located either on the dot or on the leads. Considering a tunnelling resistance R_t , a typical time to charge the island is $\Delta t = R_t C$. A typical energy scale is given by $\Delta E = U$. From Heisenberg's uncertainty relation $\Delta E \Delta t > \hbar$ a requirement for the tunnelling resistance is deduced:

$$R_t \gg \hbar/e^2. \quad (2.2)$$

To summarize, a quantum dot connected to leads shows charging effects if its charging energy is sufficiently large compared to temperature and if the coupling to the leads is weak enough. A small capacitance is realized by making the dot small. The coupling to the leads is adjusted in the fabrication process or can later be tuned in the experiment.

2.1.2 0D-Quantization: Electronic level spectrum

Quantum dots are generally very small with their dimensions as tiny as the Fermi wavelength. Hence they can be considered as zero-dimensional

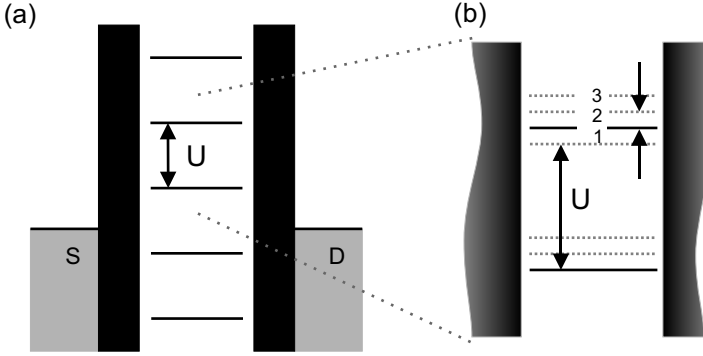


Figure 2.2: (a) Coulomb-blockade induced level spectrum of a quantum dot with charging energy U and (b) excitation spectrum with confinement-induced quantum mechanical levels ε_i spaced $\Delta\varepsilon$.

objects. Electrons residing on the dot have a discrete energy level spectrum ε_i . This quantum mechanical quantization is different from the classical charge quantization discussed in the previous section. In the dots examined in this work, it is typically much smaller than the Coulomb charging energy U .

For a two-dimensional harmonic confinement potential with a classical radius r of the ground state wave function the internal level spacing $\Delta\varepsilon_i = \varepsilon_{i+1} - \varepsilon_i$ is constant, and $\Delta\varepsilon_i = \Delta\varepsilon$ (m^* is the effective electron mass):

$$\Delta\varepsilon = \hbar\omega = \frac{2\hbar^2}{m^*r^2}. \quad (2.3)$$

In other confinement potentials the spacing is not necessarily constant, but the harmonic approximation still gives an estimate. The exact spectrum is given by the appropriate Hamiltonian. To add an extra electron onto the dot, not only Coulomb energy U but also the quantum mechanical ground state energy ε_i has to be overcome.

Figure 2.2 illustrates this situation: Around Coulomb-blockade induced levels with spacing U , electronic levels ε_i with a spacing $\Delta\varepsilon$ emerge.

2.1.3 Quantum dot Hamiltonian

In the regime of weak tunnel coupling between dot and leads the exact spectrum of a quantum dot is determined from its Hamiltonian. The leads in a SET are then described by a separate Hamiltonian which is not considered here. For stronger coupling interactions between dot and leads have to be taken into account (chapter 5). We will describe a weakly coupled quantum dot with N interacting electrons, each at position $\vec{\mathbf{r}}_i$, with momentum $\vec{\mathbf{p}}_i$ and spin $\vec{\mathbf{S}}_i$. The N -electron Hamiltonian \mathbf{H}_{QD} is composed of a sum over all single-electron energies plus a contribution from interaction:

$$\begin{aligned}
 \mathbf{H}_{\text{QD}} = & \sum_{i=1}^N \left[\underbrace{\frac{1}{2m^*} \left(\vec{\mathbf{p}}_i + e\vec{A}(\vec{\mathbf{r}}_i) \right)^2}_{\text{free electron}} + \underbrace{g\mu_B\vec{B} \cdot \vec{\mathbf{S}}_i}_{\text{Zeeman term}} + \underbrace{V_{ext}(\vec{\mathbf{r}}_i)}_{\text{confinement}} \right] \\
 & + \underbrace{\frac{e^2}{2} \sum_{i=1}^N \sum_{\substack{j=1 \\ j \neq i}}^N V_{ee}(\vec{\mathbf{r}}_i, \vec{\mathbf{r}}_j)}_{\text{interaction}}. \tag{2.4}
 \end{aligned}$$

The last term in the Hamiltonian contains the electron-electron interaction V_{ee} and accounts for the Coulomb charging energy U . The preceding sum over all N electrons represents single-particle contributions to the total energy, consisting of a free electron term, a Zeeman term and the confinement potential. The free electron term describes a free electron of charge e in an external magnetic field $\vec{B} = \nabla \times \vec{A}$. The Zeeman term with the Landé g-Factor g and Bohr's magneton μ_B gives the Zeeman energy of an electron in a magnetic field. V_{ext} is the external confinement potential. The electronic energy levels ϵ_i of a quantum dot with a given confinement potential can be determined from this Hamiltonian.

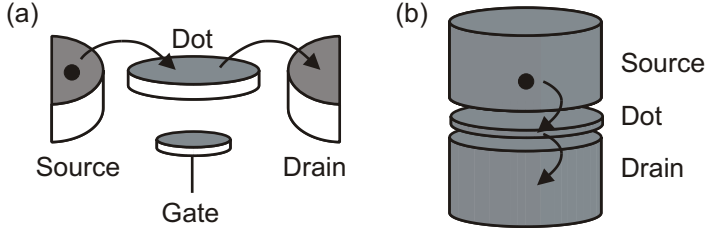


Figure 2.3: Realizations of semiconductor quantum dot in (a) lateral and (b) vertical geometry.

2.1.4 Experimental realizations of semiconductor quantum dots

Although the name "quantum dot" suggests exceedingly small, point-like spatial dimensions, typical semiconductor quantum dots are on the order of 100 nm in diameter. In comparison to metals with generally high electron densities, semiconductors contain orders of magnitude less free electrons. Islands of the size given above may contain only a few hundred or even less electrons. Thus semiconductor quantum dots consist of only very few relevant electrons and single-electron effects become prominent.

Whether the electronic level spectrum is discrete or not depends – among other parameters – on the size of the devices as compared to the Fermi wavelength. The Fermi wavelength in semiconductors is greatly reduced compared to metals.

However, the first quantum dots fabricated and examined in a controlled way were metallic SETs [28], where due to the small Fermi wavelength the electronic level spectrum was continuous. The controlled fabrication of semiconductor quantum dots was achieved a few years later [29, 30].

In experimental realizations, semiconductor quantum dots usually consist of islands which are disc shaped. Based on the direction of the current relative to the disc, they are classified into two groups, namely lateral and vertical structures. This is illustrated in Figure 2.3. While vertical dots are usually smaller and contain less electrons compared to lateral ones [30, 2], their tunnel coupling to the leads is adjusted already

in the fabrication process. Thereafter it is fixed. Lateral dots provide a better tunability in experiments by allowing the tunnel barriers to be varied.

The quantum dots examined in this work are lateral devices based on two-dimensional electron systems in GaAs/AlGaAs semiconductor heterostructures. The de Broglie wavelength of the free electrons in the heterostructures is very large, typically ~ 40 nm, and thus comparable to the spatial dimensions accessible with modern lithography. Therefore the dots can be fabricated small enough for the energy levels to become quantized.

2.2 Quantum dots in high magnetic fields

In this section, we focus on the influence of a magnetic field B on quantum dots. Magnetic fields are used in the later experiments to tune the energy levels of dots. We first consider a free electron in a magnetic field, later confinement and interaction with other electrons are added. The latter resembles the situation described by the Hamiltonian in eq. 2.4.

2.2.1 Free electron in a magnetic field

This section describes a free electron in a magnetic field and neglects the confinement potential in a quantum dot which is added later. An electron in a magnetic field is forced on circular cyclotron orbits perpendicular to the magnetic field in classical physics. An exact solution of the problem is possible also in quantum mechanics, yielding energy eigenvalues [31]

$$\varepsilon_n = (n + 1/2) \hbar\omega_C, \quad n = 0, 1, 2, \dots, \quad (2.5)$$

with Landau quantum number n and cyclotron frequency

$$\omega_C = \frac{eB}{m^*}. \quad (2.6)$$

The z degree of freedom parallel to the magnetic field has been neglected because in this work only quantum dots embedded in two-dimensional electron systems and in a perpendicular magnetic field are

considered (chapter 3.1). The Landau levels are equally spaced with an energy separation $\hbar\omega_C$ proportional to the magnetic field. Each Landau level is n_L -fold degenerate (g_S is the degeneracy due to spin),

$$n_L = g_S \cdot \frac{eB}{h}. \quad (2.7)$$

A characteristic length scale in this regime is the magnetic length

$$l_B = \sqrt{\frac{\hbar}{eB}} \quad (2.8)$$

which describes the classical cyclotron radius in $r_n = \sqrt{(2n+1)} \cdot l_B$ and thus gives the order of the extent of the electronic wave function.

To take into account the electron spin, eq. 2.5 is extended by a Zeeman contribution:

$$\varepsilon_{n,S_z} = (n + 1/2) \hbar\omega_C + g\mu_B B S_z, \quad S_z = \pm 1/2. \quad (2.9)$$

In presence of a magnetic field, spin degeneracy is lifted and each Landau level splits into two. This is considered in the definition of the filling factor ν which describes the number of occupied Landau levels. With an electron density n_e and a degeneracy per spin-split Landau level $n_L = eB/h$ we get:

$$\nu = \frac{n_e}{n_L} = \frac{n_e h}{eB}. \quad (2.10)$$

This framework describes one free electron in a magnetic field. In the next section we will consider the influence of a confinement potential in a quantum dot.

2.2.2 Confined electron in a magnetic field: Fock-Darwin spectrum

To add external confinement to the free electron spectrum from eq. 2.9, a smooth, circularly symmetric confinement potential $V_{ext}(r)$ varying slowly on the scale of variations of the electronic wave function, l_B , is considered (Thomas-Fermi approximation):

$$\varepsilon_{n,S_z,m} = (n + 1/2) \hbar\omega_C + g\mu_B B S_z + V_{ext}(r_m). \quad (2.11)$$

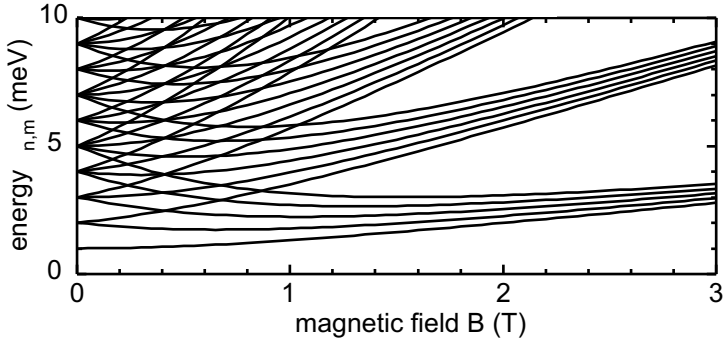


Figure 2.4: Fock-Darwin spectrum of a single particle in a harmonic potential, $\omega_0 = 1$ meV.

In addition to Landau-level index n and spin S_z an angular momentum quantum number m was introduced.

A common approximation to quantum dot confinement potentials is the circularly symmetric harmonic confinement,

$$V_{ext}(r) = (1/2)m^*\omega_0^2 r^2.$$

For this confinement, eq. 2.11 was solved by Fock and Darwin [32, 33]. Neglecting the Zeeman term which is trivial they evaluated

$$\varepsilon_{n,m} = (2n + 1 + |m|)\sqrt{(\hbar\omega_0)^2 + (\hbar\omega_C/2)^2} + (m/2)\hbar\omega_C.$$

The Fock-Darwin spectrum for an electron in GaAs with $\omega_0 = 1$ meV is shown in Figure 2.4. For low magnetic fields, frequent level crossings are observed, whereas for high magnetic fields Landau quantization dominates the confinement potential and the asymptotic form $\varepsilon_{n,m} = (n + 1/2 + (|m| - m)/2)\hbar\omega_C$ is found. To determine energy levels ε_i in more realistic confinement potentials sophisticated numerical calculations are necessary.

This single-particle description of a quantum dot is adequate for structures containing only very few electrons. It is often applied to vertical quantum dots [2]. However, it neglects Coulomb interaction which strongly alters the energy spectrum in lateral multi-electrons quantum dots considered in this work [34].

2.2.3 Interacting and confined electrons in a magnetic field

In extension to the single-particle description developed in eq. 2.11 now interactions between the confined electrons are considered. This problem needs a self-consistent treatment. The total energy of all N electrons on the quantum dot is given by

$$\begin{aligned}
 E_N &= \sum_n \sum_{S_z} \int d^2r \rho_{n,S_z}(r) \cdot ((n + 1/2) \hbar\omega_C + g\mu_B B S_z) \\
 &+ \int d^2r \rho(r) \cdot V_{ext}(r) \\
 &+ \frac{1}{2} \int d^2r \int d^2r' \rho(r)\rho(r')V_{ee}(r, r')
 \end{aligned} \tag{2.12}$$

with $\rho_{n,S_z}(r)$ the electron density in Landau level n , $\rho(r)$ the total electron density, $V_{ext}(r)$ the bare confinement potential and $V_{ee}(r, r')$ the electron-electron interaction. The first two terms describe the energy of single electrons from the previous section while the last term accounts for their interaction. This equation is solved by minimizing E_N with respect to the charge distribution $\rho_{n,S_z}(r)$ under certain constraints. In the context of quantum dots this was first discussed by McEuen *et al.* [34]. In the following paragraphs we briefly discuss their results.

Charge density

A self-consistent solution of eq. 2.12 for a sufficiently high magnetic field B yields a charge distribution $\rho_{n,S_z}(r)$ as schematically depicted in Figure 2.5¹. Starting with an empty dot, first electrons are added to the dot centre where the external confinement potential has a minimum. Due to Coulomb interaction, subsequently added electrons cannot be added to the dot centre like the first ones. Instead they are placed in outer regions. Only when the first Landau level $n = 0$ is completely occupied, additional electrons are placed in the centre of the dot again and are added to Landau level $n = 1$. Therefore the large energy gap $\hbar\omega_c$ between first and second Landau level has to be

¹Zeeman energy is neglected in the following discussion for the sake of simplicity.

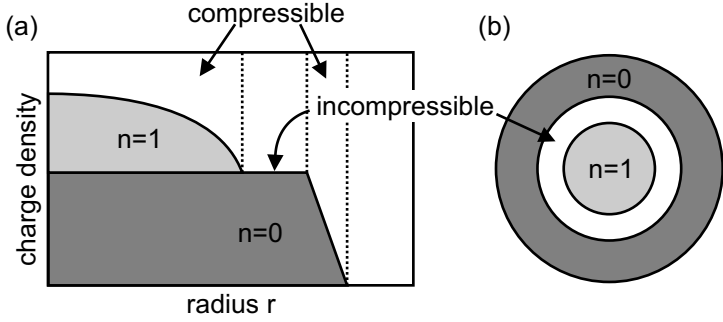


Figure 2.5: (a) Schematic self-consistent charge density $\rho(r)$ in a quantum dot in a high magnetic field. The Landau levels n form edge states in the external potential, resulting in compressible stripes separated by incompressible (insulating) regions. (b) Top view of a quantum dot with the stripes from (a).

overcome. This is the situation depicted in Figure 2.5. The interplay between Landau quantization, Coulomb repulsion and confinement potential leads to the constant charge density for the first Landau level $n = 0$ in the central dot region where the confining potential is completely screened and thus the effective potential is flat. At the edge of the dot, the confining potential cannot be completely screened any longer. Consequently, the charge density drops rapidly. In the Figure, the second Landau level $n = 1$ is not completely occupied and thus the charge density $\rho_{n=1}$ drops gradually from the centre to the outer dot regions.

Radial regions of constant charge density are named incompressible stripes. These never contain states at the Fermi level contributing to transport and are thus insulating. In contrast, the so-called compressible stripes characterized by a variable charge density completely screen the external potential. They are available for transport and therefore named metallic.

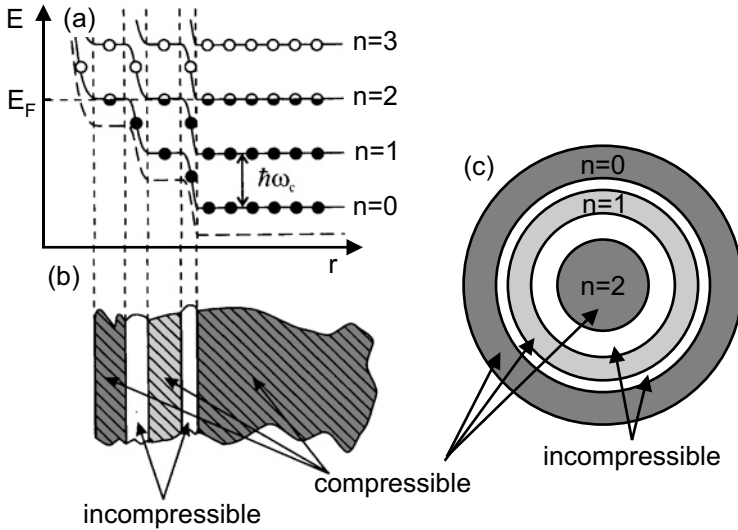


Figure 2.6: Confined, interacting electron systems form edge states at the border of the confining potential in a magnetic field: (a) Self-consistent energy scheme of different Landau levels resulting in compressible edge channels separated by incompressible regions as illustrated in (b) and (c).

Edge states

The compressible and incompressible stripes from the previous paragraph can be understood in terms of so-called edge states ([35, 36] and references therein). As sketched in Figure 2.6, the self-consistent energy of the electrons on every Landau level is – due to screening – flat in the central region of the dot and is bent upwards on the outer perimeter due to the external confinement potential. The resulting increase to the outer regions is stepwise, containing rising as well as flat segments. Every occupied Landau level has a region of flat potential at the Fermi level. The lower the Landau level index, the farther this region is located to the outer dot perimeter. It corresponds to a compressible, metallic stripe which screens the external potential due to

its variable charge density. The other regions are incompressible and insulating, not screening the external potential.

The interplay between discrete Landau levels and Coulomb interaction again has led to the formation of metallic regions on the quantum dot separated by insulating regions. This model of a quantum dot in a high magnetic field is comparable to the description of a bulk quantum Hall system.

2.3 Single-electron tunnelling

Until now, we have concentrated on the quantum dot itself and have neglected other components of a SET. In this section we will consider complete SETs with gates as well as source and drain contacts. After introducing some simple models, we will consider the transport properties of single-electron tunnelling transistors.

2.3.1 Electrostatic capacitance model

A simple electrostatic capacitance model for the total energy of the electrons on a quantum dot has proven very useful. This model completely neglects the internal structure of the dot. Thus it describes metallic quantum dots with a negligible level spacing very well but semiconductor quantum dots only roughly. It allows to determine the dependence of the dot energies on the external gate voltages (chapter 4.3). The pure capacitance model presented here will be extended to the constant-interaction model in chapter 2.3.2 to take into account the intra-dot level structure of semiconductor quantum dots.

All electrodes, gates as well as source and drain contacts, couple capacitively to the quantum dot as illustrated in the circuit diagram in Figure 2.7. The quantum dot and its surroundings can be interpreted as a network of capacitors. We consider a quantum dot on the potential V_{QD} . Its total charge Q_{QD} is linear in the voltage V_i of every gate $i \in \{S, D, G, \dots\}$:

$$Q_{QD} = \sum_{i=1}^M C_i (V_{QD} - V_i) = V_{QD} C_\Sigma - \sum_{i=1}^M C_i V_i. \quad (2.13)$$

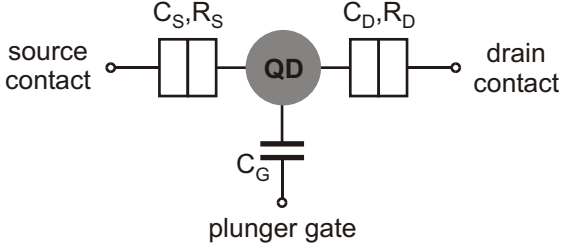


Figure 2.7: Circuit diagram of a quantum dot tunnel coupled to *source* and *drain* leads. The tunnel junctions are characterized by their capacitance $C_{S,D}$ and their resistance $R_{S,D}$. The gate electrode couples purely capacitively to the quantum dot with a capacitance C_G .

We have introduced the total capacitance C_Σ of the quantum dot:

$$C_\Sigma = \sum_{i=1}^M C_i. \quad (2.14)$$

The capacitances C_i describe the dependence of the dot charge on outer gate or contact voltages V_i : $C_i = \partial Q_{QD} / \partial V_i$. These coefficients depend on the relative geometric arrangement of dot and gates and on the dielectrics involved.

We assume an integer number of electrons N on the island and a charge $Q_{QD} = -eN$. Solving eq. 2.13 for V_{QD} allows to compute the total energy for N electrons on the island, E_N , depending only on the charge of the island $-eN$ and on the potentials of the external electrodes V_i :

$$\begin{aligned} E_N &= \int_0^{-eN} dQ_{QD} V_{QD}(Q_{QD}) \\ &= \frac{(eN)^2}{2C_\Sigma} - eN \cdot \sum_{i=1}^M \frac{C_i}{C_\Sigma} V_i. \end{aligned} \quad (2.15)$$

The first term regards the work necessary to load the island with N electrons. The second term accounts for the potential energy of N electrons in the gate-electrode potentials $\varphi_i = C_i / C_\Sigma \cdot V_i$.

The above formula allows to determine the energy needed to place an extra electron on the dot. This energy is equivalent to the chemical potential μ_N , the derivative of the total energy E_N with respect to particle number N :

$$\mu_N = \frac{\partial E_N}{\partial N} = \frac{e^2}{C_\Sigma} N - e \cdot \sum_{i=1}^M \frac{C_i}{C_\Sigma} V_i. \quad (2.16)$$

Thus to place an extra electron on the dot the charging energy

$$U = e^2/C_\Sigma \quad (2.17)$$

from the N electrons already on the dot has to be overcome (first term in eq. 2.16). Additionally, the extra electron has to be placed in the potentials of the gate electrodes $\varphi_i = C_i/C_\Sigma \cdot V_i$ (second term). For the addition of every further electron, the chemical potential on the dot increases accordingly. The chemical potential of the quantum dot is an important quantity because of the easy experimental accessibility of chemical potential differences. This will be discussed in the next section.

We point out that the part of the addition energy describing the influence of the external potentials does not depend on the electrons already on the dot (apart from small corrections due to a dependence of C_Σ on N). This allows to introduce a so-called lever arm α_i ,

$$\alpha_i = C_i/C_\Sigma, \quad (2.18)$$

to describe the influence of the voltage V_i on the corresponding electrostatic potential and hence on the chemical potential of the quantum dot, μ_N . In the approximation discussed here, the lever arm is a constant independent of other dot parameters, in particular independent of N . Varying the electrode voltage V_i linearly shifts the chemical potential on the dot by $-\alpha_i e V_i$.

2.3.2 Constant-interaction model

The capacitance model is extended to the constant-interaction model by considering the electronic level structure of a quantum dot. For the

N -electron dot an energy E_N^I is added to the energy E_N from eq. 2.15. E_N^I is given by a sum over the energies of occupied single-particle states ε_i . If the set I denotes the occupied levels, we get

$$E_N^I = \sum_{i \in I} \varepsilon_i. \quad (2.19)$$

The resulting total energy of the quantum dot is

$$E_{N,I} = E_N + E_N^I. \quad (2.20)$$

We have neglected many-particle effects like exchange interaction which would modify $E_{N,I}$. Also neglected are the dependencies of the parameters of the capacitance model on N . The parameters of the capacitance model depend on details of the electronic wave functions involved, another fact which is ignored. Despite its clear deficiencies, the constant-interaction model has proven highly useful in parameterizing the experimental data.

2.3.3 Coulomb-blockade measurements

From charge quantization it is clear that the chemical potential μ_N of a quantum dot (equation 2.16) has only discrete values. This leads to a discrete spectrum of the quantum dot as depicted in Figure 2.8(a). In the electrostatic capacitance model, this spectrum is moved up and down as a whole with any electrode voltage, e. g. $V_{i=G}$. The bias voltage $V_{SD} = (\mu_D - \mu_S)/e$ defines a *transport window*, a span of dot energies for which electronic transport is in principle possible. If the quantum dot actually is conducting or not depends on whether one of the discrete dot levels is within the transport window.

In situation (1) depicted in the figure, there are N electrons on the dot. The N th electron cannot tunnel from the dot to source or drain reservoirs because all levels up to the corresponding chemical potentials μ_S and μ_D are occupied. On the other hand, no electron can tunnel from the reservoirs to the dot, because the level μ_N is already occupied and the next available level μ_{N+1} lies energetically too high. Thus, whenever there is no dot level within the transport window, no transport of electrons between source and drain reservoir is possible.

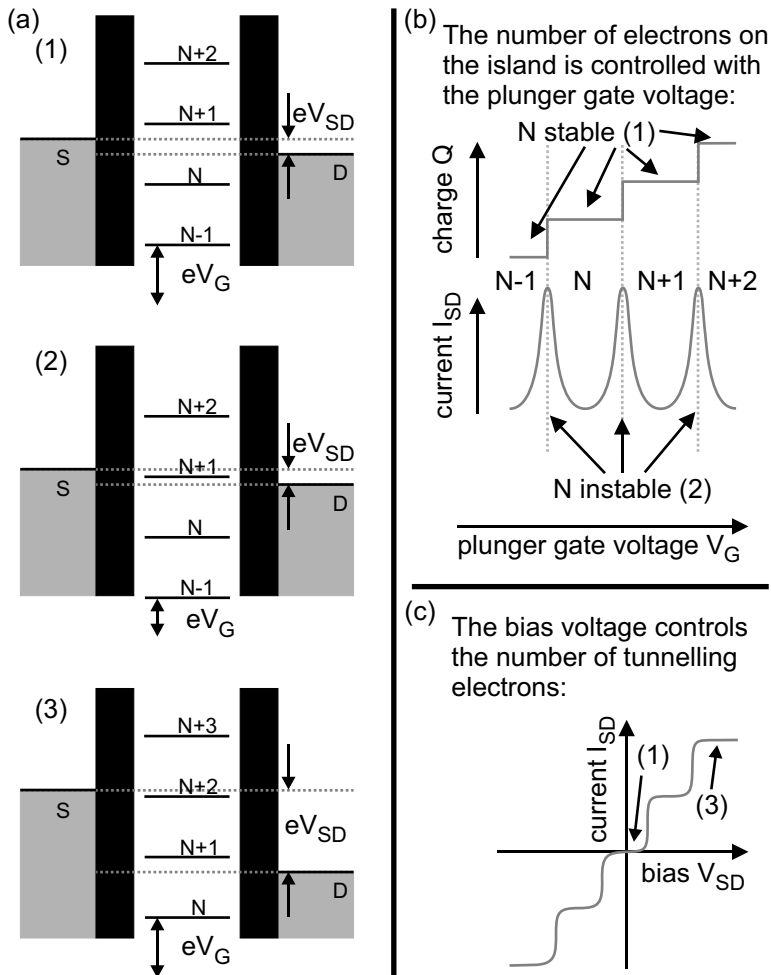


Figure 2.8: Coulomb blockade: Depending on plunger gate voltage, the situations on the quantum dot depicted in (a) lead to (b) alternating Coulomb resonances and blockade in the source-drain current for nearly zero bias voltage V_{SD} as a function of plunger gate voltage V_G . (c) A variation of the bias voltage V_{SD} results in the so-called Coulomb staircase.

Then the number of electrons on the dot is stable and the system is Coulomb blocked.

In situation (2) the plunger gate voltage has been adjusted so that the μ_{N+1} dot level is within the transport window: If the dot is occupied by N electrons, another electron can tunnel onto it from the source reservoir. Due to $\mu_{N+2} > \mu_S, \mu_D$ no $(N + 2)$ th electron can enter the dot as long as it is occupied by $N + 1$ electrons. Only when the $(N + 1)$ th electron has left the dot in a further tunnelling process another electron can enter. The $(N + 1)$ th electron can leave the dot into the drain reservoir because of $\mu_N + 1 > \mu_D$. In the situation (2) one transport channel from source to drain is open. The number of electrons on the dot fluctuates between N and $N + 1$, therefore this situation is named charge degeneracy.

Situation (3) is comparable to situation (2) except for the wider transport window. Here, two channels are available for transport giving rise to a higher dot conductance than in situation (1). The number of electrons on the dot fluctuates between N , $N + 1$ and $N + 2$.

In Figure 2.8(b), the dependencies of dot charge $Q = Ne$ and current on plunger gate voltage V_G are considered. Only small bias voltages V_{SD} comparable to situations (1) and (2) discussed above are regarded. At plunger gate voltages as in situation (1) no current flows through the dot and its charge is stable. For voltages leading to situation (2), the charge becomes instable. It can fluctuate by e . Then transport becomes possible, hence a Coulomb resonance is observed in the current. The width of the resonance is discussed in section 2.4. Due to the constant charging energy U , Coulomb oscillations are periodic in gate voltage.

Figure 2.8(c) depicts the current as a function of bias voltage V_{SD} . As with increasing bias voltage the transport window widens, the so-called Coulomb staircase is observed. With the current first zero, more and more channels become available for transport with increasing V_{SD} . The addition of each channel results in a step in the current.

Coulomb diamonds

The combination of Figure 2.8, (b) and (c), i. e. bias and gate-voltage dependence leads to so-called Coulomb diamonds. This term refers to a diamond shaped conductance pattern as a function of V_{SD} and V_G .

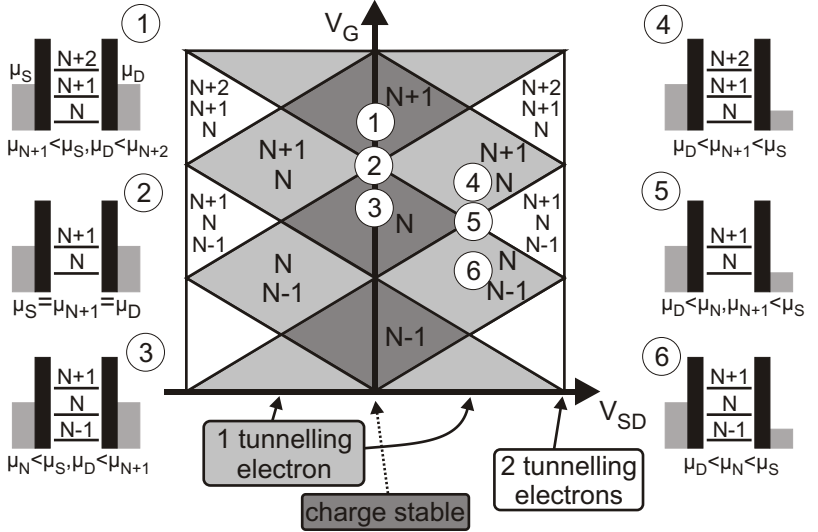


Figure 2.9: Scheme of Coulomb-blockade diamonds with dot energy diagrams and the resulting conductance pattern in dependence of plunger gate V_G and bias voltage (V_{SD}) as explained in the text. Lighter shades indicate higher conductance.

In Figure 2.9 some Coulomb diamonds are schematically depicted.

To understand the emergence of the Coulomb diamonds, we first consider a variation of plunger gate voltage V_G at zero source-drain bias voltage V_{SD} according to the previous discussion (points (1)–(3) as marked in Figure 2.9): Inside a Coulomb diamond of vanishing conductance marked by (3) in the figure the system is Coulomb blocked and the charge Ne on the quantum dot is stable. Increasing the plunger gate voltage V_G will bring the SET to the charge degeneracy point (2) where the number of electrons can fluctuate between N and $N + 1$. A further increase of V_G eventually ends in another stable configuration (3) with $N + 1$ electrons on the dot.

The influence of a finite source-drain bias voltage V_{SD} is illustrated by including the configurations (4) to (6) into our consideration: When

the source-drain bias voltage is increased by lowering the right reservoir's chemical potential, starting at the stable configuration (1) with $N + 1$ electrons, the transport window is widened until in region (4) the chemical potential for $N + 1$ electron on the dot lies between the chemical potentials in the reservoirs. This enables transport with the charge on the dot fluctuating between N and $N + 1$ electrons. As in the $V_{SD} = 0$ case, a decrease of gate voltage in regions (5) and (6) leads to dot charges fluctuating between $N - 1$, N and $N + 1$ in region (5) and $N - 1$ and N in (6). Coulomb diamonds apart from but interlocked with the ones lined up at $V_{SD} = 0$ emerge. These new diamonds differ from the first ones by their finite conductance. At even higher bias voltages further Coulomb diamonds appear with dot charges fluctuating not only by one but by two or more electrons. Thus the conductance in these diamonds is even higher.

To conclude, the conductance of a quantum dot showing Coulomb blockade can be tuned by either varying a gate voltage, leading to Coulomb resonances, or by tuning the bias voltage, leading to a Coulomb staircase. The combination of both make up the Coulomb diamonds. These are purely classical effects based on charge quantization without any quantum mechanics involved.

2.3.4 Excitation spectroscopy

In addition to charge quantization, the electronic level spectrum of a quantum dot and in conclusion quantum mechanics also contributes to the addition spectrum. We have already considered this fact in the constant-interaction model. It becomes prominent in two situations: First we discuss a level spacing $\Delta\varepsilon_i = \varepsilon_{i+1} - \varepsilon_i$ which is not constant but varies as a function of i . When it is comparable to the charging energy U or even larger, the Coulomb oscillations become aperiodic. This is observed in vertical quantum dots [2]. In larger lateral dots with $\Delta\varepsilon_i$ much smaller than U it is a small effect, and we approximate $\Delta\varepsilon_i \approx \Delta\varepsilon$.

Second, the electronic level spectrum also becomes visible if more than one electronic energy level comes into the transport window, e. g. ε_i and ε_{i+1} . Then an electron tunnelling into the dot can tunnel into either state i or state $i + 1$ which gives rise to a change in the

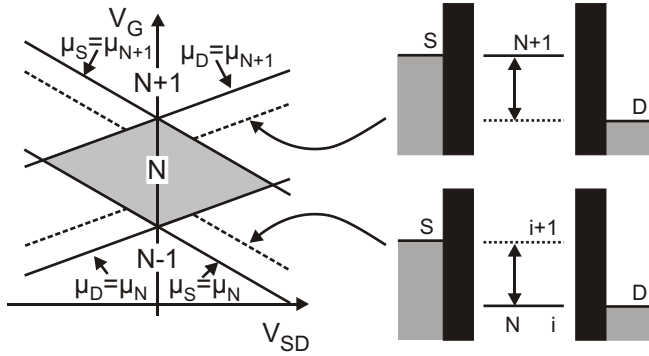


Figure 2.10: Scheme of excitation spectroscopy of a quantum dot in nonlinear transport measurements, the lines indicating increased differential conductance and thus the opening of additional transport channels. The corresponding energy diagrams relate these channels to tunnelling through excited states.

tunnel current. These states are never simultaneously occupied as the bias window is too small to overcome the additional charging energy U . The increase is solely due to the existence of a second channel.

Figure 2.10 illustrates how these additional transport channels modify the Coulomb diamonds in a differential conductance measurement. In such measurements, not the absolute conductance but its derivative dI/dV_{SD} with respect to source-drain voltage V_{SD} is detected. Hence, steps in the absolute conductance become peaks in differential conductance. In the figure, dashed diagonal lines of increased differential conductance parallel to the borders of the Coulomb diamonds mark additional steps in the quantum dot conductance. The energy diagrams relate the additional transport channels to excited states in the quantum dot. These come into the transport window at the increased bias voltage. Not every excited state is necessarily visible in the type of measurement discussed here, since some states may couple to the reservoirs only weakly.

The increases in tunnelling current allow to spectroscopically investigate the excitation spectrum of quantum dots by variation of the bias

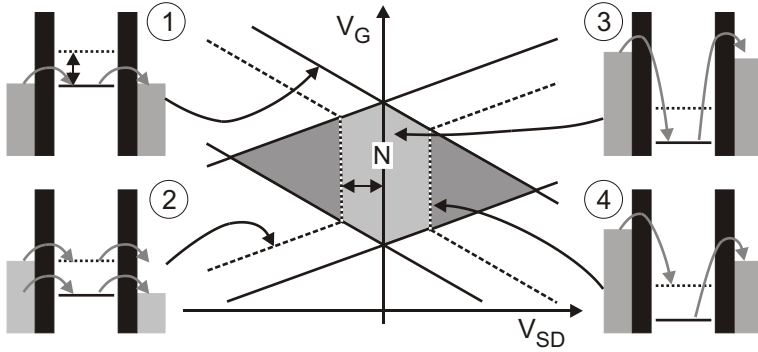


Figure 2.11: Scheme of a Coulomb diamond with excited states and with a differential background conductance due to elastic (light grey area) and inelastic cotunnelling (dark grey area). The quantum dot ground state (solid lines) and an excited state (dotted lines) are considered. (1) and (2) are first order tunnelling processes, (3) and (4) represent cotunnelling processes.

voltage and to experimentally determine the level spacing $\Delta\varepsilon_i$.

2.3.5 Cotunnelling

Until now, only first order tunnelling between quantum dot and leads was considered. The term *cotunnelling* generally refers to higher order tunnelling processes, i. e. two or more correlated tunnelling events involving energetically forbidden intermediate states. As an example for a second order tunnelling process, an electron might tunnel onto a SET despite Coulomb blockade. The resulting virtual intermediate state is energetically forbidden. The lifetime of this virtual state is given by Heisenberg's uncertainty relation, $\tau \lesssim h/\Delta E$. It decays by removal of one electron from the dot, and energy conservation is again satisfied.

Cotunnelling contributes to the background conductance in transport measurements as illustrated in Figure 2.11 [37, 38]. Processes (1) and (2) are the known first order tunnelling processes, (1) giving rise to Coulomb resonances and (2) involving an excited state. (3) depicts an elastic cotunnelling process responsible for a constant background

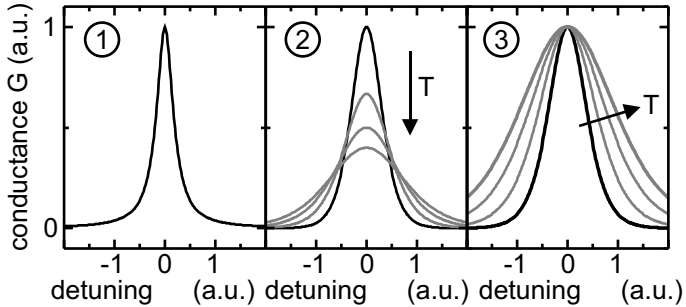


Figure 2.12: Typical types of Coulomb oscillations in a quantum dot for temperatures T in the three regimes discussed in the text and as named in Figure 2.13. The traces are normalized for each regime, the black curves having been calculated for the lowest temperature. The arrows indicate increasing temperatures.

conductance in the Coulomb diamond. At (4) the transport window is large enough for an additional inelastic cotunnelling channel to be opened. This channel involves an excited state on the dot. It is called inelastic because the state of the dot before and after the process differ. After the tunnelling process the dot is in an excited state and relaxes into its ground state. Inelastic cotunnelling is only observed if the level spacing $\Delta\varepsilon$ is smaller than the Coulomb energy U . It sets in at a source-drain voltage of $eV_{SD} \geq \Delta\varepsilon$.

Since cotunnelling is proportional to the bias voltage V_{SD} , it produces a constant differential conductance despite the peaks in differential conductance making up the Coulomb diamonds.

2.4 Coulomb-resonance lineshape

We determine the energy scales of the quantum dot from the line-shapes of Coulomb resonances. Typical Coulomb resonances as seen in the conductance measurements are shown in Figure 2.12 as a function of detuning $\delta\varepsilon = \varepsilon - \varepsilon_0$ from the resonance at ε_0 . The detuning is determined by the plunger gate voltage V_G . The lineshape of the

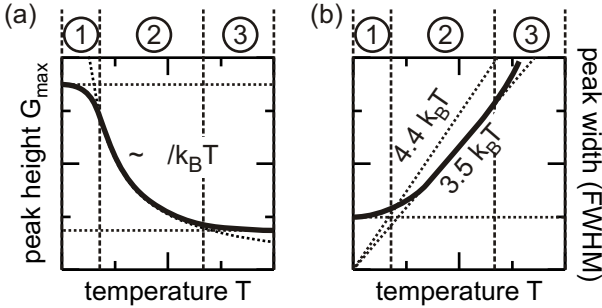


Figure 2.13: Peak (a) height and (b) width of Coulomb resonances in dependence on temperature T in the three regimes discussed in the text: (1) low temperature limit, $k_B T \ll \hbar\Gamma \ll \Delta\varepsilon$, (2) finite temperatures, $\hbar\Gamma \ll k_B T \ll \Delta\varepsilon$, and (3) high temperatures $\hbar\Gamma, \Delta\varepsilon \lesssim k_B T$.

resonances depends on three quantities: intrinsic linewidth $\hbar\Gamma$, temperature $k_B T$ and electronic level spacing $\Delta\varepsilon$. It is modified if the electronic level spacing is so small that multiple levels lie within one Coulomb resonance. The thermal energy $k_B T$ does not modify the resonance itself as in the Coulomb-blockade regime it always is small compared to the charging energy U , $k_B T \ll U$. Thus it has no influence on the dot occupation N . Source and drain reservoirs, however, have a continuous density of states occupied according to the Fermi-Dirac distribution function. This broadens the measured lineshape at finite temperature, whereas at $T = 0$ a step-like Fermi distribution does not lead to any broadening. The intrinsic resonance linewidth $\hbar\Gamma$, finally, is determined by Heisenberg's uncertainty relation containing the finite lifetime $\tau \sim 1/\Gamma$ of the investigated state on the quantum dot. It depends mainly on the tunnel coupling to the leads.

Following Reference [39] we distinguish three regimes in the dependence of the Coulomb lineshape on the above-mentioned parameters. Typical lineshapes are depicted in Figure 2.12. Figure 2.13 shows peak width and height as a function of temperature for all three regimes.

(1) Low temperature limes, $k_B T \ll \hbar\Gamma \ll \Delta\varepsilon$

The low temperature limes is characterized by thermal energies $k_B T$ negligible compared to the intrinsic linewidth $\hbar\Gamma$. Coulomb resonances in this regime are described by the well-known Breit-Wigner formula [40] with a full width at half maximum (*FWHM*) of $\hbar\Gamma$ [39]:

$$G(\delta\varepsilon)/G_{max} = \hbar \frac{\Gamma_l \Gamma_r}{\Gamma_l + \Gamma_r} \cdot \frac{\hbar\Gamma}{(\delta\varepsilon)^2 + (\hbar\Gamma/2)^2} \text{ for } k_B T \ll \hbar\Gamma \ll \Delta\varepsilon \quad (2.21)$$

Γ_l and Γ_r denote the tunnel coupling of the dot to the left and right reservoirs, and $\Gamma = \Gamma_l + \Gamma_r$. If \mathcal{G} is the degeneracy of the resonant level, the peak conductance G_{max} in this regime is given by

$$G_{max} = \mathcal{G} \frac{e^2}{h}. \quad (2.22)$$

Neither Coulomb-peak height nor width depend on temperature in this regime. This is reflected in the temperature independent asymptotes in Figure 2.13 at low temperatures (regime (1)).

(2) Finite temperatures, $\hbar\Gamma \ll k_B T \ll \Delta\varepsilon$

This regime is reached when the thermal energy $k_B T$ is large compared to the intrinsic linewidth $\hbar\Gamma$ but small compared to the level spacing $\Delta\varepsilon$. Thermal broadening for the Fermi-Dirac distributed electrons in the reservoirs determines the lineshape. $G(\delta\varepsilon)/G_{max}$ is basically given by the derivative of the Fermi distribution function with respect to energy [39],

$$G(\delta\varepsilon)/G_{max} = \left(\cosh \frac{\delta\varepsilon}{2k_B T} \right)^{-2} \text{ for } \hbar\Gamma \ll k_B T \ll \Delta\varepsilon. \quad (2.23)$$

The peak conductance G_{max} is proportional to the intrinsic linewidth $\hbar\Gamma$ and to the inverse temperature T^{-1} :

$$G_{max} = \frac{e^2}{4k_B T} \cdot \frac{\Gamma_l \Gamma_r}{\Gamma_l + \Gamma_r} = \frac{e^2}{16} \cdot \frac{\Gamma}{k_B T} \quad (2.24)$$

The FWHM is given by

$$\text{FWHM} = 4 \cdot \text{arccosh}(\sqrt{2}) \cdot k_B T \approx 3.53 \cdot k_B T. \quad (2.25)$$

In this experimentally particularly important regime the linewidth is proportional to the temperature T . The conductance maximum, however, is proportional to the inverse temperature T^{-1} . Thus the area $A \sim G_{max} \cdot \text{FWHM}$ under the peak is independent of the temperature T . This is regime (2) in Figures 2.12 and 2.13.

The known temperature dependence of the FWHM of Coulomb peaks in this regime allows to determine the lever arm α_i (section 2.3.1).

(3) High temperatures, $\hbar\Gamma, \Delta\varepsilon \lesssim k_B T$

When the temperature is increased even further, the thermal energy $k_B T$ becomes the largest energy scale. Many single-particle levels in the dot contribute to transport if $\Delta\varepsilon \lesssim k_B T$, leading to multilevel transport [39, 41]:

$$\begin{aligned} G(\delta\varepsilon)/G_{max} &= \frac{\delta\varepsilon/k_B T}{\sinh(\delta\varepsilon/k_B T)} \\ &\approx \left(\cosh \frac{\delta\varepsilon}{2.5k_B T} \right)^{-2} \quad \text{for } \hbar\Gamma, \Delta\varepsilon \ll k_B T. \end{aligned} \quad (2.26)$$

The peak conductance G_{max} depends on the density of states ρ within the quantum dot (it makes no longer sense to talk about single levels) and on the intrinsic linewidth $\hbar\Gamma$, but is independent on temperature T :

$$G_{max} = \frac{e^2 \rho}{2} \cdot \frac{\Gamma_l \Gamma_r}{\Gamma_l + \Gamma_r} = \frac{e^2 \rho}{8} \cdot \Gamma \quad (2.27)$$

The FWHM is proportional to the temperature T , approximately:

$$W \approx 4.35 \cdot k_B T. \quad (2.28)$$

This situation is reflected as regime (3) in Figures 2.12 and 2.13.

The three regimes described above are distinguished by their individual characteristic dependence of peak height and width on temperature. In this work, the quantum dots are typically operated in the finite temperature regime.

3 Experiment

In this chapter the fabrication of the split-gate single-electron tunnelling transistors and the low-temperature measurement techniques employed for the investigation of their transport properties are described.

3.1 Heterostructures

The starting point for the structures investigated in this thesis are modulation doped GaAs/AlGaAs heterostructures [7]. In such structures extremely high electron mobilities are achieved by spatial separation of conduction electrons from scatterers like their parent donor atoms. Epitaxial growth by molecular beam epitaxy (MBE) allows to fabricate crystals of excellent quality with only few contaminating impurities, both further improving the mobility.

In general, heterostructures consist of layers of two or more semiconductors with different band gaps. Similar lattice constants of the constituents allow to grow single crystals without dislocations. With the correct layer sequence it is possible to form nearly arbitrary potential profiles in the growth direction. A preferred material system for this so-called band gap engineering is $\text{Ga}_{1-x}\text{Al}_x\text{As}$ because its band gap is continuously varied with the aluminium concentration x from $E_{\text{GaAs}} = 1.5$ eV to $E_{\text{Ga}_{0.67}\text{Al}_{0.33}\text{As}} \approx 1.91$ eV [42]. GaAs and AlAs have almost the same lattice constants, $a_{\text{GaAs}} = 5.6533$ Å and $a_{\text{AlAs}} = 5.6611$ [43]. This allows defect free, crystalline growth of arbitrary material mixtures. Nowadays electron mobilities exceeding 3000 m²/Vs are reached by this method.

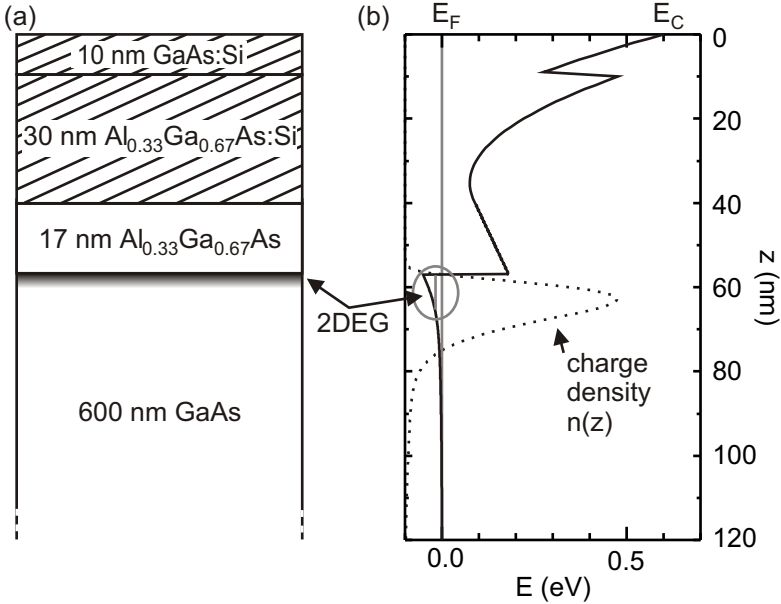


Figure 3.1: (a) Layer sequence of heterostructure 1129 which was used in the experiments. (b) Simulation of the resulting conduction band edge and formation of the two-dimensional electron gas in the triangular potential minimum.

In this work, mainly heterostructure 1129 grown at the Ruhr-Universität Bochum in the group of D. Reuter and A. D. Wieck was used. In Figure 3.1 the according layer sequence is shown together with a simulated band structure. As can be seen in the simulation, at the AlGaAs/GaAs interface a triangular potential well in the conduction band energy E_C is formed. Quantized states in this potential well lead to the formation of two-dimensional subbands in the xy -plane. At sufficiently low temperatures, only the lowest subband is occupied. Then the heterostructure contains only one two-dimensional electron system (2DES) 57 nm below the surface.

The sample was characterized in standard quantum Hall measurements [44], yielding an electron density of $n = 3.7 \cdot 10^{15} \text{ m}^{-2}$ and a

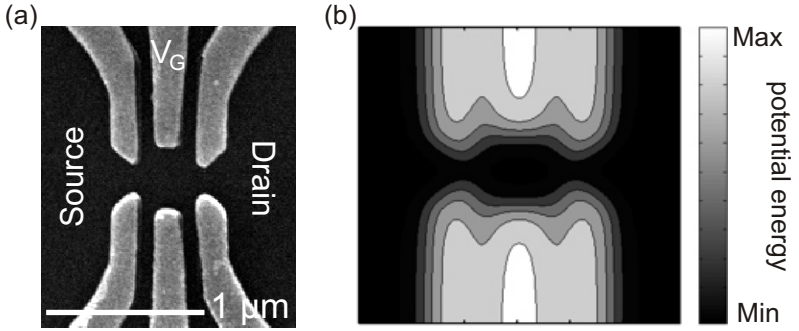


Figure 3.2: (a) SEM micrograph of the central gate structure forming the quantum dot. (b) Simulated potential energy in the 2DES created by application of -1 V to each gate electrode (self-consistent calculation by courtesy of M. Stopa).

low temperature mobility of $\mu = 130$ m²/Vs. Further information on the heterostructure and the simulation of band structures is given in appendix C.

3.2 Patterning of the 2DES

Even more than 10 years after the advent of the first lateral semiconductor SETs, the patterning of quantum dots only a few 100 nm wide in a 2DES 57 nm below the substrate surface remains a challenge. Three orders of magnitude have to be overcome to contact the less than 100 nm wide gate electrodes to 100 μ m wide bond pads. This is achieved by the combination of optical and electron beam lithography described in this section.

Standard Hall bars are patterned on the heterostructure by optical lithography [45]: First, the 2DES is contacted by alloyed Au/Ge/Ni pads and in a second step a mesa is etched from the heterostructure. Afterwards, six metallic gate electrodes (6 nm Cr, 25 nm Au) are fabricated on each Hall bar using two further electron beam lithography steps [46, 47]. A scanning electron microscopic (SEM) image of the central region of the gate structure which later forms the quantum

dot is shown in Figure 3.2(a). The 2DES areas serving as source and drain leads are marked. Visible are the six finger gates used to define a quantum dot in the centre. The central upper gate electrode is used as a plunger gate for shifting the quantum dot energy levels. As shown in Figure 3.2(b), negative voltages applied to all gate electrodes allow to deplete the two-dimensional electron gas underneath. In this way, a potential minimum is created in the 2DES. This small island contains electrons which are separated from the bulk 2DES by tunnel barriers, visible as constrictions in the Figure. The fabrication scheme is explicated in more detail in appendix B.

From the SEM image a geometric dot diameter of 380 nm is deduced. Taking into account the depletion length of the split gates, we obtain an electronic diameter of $d_{el} \approx 250$ nm. Such a dot of area A is estimated to contain $N \sim n \cdot A = 180$ electrons.

3.3 Measurement setup

The study of single-electron transport in split gate transistors requires low temperatures and a highly accurate low-noise setup. Thermal energy and noise level are to be kept small compared to the level spacing between the quantum dot states. In this work, four different cryogenic systems were used:

- ^4He storage vessel for easy and rapid characterization measurements at $T = 4.2$ K, mainly to test ohmic contacts.
- ^4He bath cryostat from Oxford Instruments for quantum Hall characterization measurements at $T \geq 1.3$ K.
- Single-shot ^3He insert from Oxford Instruments in a ^4He bath cryostat for temperatures between $T = 350$ mK and 4.2 K. The measurement setup was developed in this cryostat. Some first productive SET measurements were also conducted here.
- Oxford Instruments Kelvinox 300 ^3He - ^4He dilution refrigerator for nearly all SET measurements shown in this thesis. This cryostat reaches a base temperature of approximately 20 mK (with

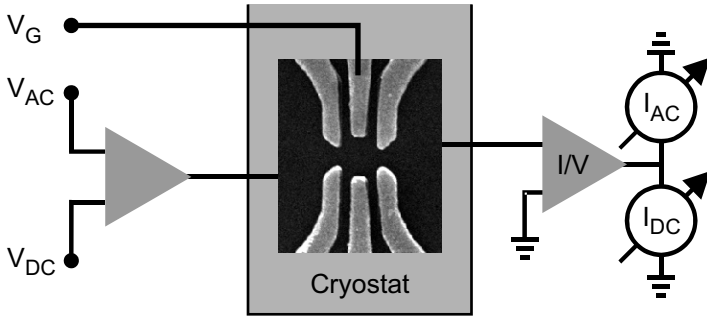


Figure 3.3: Schematic setup for the electronic transport measurements.

the samples mounted). A superconducting magnet reaching fields of up to $B = 13$ T is integrated into the cryostat.

A detailed introduction to cryogenics is given in Reference [48].

We have sketched a simplified setup for the electrical transport measurements in Figure 3.3. The oscillator output voltage V_{AC} of an EG&G 7260 lock-in amplifier is added to a DC voltage V_{DC} generated by an IOtech DAC488 HR/4 digital to analog converter (DAC). This signal is divided by a factor of 1000, filtered and then applied to the source contact of the sample. It is adjusted so that the AC voltage modulation across the sample is $V_{SD,AC} = 10 \mu\text{V}$ at a frequency of 86.666 Hz. The drain contact of the sample is connected to an Ithaco 1211 current amplifier providing a virtual ground to the sample. The current amplifier's output is split into an AC component connected to the input of the lock-in amplifier and a low-pass filtered DC component which is read out with a Keithley 2000 multimeter. The split gate electrodes are connected to the remaining three output channels of the DAC. These leads also contain voltage dividers (1 by 6.5). Because of the limited number of DAC channels, opposite gate electrodes are connected to the same output, except for the plunger gate which is controlled individually to keep the lever arm for shifting dot energy levels low.

To achieve a good signal quality and sufficiently low temperatures, extreme care has to be taken with filtering of the electrical signals. This is true in particular for the dilution refrigerator. All signal lines enter the cryostat only through π filters at room temperature. These have a cut-off frequency of ~ 10 MHz. The voltage dividers are mounted close to these filters. In the cryostat at base temperature additional low pass filtering is applied to the extremely noise sensitive lines connecting the gate electrodes. These RC filters have a cut-off frequency of ~ 1 Hz. All measurement equipment is connected through individual insulating transformers to the wall sockets. GPIB/IEEE 488 and serial connections to the computer controlling the experiment contain optocouplers to insulate high-frequency noise from digital transients and to avoid ground loops. With these measures, in the dilution refrigerator an electronic temperature of $T_{el} \lesssim 70$ mK is achieved as known from Coulomb blockade measurements (chapter 4.2).

4 Coulomb-blockade regime

In this chapter, we explore transport through our split-gate quantum dots in the Coulomb-blockade transport regime. This regime is characterized by a weak tunnel coupling between dot and leads. The prevailing phenomena in this regime reviewed in chapter 2 are well understood. This allows to characterize the interacting multi-electron system in the quantum dot and its interaction with the gate electrodes.

We pay particular attention to magneto-transport spectroscopy. A magnetic field provides an additional means of tuning the relative strengths of confinement, Coulomb, exchange and Zeeman energy of the electrons on the dot and thus to influence their many-electron ground state.

With one exception (Figure 4.6(b)) all data presented in this chapter is from the same sample 1129-8-7.3 and from the same cooling cycle. In this way, we consistently characterize this device.

4.1 Linear conductance measurements

Linear conductance measurements on a quantum dot are always conducted at zero bias voltage $V_{SD} = 0$, i. e. in the linear response regime. Hence the transport window (chapter 2.3.3) ideally is infinitely narrow. In Figure 4.1, such a measurement is shown as a function of plunger gate voltage V_G . We observe regularly spaced Coulomb peaks, $\Delta V_G \sim \text{const}$. As explicated in chapter 2.3.3, these peaks appear whenever the chemical potential for adding another electron to the dot is in resonance with the source and drain reservoirs. Each peak is interpreted as the addition of one electron to the dot. The peak height fluctuates indicating that the dot is in the quantum regime with only one internal

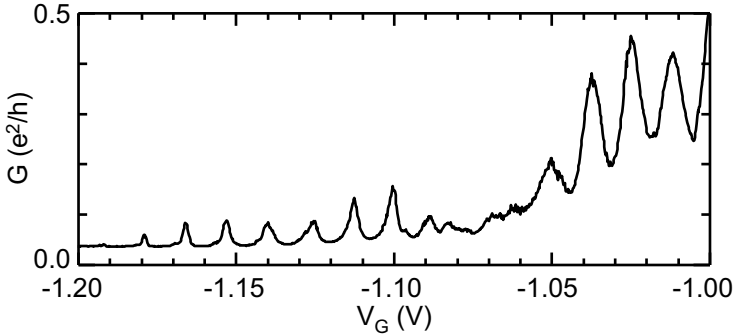


Figure 4.1: Coulomb-blockade oscillations in a linear conductance measurement. Each of the regular Coulomb peaks at increasing plunger gate voltage V_G marks the addition of one extra electron to the quantum dot. At $V_G \sim -1.07$ V this regularity is broken due to a charge reconfiguration on the dot.

level coupling to the reservoirs: Different internal states couple to the reservoirs with different strengths leading to the observed amplitude modulation. Apart from the modulation, the peak height increases with rising plunger gate voltage. This is due to the spatial proximity of the plunger gate to the tunnel barriers which are still in the range of the plunger gate's electrostatic potential. At $V_G \sim -1.2$ V this coupling is so low that the Coulomb resonances vanish. At $V_G \sim -1$ V it is high enough for different Coulomb oscillations to overlap resulting in a non-zero conductance in between. A reconfiguration of the charges on the dot is responsible for the deviations from regular Coulomb blockade at $V_G \sim -1.07$ V: At an increased internal dot energy a new ground state becomes favorable, leading to a redistribution of the electrons on the dot.

According to the constant-interaction model from chapter 2.3.2, the total energy $E_{N,I}$ of a quantum dot containing N electrons in state I is a sum of Coulomb energy E_N and quantum mechanical energy E_N^I . Adding one electron costs Coulomb charging energy $U = e^2/C_\Sigma$ plus single-particle energy ε_i . Assuming that the single particle energy is generally different for each single particle state $i \in I$, we conclude

$\varepsilon_i \ll U$ because the spacing of the Coulomb peaks is nearly constant. Thus the spacing $\Delta V_G \approx 13$ mV reflects the charging energy of the dot. Knowledge of the lever arm α_G (equation 2.18) would allow to convert the unit from gate voltage to energy. Anticipating $\alpha_G = 0.045$ from the discussion of the temperature dependence of Coulomb oscillations in the next section, a charging energy of

$$U \approx 0.590 \text{ meV}$$

and a total capacitance

$$C_\Sigma \approx 270 \text{ aF}$$

are computed. The gate capacitance is

$$C_G = e/\Delta V_G \approx 12 \text{ aF}.$$

These results are summarized in table 4.1 on page 62. Further information on the quantum dot is determined in the next section.

4.2 Temperature dependence of Coulomb oscillations

In this section we will extract the lever arm α_G and the intrinsic linewidth $\hbar\Gamma$ of the SET from the temperature dependence of linear conductance measurements. A model for the variation of Coulomb-peak lineshapes as a function of temperature was discussed in chapter 2.4.

Figure 4.2(a) shows a Coulomb resonance in linear conductance for various temperatures. Since the peak height drops with increasing temperature but the width increases, the finite temperature limit is applicable. From equation 2.25,

$$\text{FWHM} \approx 3.53 \cdot k_B T,$$

at finite temperatures it is possible to identify an energy scale in terms of plunger gate voltage V_G (i. e. the peak's FWHM ΔV_G) with an absolute energy scale $k_B T$. Therefore the slope of the $\Delta V_G(T)$ curve has to be determined. However, particularly for low temperatures the

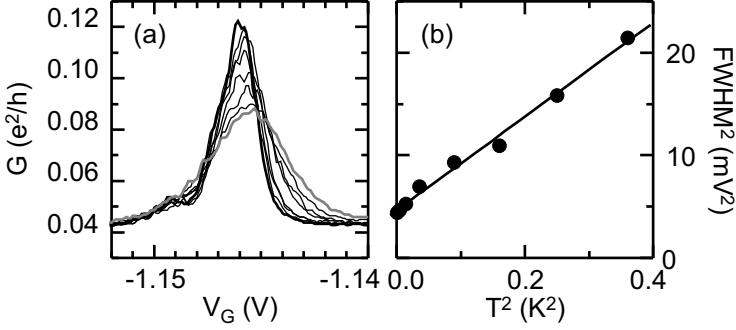


Figure 4.2: (a) Coulomb oscillations in linear conductance at temperatures $T = 30$ mK, 70 mK, 120 mK, 190 mK, 300 mK, 400 mK, 500 mK and 600 mK. (b) Quadratic peak widths (FWHM) from Figure (a) versus quadratic temperature.

total width W_{total} of a Coulomb peak is given by a convolution of peaks with a width W_1 according to the above formula with peaks with the intrinsic linewidth $W_2 = \hbar\Gamma$. Modelling Gaussian lineshapes the convolution yields a peak with FWHM $W_{total}^2 = W_1^2 + W_2^2$. Thus the quantity to be considered is $\Delta V_G^2(T^2)$ as shown in Figure 4.2(b). From the slope a of this curve a lever arm of

$$\alpha_G = \frac{3.5k_B}{e} \cdot \frac{1}{\sqrt{a}} = 0.045$$

is determined. An extrapolation of this curve to $T = 0$ yields an axis intercept y_0 from which the intrinsic resonance linewidth is computed:

$$\hbar\Gamma = e\alpha_G \cdot \sqrt{y_0} = 100 \mu\text{eV}.$$

Deviations from the temperature dependence of Coulomb-peak lineshapes expected from the discussion in chapter 2.4 are frequently observed at low temperatures. They are attributed to a deviation of the electronic temperature from the measured temperature of the cryostat's mixing chamber. Such a decoupling of electronic and lattice temperatures in our experiment is observed at $T \lesssim 70$ mK (not shown). The electronic temperature is assumed to saturate in this range.

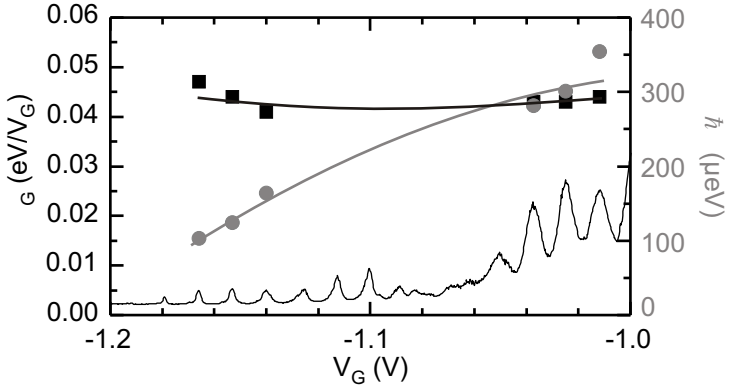


Figure 4.3: Lever arm α_G (black squares) and intrinsic linewidth $\hbar\Gamma$ (grey circles) determined from the temperature dependence of several Coulomb oscillations. These quantities are shown together with lines to guide the eye and Coulomb oscillations at base temperature.

We have analyzed temperature dependencies for several Coulomb peaks. The results are summarized in Figure 4.3. With increasing plunger gate voltage the intrinsic linewidth $\hbar\Gamma$ of the resonances increases while the lever arm α_G is almost constant. The increase of $\hbar\Gamma$ is attributed to the influence of the plunger gate on the height of the tunnel barriers due to spatial proximity. Decreased tunnel barriers shorten the lifetime and thus increase the width of the resonant level. For even higher plunger gate voltages $V_G \gtrsim -1$ V, due to the increased coupling to the leads other mechanisms start to dominate transport and the dot is no longer in the regime of weak coupling. Therefore this simple analysis of the Coulomb lineshape as a function of temperature is not possible anymore.

4.3 Nonlinear conductance measurements

In addition to the variation of the plunger gate voltage V_G in linear conductance measurements, in nonlinear differential conductance measurements of dI/dV_{SD} the bias voltage V_{SD} between source and drain

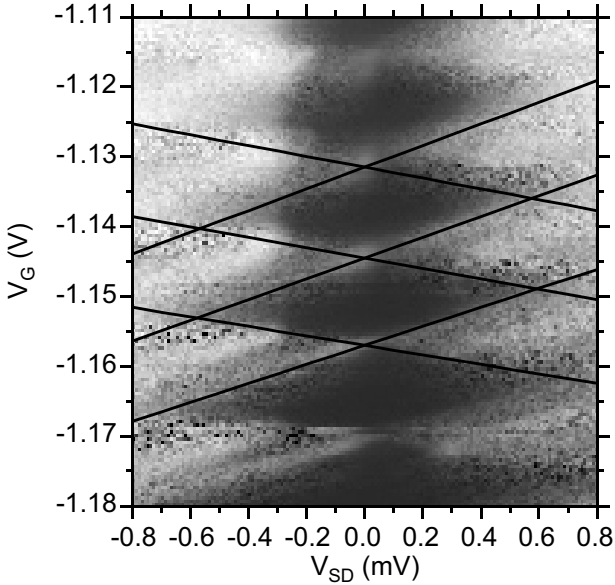


Figure 4.4: Differential conductance as a function of bias V_{SD} and plunger gate voltage V_G in grey scale, black corresponding to $dI/dV_{SD} = 0$ and white to $dI/dV_{SD} = 0.35 e^2/h$. Black lines highlight the Coulomb-blockade diamonds.

reservoirs is also swept. Such a measurement is shown as a grey scale plot of the differential conductance in Figure 4.4. Coulomb diamonds of vanishing conductance are lined up along the gate voltage axis at $V_{SD} = 0$ (chapter 2.3.3). At $V_G \sim -1.17$ V, a slight charge reconfiguration on the dot is observed. Coulomb-blockade diamonds allow to determine the dot-gate capacitances from the electrostatic capacitance model.

4.3.1 Charging energy and total capacitance

The width of the Coulomb diamonds allows to estimate the charging energy U by assuming lever arms of source and drain contacts of

$\alpha_{S,D} \approx 0.5$ according to equation 2.18 and assuming that source and drain capacitances are the main contributions to the total capacitance. Neglecting quantum mechanical single particle energies, for the measurement presented in Figure 4.4 this results in

$$U = \alpha_S e \Delta V_{SD} \approx 0.6 \text{ meV.}$$

The total capacitance is determined from equation 2.17:

$$C_\Sigma = \frac{e^2}{U} \approx 270 \text{ aF.}$$

These results are in good agreement to the values obtained from linear and temperature dependent conductance measurements in the previous sections.

4.3.2 Determination of dot-gate and dot-contact capacitances

The capacitances of the quantum dot to its surroundings are determined from the slopes of the Coulomb diamonds. We combine the stability considerations (Figure 2.9 on page 23) with equation 2.16 from the electrostatic capacitance model. We recall the bias voltage and plunger gate-voltage dependent contributions ($V_S = 0$ and $V_D = V_{SD}$):

$$\mu_N(V_{SD}, V_G) = e \frac{C_D}{C_\Sigma} V_{SD} + e \frac{C_G}{C_\Sigma} V_G + \text{const.}$$

At the border of a Coulomb diamond, the chemical potential μ_N for adding the N th electron to the dot is in resonance with either the source or drain reservoir's chemical potential (Figure 4.5). Setting $\mu_S = 0$ and $\mu_D = eV_{SD}$, from $\mu_S \stackrel{!}{=} \mu_N$ we get

$$\left(\frac{\Delta V_G}{\Delta V_{SD}} \right)^{(S)} = m_S = -\frac{C_D}{C_G} \quad (4.1)$$

for resonance with the source chemical potential and from $\mu_D \stackrel{!}{=} \mu_N$ we get

$$\left(\frac{\Delta V_G}{\Delta V_{SD}} \right)^{(D)} = m_D = \frac{C_\Sigma - C_D}{C_G}. \quad (4.2)$$

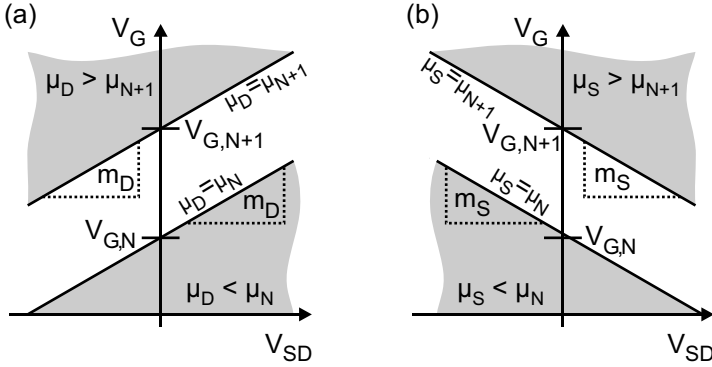


Figure 4.5: The slopes (a) m_D and (b) m_S of the Coulomb diamonds allow to determine the dot capacitances. $V_{G,N}$ and $V_{G,N+1}$ determine the gate voltages of two successive Coulomb resonances at $V_{SD} = 0$.

for resonance with the drain chemical potential.

We determine $m_S = -7.4$ and $m_D = 14.8$ from Figure 4.4 at $V_G \sim -1.146$ V, thus

$$\alpha_D = \frac{1}{1 - m_D/m_S} \approx 0.3 \quad \text{and} \quad \alpha_G = \frac{1}{m_D - m_S} \approx 0.045.$$

Assuming $C_\Sigma = 270$ aF from previous results, the capacitances are

$$C_D \approx 90 \text{ aF} \quad \text{and} \quad C_G \approx 12 \text{ aF}.$$

The source capacitance C_S is expected to have a similar value as the drain capacitance C_D and can only be determined from a separate measurement with the source and drain leads swapped. Source and drain capacitances give the largest contributions to the total dot capacitance.

4.3.3 Excitation spectrum

In nonlinear conductance measurements not only the charging energy of a SET and its capacitances are probed but also the electronic level spectrum of the dot (chapter 2.3.4). In these measurements, diagonal lines of increased differential conductance are not only observed at the

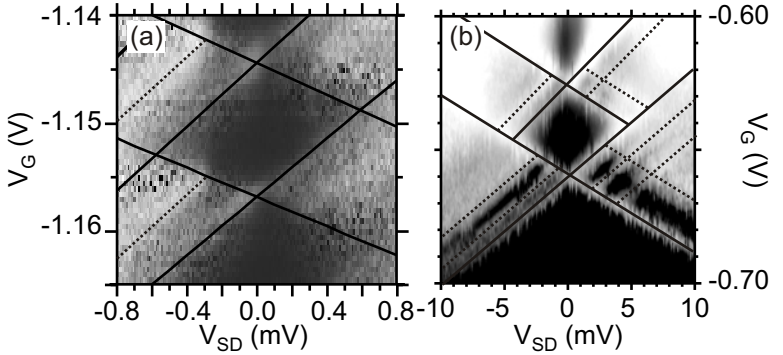


Figure 4.6: Excitation spectra (dotted lines) in Coulomb diamonds (solid lines) for two different quantum dots in differential conductance measurements: (a) More detailed view into the measurement already presented in Figure 4.4. (b) Completely different system with extremely small spatial dimensions and consequently with large excitation energies. Please note the different axis scales.

borders of Coulomb diamonds but also parallel to them. Two measurements are shown in Figure 4.6. The additional increases of differential conductance correspond to the opening of extra transport channels through excited dot states. Thus they always lie outside the blockade region.

We extract excitation energies of roughly $\Delta\varepsilon \sim 300 \mu\text{eV}$ from Figure 4.6(a). From equation 2.3 we estimate an electronic level spacing of $\sim 150 \mu\text{eV}$ assuming an electronic quantum dot diameter of 250 nm. Hence in the measurement the second excited state is probed. We do not clearly observe the first excited state. This is attributed to a weak tunnel coupling of the associated wave function to the leads. Additional data from the same measurement (not shown) indicates excitation energies $\Delta\varepsilon \sim 100 \mu\text{eV}$, confirming an electronic level spacing between $\sim 100 \mu\text{eV}$ and $\sim 150 \mu\text{eV}$.

Figure 4.6(b) is from the lithographically identical sample 1129-1-2.2. In this sample, only one pair of opposite split gates was used to form a dot, the others were grounded. We assume that this dot is

formed by an impurity underneath the tunnel barrier [49]. It shows much larger excitation energies, hence the spectrum is more clear than for the sample discussed above. Both, capacitances and excitation energies in this sample indicate an electronic diameter on the order of ~ 10 nm (data found in table 4.1). The data from this dot is shown because due to the smallness of the system and the high excitation energies the excitation spectrum is much more clearly visible.

4.4 Magneto-transport spectroscopy

As explicated in chapter 2.2 the electronic energy levels in a quantum dot are modified by a magnetic field B . These energy levels contribute to the total addition energy for an extra electron on the dot. The addition energy finally is experimentally accessible in the plunger gate voltage of the Coulomb peaks. Thus to spectroscopically investigate the magnetic field dependence of a quantum dot's energy levels, the B -dependence of Coulomb-peak positions is studied. The peak amplitude reveals additional information on the coupling of the current electronic energy level to the 2DES leads.

A magnetic field influences not only the quantum dot's energy levels but also the structure of the leads. As two-dimensional electron systems these are subject to the quantum Hall effect (QHE). Consequently the emitter and collector Fermi levels can no longer be considered constant but oscillate as a function of B . This was experimentally verified e. g. in References [50, 51]. These oscillations have to be considered in magneto-conductance spectroscopy as they obscure the spectrum of the quantum dot itself [52].

Figure 4.7 shows an overview of the magneto-conductance of a quantum dot. The linear conductance is plotted in grey scale as a function of plunger gate voltage V_G and magnetic field B . The nearly horizontal white traces of high conductance represent Coulomb resonances, some of them are highlighted by dotted lines. Their positions shift up and downwards in V_G as functions of B . Some of the shifts appear at the same magnetic field values for all Coulomb resonances and are thus independent of the number of electrons on the dot (vertical dotted lines in the figure). Periodic in $1/B$, they are attributed to the

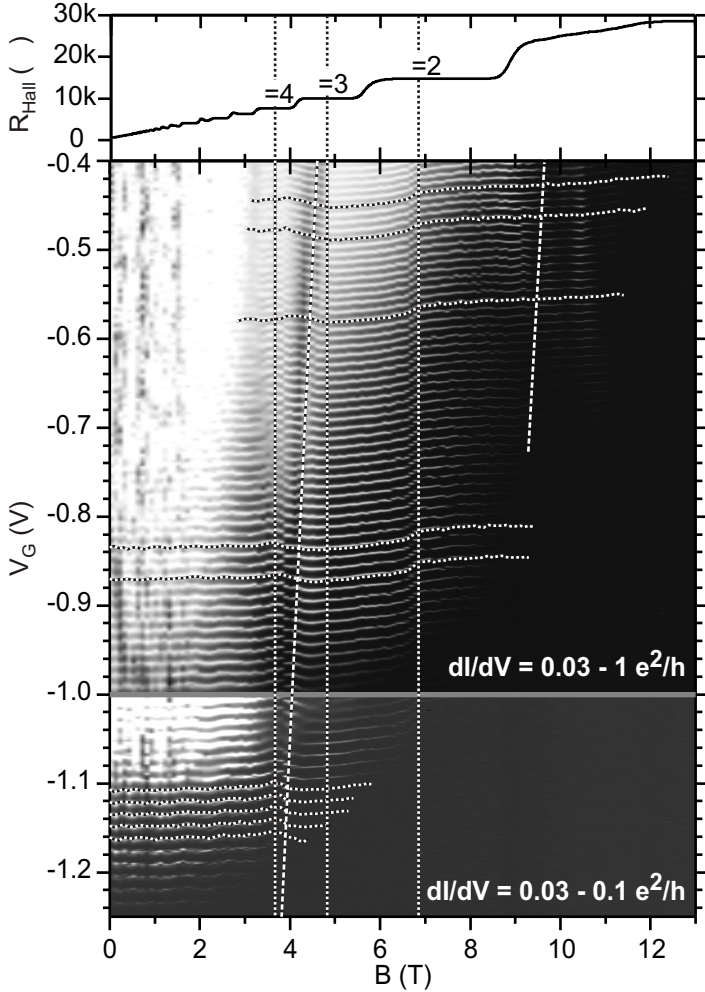


Figure 4.7: Dot conductance on a logarithmic scale as a function of plunger gate voltage V_G and magnetic field B in grey scale (black: low conductance; white: high conductance as indicated). We change the grey scale at $V_G = -1$ V (grey line). At the top of the Figure a two-terminal Hall measurement from the same cooling cycle with all gates grounded is shown.

quantum Hall effect in the 2DES leads and will be addressed in section 4.4.1. They obviously do not depend on the configuration of the dot – then we would expect a variation with gate voltage. Other shifts occur at different magnetic fields for different gate voltages (almost vertical dashed lines at $B \sim 4$ T and 9 T). These are attributed to electron redistributions on the quantum dot itself. The large shifts visible in this large-scale overview are attributed to changes in the dot filling factor as discussed in section 4.4.3. An additional fine structure will be examined in section 4.4.2.

4.4.1 Magneto-oscillations of the emitter Fermi level

The Coulomb-peak position shifts in Figure 4.7 which do not depend on magnetic field are attributed to a quantum Hall effect in the 2DES leads. For comparison, we show a two-terminal quantum Hall measurement of the 2DES in the upper part of the Figure. It is taken from the same sample and cooling cycle as the grey scale plot. Due to the two-terminal nature of the measurement, the Hall resistance R_{Hall} also contains components of the longitudinal resistance with its Shubnikov-de Haas oscillations. The plateaus are not lying at the exact quantized values because the lead and contact series resistances have not been subtracted. It is evident that the marked upwards-shifts in the Coulomb-peak positions are correlated with integer 2DES filling factors at $\nu = 4$ and $\nu = 2$. For higher filling factors the situation is not as clear, and for $\nu = 3$ no peak position shift is observed.

Figure 4.8 shows the shift in the Coulomb-peak position for filling factor $\nu = 2$ for several subsequent peaks from two gate voltage regimes. At $B = 6.8$ T all Coulomb peaks clearly shift upwards by $\Delta V_G \approx 9$ mV.

For an explanation of the above behavior the chemical potential μ of emitter and collector has to be considered. It is calculated according to equation 2.9 for a free electron in a magnetic field and sketched in Figure 4.9(a). μ slowly rises with increasing magnetic field until an integer filling factor is reached. Then, after a sharp drop, the depopulation of another filling factor starts. The energy difference ΔE of these jumps rises with decreasing filling factor. The jumps are generally large at even filling factors due to the beginning depopulation of a new top-

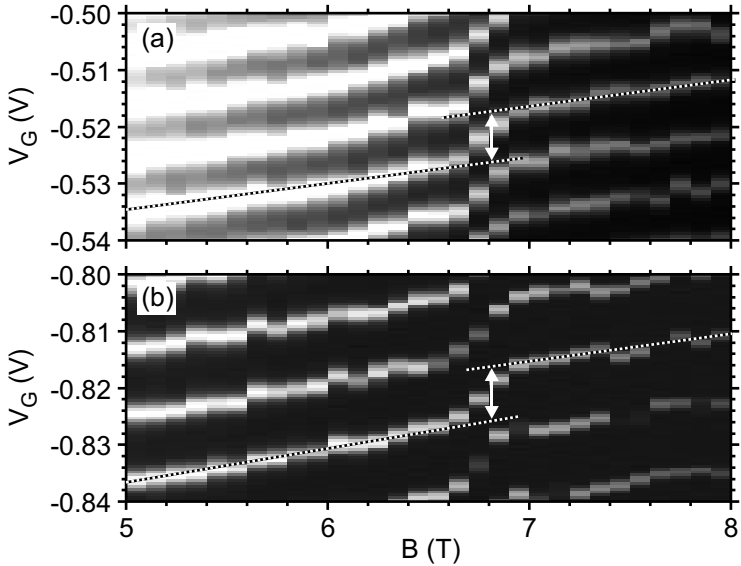


Figure 4.8: More detailed graph of the dot conductance versus V_G and B than in Figure 4.7 (black: low conductance; white: high conductance), reflecting the jumps in the 2DES chemical potential at filling factor $\nu = 2$. Note that the scales on the B -axes are the same.

most Landau level, whereas at odd filling factors only the small Zeeman energy plays a role. In the calculation of μ the exchange enhancement of the g -factor for certain filling factors has been neglected. Therefore the height of some jumps, particularly at $\nu = 1$, is underestimated.

In magneto-conductance spectroscopy, resonance between the dot's chemical potential μ_N and the reservoirs' chemical potentials $\mu_S = \mu_D$ is detected. At jumps in the emitter chemical potential, μ_N has to be adjusted to maintain resonance. This is achieved by a variation of the plunger gate voltage V_G . Thus in a grey scale plot of magneto-conductance versus B and V_G , jumps in the emitter chemical potential are reflected in the V_G -positions of the Coulomb resonances. The downward jumps in $\mu_S = \mu_D$ at integer filling factors require a decreased chemical dot potential μ_N for a continued resonance. This corresponds

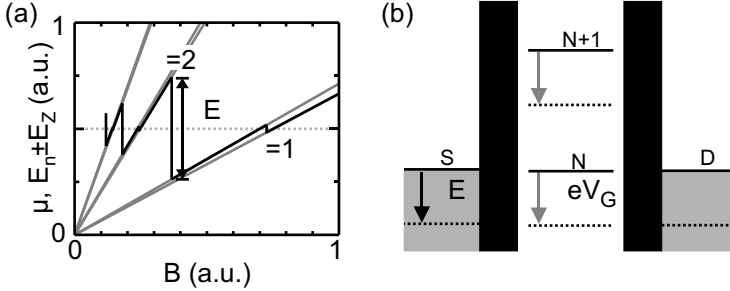


Figure 4.9: (a) The calculated 2DES chemical potential μ taking into account Landau energy E_n and Zeeman energy E_Z , exhibits large, sharp drops by ΔE at even filling factor ν . (b) A drop in the 2DES chemical potential (black arrow) by ΔE requires a less negative plunger gate voltage (grey arrow) to maintain the resonance condition.

to a more positive plunger gate voltage. Figure 4.9(b) illustrates this mechanism connecting the emitter Fermi level variations of a 2DES to the measured magneto-conductance. It explains the observed electron number independent jumps in the Coulomb-peak positions.

One might consider random charge reconfigurations in the vicinity of the dot as an alternative explanation for the discussed discontinuities in the magneto conductance from Figure 4.7. However, the shifts are steep but continuous in B as seen from Figure 4.8. In addition they could be reproduced in a second measurement. Thus they cannot be attributed to such charge reconfigurations.

To summarize, jumps in the Fermi energy at even integer 2DES filling factors explain the gate voltage independent features in Figure 4.7. With increasing filling factor these jumps become smaller which explains that only at $\nu = 2$ and $\nu = 4$ a clear influence of the emitter is observed.

4.4.2 Spectroscopy of the quantum dot

We deduce information on the quantum dot itself from magneto-conductance measurements by following the gate voltage position of sin-

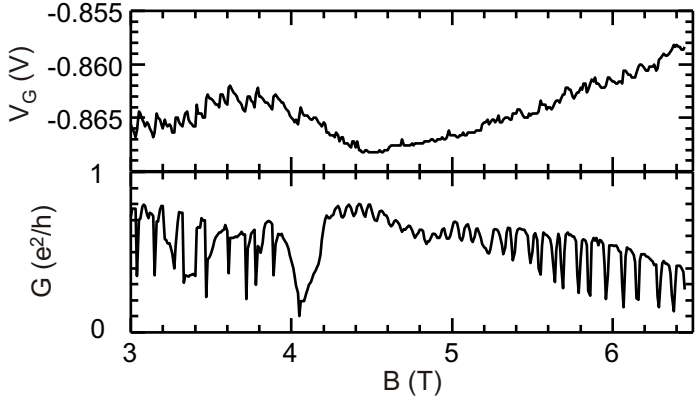


Figure 4.10: Position (in gate voltage V_G) and amplitude G of a Coulomb peak over a wide range of magnetic field B . Both quantities show correlated patterns of cusps.

gle Coulomb peaks as a function of perpendicular magnetic field. Figure 4.10 shows such a Coulomb-peak position in V_G and the corresponding peak amplitude G versus B . Apart from the overall structure attributed to the 2DES leads, the Coulomb peaks move in a zig-zag pattern on small magnetic field scales $\Delta B \sim 100$ mT. The amplitude of these fluctuations is small compared to the total addition energy which is $\gtrsim 10$ mV in units of plunger gate voltage and which varies with B . The Coulomb-peak amplitude shows correlated fluctuations. Figure 4.11 is from a similar measurement of the same sample at different gate voltages, more clearly showing the correlation between peak position and amplitude variations. The two regimes distinguished in this Figure differ in whether spin blockade is present or not. They are further studied in the following.

Regime (1): Absence of spin blockade

Regime (1) in Figure 4.11 consists of a regular series of cusps in the Coulomb-peak position. Each steep ascent is correlated with a drop in the Coulomb peak's amplitude. During the cusp's slow descent the

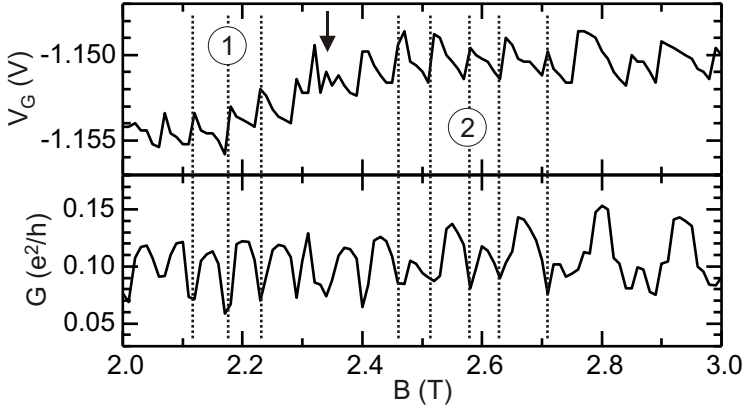


Figure 4.11: Position (in gate voltage V_G) and amplitude G of a Coulomb peak as a function of magnetic field B , similar to Figure 4.10 but showing more details. The gate voltages are also different than in the previous Figure. Two different regimes are observed, the arrow roughly marking the transition between them.

amplitude is constant. One such cycle is schematically depicted in Figure 4.12(b).

The cusps were first attributed to the frequent crossings of single particle levels in the Fock-Darwin spectrum of a quantum dot (Figure 2.4 on page 13). McEuen *et al.* soon realized that a self-consistent treatment is necessary to completely understand the experimental results [53, 34]. This is based on minimizing the total energy of all electrons on the dot under consideration of interaction as described in chapter 2.2.3. Such a treatment leads to a charge density distribution as depicted in Figure 4.12(a) for a quantum dot with two Landau levels occupied and thus consisting of two metallic regions separated by an insulating stripe (discs in Figure 4.12(b)). Slightly increasing the magnetic field in such a system increases the degeneracy of each Landau level. The charge density in the lower Landau level then increases in the centre of the dot and thus decreases at the edges because no electron has been added or redistributed. Thereby the electrostatic potential in the central metallic region is increased and in the outer metallic region is

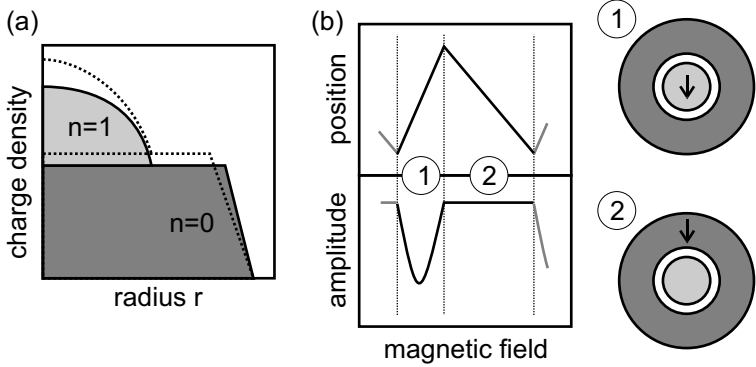


Figure 4.12: Magneto-conductance measurements of a quantum dot: (a) Sketch of a quantum dot's charge density distribution ρ with the lowest Landau level $n = 0$ completely filled and the $n = 1$ one partially filled. The dotted lines denote the charge density after slightly increasing the magnetic field. (b) Schematic Coulomb-peak position and amplitude for an electron tunnelling through (1) an inner and (2) an outer edge state in an increasing magnetic field.

decreased. Thus the rising portions of the Coulomb-peak position vs. B trace (region (1) in Figure 4.12) correspond to electrons tunnelling through the dot centre and the falling portions (region (2)) to electrons tunnelling through the edge. At the transition from a rising to a falling portion of the curve the tunnelling electron's intermediate shell changes from the inner to the outer one. No electron statically bound to the dot is redistributed in this process but just the lowest-lying free state which is utilized by the tunnelling electron. In contrast, at the transition from a falling to a rising portion of the Coulomb-peak position vs. B trace an electron trapped on the dot is redistributed from Landau level $n = 1$ to $n = 0$. The tunnelling electron now again utilizes an inner shell of the quantum dot. Thus for one complete cycle one magnetic flux quantum has to be added to the dot.

The Coulomb-peak amplitude variation with B is easily understood considering whether an inner or an outer edge state of the dot is utilized by the tunnelling electron. Inner edge states are generally tunnel

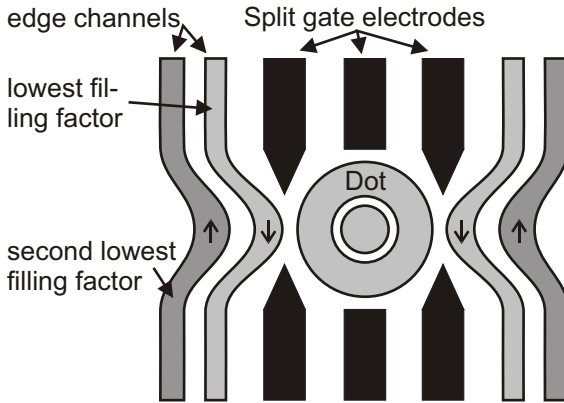


Figure 4.13: The 2DES emitter in a lateral SET becomes effectively spin polarized at high magnetic fields.

coupled to the leads more weakly compared to outer ones due to their greater spatial separation from them. Hence the tunnelling current is lowered if an inner shell of the dot is utilized by the tunnelling electron.

Regime (2): Spin Blockade

Regime (2) in Figure 4.11 is similar to regime (1) described above. It differs mainly in the Coulomb peaks' amplitude modulation where cycles with higher and lower amplitudes alternate. Less clear the same is true for the cusps in the peak positions. Thus in this regime we have to consider new cycles consisting of two old cycles from the section above.

To explain the Coulomb peak and amplitude modulation observed in this regime, McEuen's model from the above section has to be extended by the concept of spin blockade [54, 52]. Therefore we have to remember that the leads connected to the quantum dot consist of a 2DES with its peculiar behavior in a magnetic field. In particular, the emitter may become effectively spin polarized due to a spin polarized outer edge state and a tunnel coupling of the other emitter edge states to the dot too weak. This is illustrated in Figure 4.13.

The polarized outer emitter edge state corresponds to a filling factor

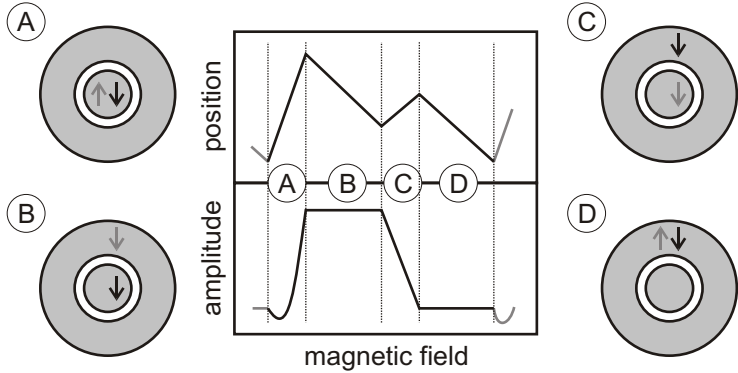


Figure 4.14: Scheme of magneto-conductance spectroscopy in a quantum dot considering spin. Coulomb-peak position and amplitude for an electron tunnelling through the inner and outer edge states in an increasing magnetic field. From (1) to (4) the spin of the tunnelling electron (grey) changes giving rise to spin blockade. The static part of the dot’s electronic configuration is sketched in black. From the spin-polarized emitter mainly spin-down electrons are available.

$\nu = 1$. This situation is not to be confused with a totally spin polarized emitter at a 2DES filling factor $\nu = 1$. Also considering edge channels corresponding to higher filling factors $\nu > 1$ more to the centre of the bulk 2DES, the emitter is not necessarily totally spin polarized despite a spin polarized outer edge. Since we do not observe a clear influence of the bulk 2DES filling factor on spin blockade, changes of the bulk 2DES filling factor in a magnetic field must mainly influence the inner edge channels. This has also been confirmed in other works [52, 55]. The formation of an isolated spin polarized edge state in the emitter depends on the smooth edge potential created by the split gate electrodes [54].

In Figure 4.14 the complete four-stage cycle is sketched together with the corresponding quantum dot configurations. The statically trapped electrons are colored in black and the tunnelling electron in grey. Region (1) and (2) make up one cycle in McEuen’s interpretation as discussed above, (3) and (4) make up another one. The tunnelling

electron always favors the spin-down state for energetic reasons whenever it is unpaired, and the spin-up state if the down-state is already occupied by an electron on the dot. From the spin-polarized emitter mainly spin-down electrons are available, again for energetic reasons. In regions (1) and (4) the tunnelling amplitude is reduced due to a spin mismatch, resulting in spin blockade.

4.4.3 Filling factor of the quantum dot

The filling factor of the quantum dot has a great influence on the magneto-conductance spectroscopy discussed above, hence it should be possible to derive an exact dot filling factor from the data. Figure 4.15 shows Coulomb-peak positions and amplitudes for three consecutive Coulomb resonances over a wide range of magnetic field. The dot is well in the Coulomb regime at $V_G \sim -1.1$ V. Clear and frequent cusps are observed up to a magnetic field of $B \sim 3.8$ T. Then the modulation vanishes. Here, the dot is assumed to be completely spin unpolarized at filling factor $\nu_{dot} = 2$. At still higher magnetic fields additional features are expected when the dot becomes spin polarized ($\nu_{dot} = 1$). However, as the height of the tunnel barriers is increased by an increasing magnetic field, the tunnel amplitude vanishes before additional features are observed.

A similar graph is shown in Figure 4.16 for a larger electron number and extremely high tunnel coupling at $V_G \sim -0.5$ V. Despite the dot is not entirely in the Coulomb regime here, similar features like in Figure 4.15 are observed. We presume a dot filling factor $\nu_{dot} = 2$ near $B \sim 4.7$ T. The modulation of both, Coulomb-peak position and amplitude, vanishes and slowly reappears at still higher magnetic fields.

In the intermediate coupling regime at $V_G \sim -0.8$ V we extract $\nu_{dot} = 2$ at $B \sim 4$ T from Figure 4.10. The vanishing of the modulation of Coulomb-peak position and amplitude at filling factor $\nu_{dot} = 2$ and its slow revival is clearly observed.

A clear indication for dot filling factors $\nu_{dot} = 3$ or $\nu_{dot} = 4$ is not observed in any of Figures 4.10, 4.15 or 4.16.

The presumed positions of filling factor $\nu_{dot} = 2$ in B are summarized by the nearly vertical dashed line at $B \sim 4$ T in Figure 4.7. The great difference of the dot filling factor compared to the bulk 2DES

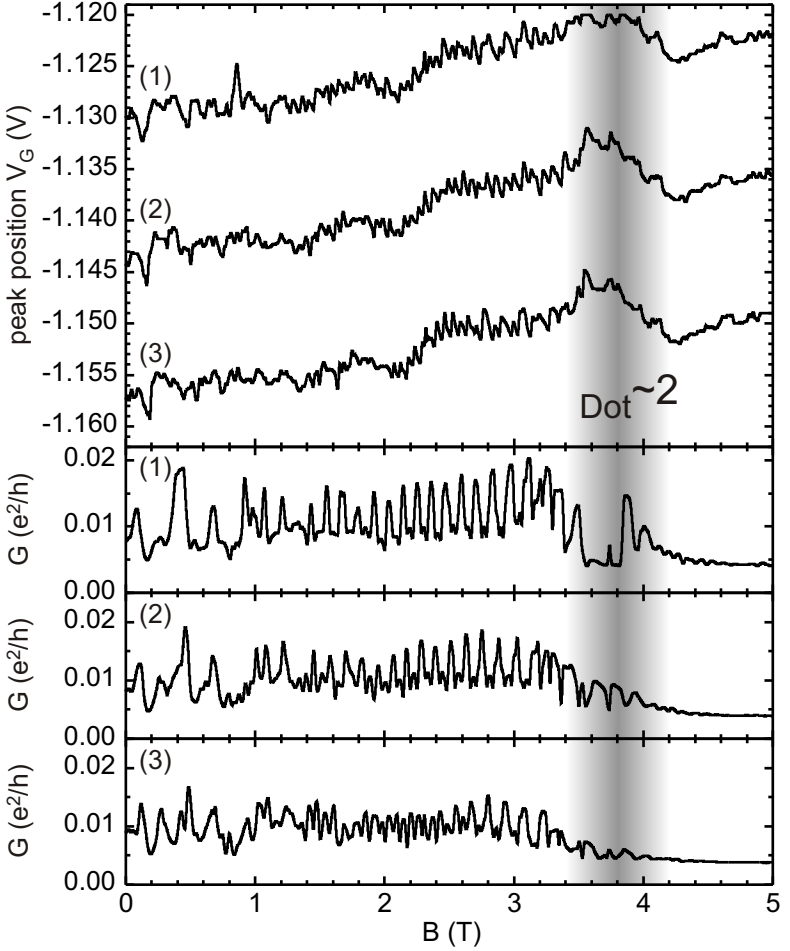


Figure 4.15: Coulomb-peak positions (in gate voltage V_G) and corresponding peak amplitudes G versus B in the Coulomb blockade regime at gate voltages $V_G \sim -1.1$ V. The dot filling factor $\nu_{dot} = 2$ is presumed in the grey area.

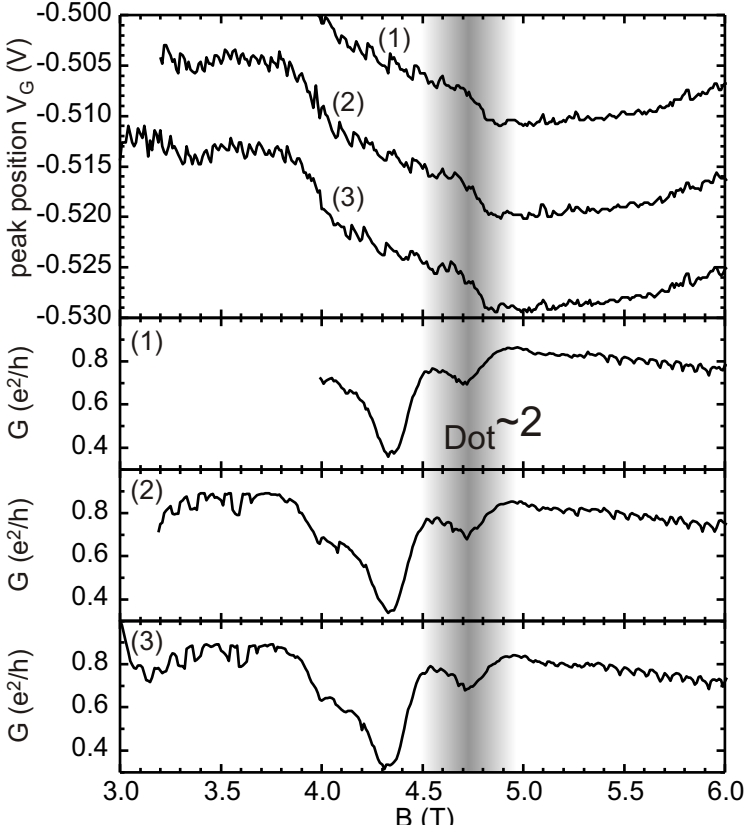


Figure 4.16: Coulomb-peak positions (in gate voltage V_G) and corresponding peak amplitudes G versus B at extremely high gate voltages $V_G \sim -0.5$ V. The dot filling factor $\nu_{dot} = 2$ lies presumably in the grey area.

filling factor by nearly a factor of two is attributed to the reduced electron density in the dot due to the presence of negatively charged gate electrodes. This was also observed in previous studies [52, 55].

In dots with a low number of confined electrons $N \lesssim 25$, it is possible to determine the exact electron number by counting the number of spin flips starting at filling factor $\nu_{dot} = 2$ needed to fully spin polarize the dot ($\nu_{dot} = 1$) [52, 56, 57]. At higher electron numbers, however, this analysis becomes unreliable [58, 59]. Then it becomes difficult to correlate all cusps in peak position to cusps in amplitude, making clear that not all relevant features can be spotted in the data [55]. Furthermore, with many electrons on the dot it is no longer obvious whether single spin flips are the only relevant electronic reconfiguration. Due to the interplay of the spin and orbital degrees of freedom of many correlated electrons other energies might become dominant over Zeeman energy [54]. Hence, at high electron numbers counting the features in Coulomb-peak position and amplitude in the $1 < \nu_{dot} < 2$ range does not give the correct total electron number on the dot.

4.4.4 Maximum density droplet

At sufficiently high magnetic fields a quantum dot reaches the equivalent of filling factor $\nu = 1$ in a bulk 2DES. In this state the dot is completely spin polarized, all electrons are aligned, and the charge distribution is compact. Single-particle states of angular momentum are successively occupied. Therefore this state is called maximum-density droplet (MDD) [60, 61]. The stability of this state is determined by a balance of the following energies:

- the confinement potential tending to compress the electron puddle,
- the repulsive Coulomb interaction between the electrons, and
- the attractive exchange interaction.

Zeeman energy and correlation effects also have to be considered. The relative strengths of these forces are tuned in a magnetic field which induces transitions between the MDD and other lower-density states.

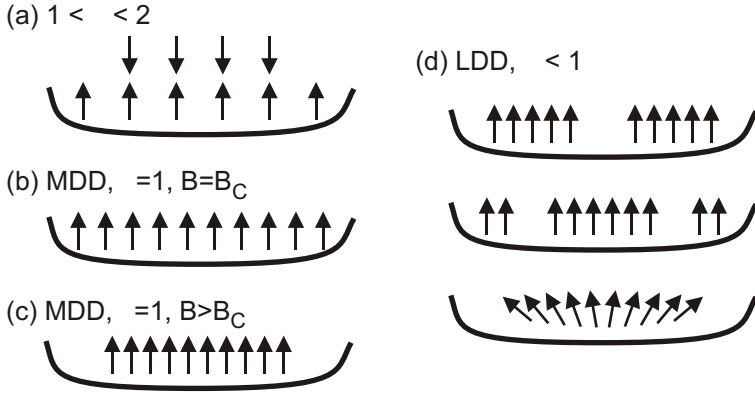


Figure 4.17: Sketch of a quantum dot's spin configuration at different filling factors as indicated. The magnetic field increases from (a) to (d).

Hartree-Fock calculations predict the formation of MDDs in fair agreement with experiments [62].

The formation of MDDs is illustrated in Figure 4.17. In (a), the dot filling factor is $1 < \nu_{dot} < 2$ and the dot is only partly polarized. By increasing the magnetic field, the electron distribution on the dot is compressed which increases Coulomb energy. Consequently electrons are redistributed from the centre to the edge of the dot flipping their spin to maximize exchange and to minimize Zeeman energy. Finally, the spin-polarized, highly symmetric MDD state is reached at $B = B_C$ (b). By further increasing B , this state becomes even more compact (c). At a certain threshold magnetic field, the Coulomb interaction becomes large enough for the MDD to break apart into a larger lower-density droplet (LDD). (d) depicts three different LDD states with holes in the electron distribution and spin textures. The stability of maximum density droplets and which LDD configuration is favored is experimentally examined in Refs. [63, 64].

Since we assume filling factor $\nu_{dot} = 2$ at a magnetic field of $B \sim 4.7$ T, $\nu_{dot} = 1$ is expected at $B \sim 9$ T. Only at extremely high plunger gate voltages of $V_G \sim -0.5$ V the tunnel coupling is sufficiently high to investigate electronic transport even at these high magnetic fields.

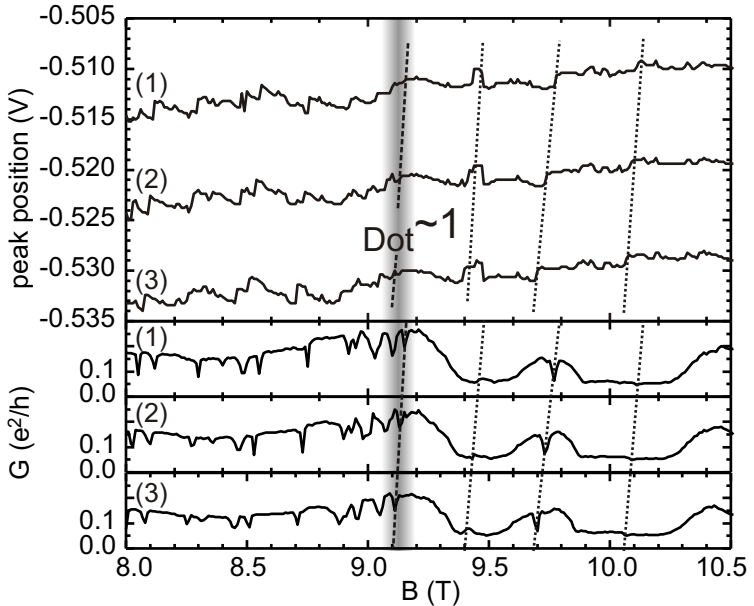


Figure 4.18: Coulomb-peak positions and amplitudes versus B at extremely high magnetic fields. At the dashed line at $B \sim 9.2$ T, a maximum density droplet corresponding to $\nu_{dot} = 1$ is formed in the quantum dot. At still higher magnetic fields marked by dotted lines it decays into lower density droplets.

As shown in Figure 4.18, relatively regular cusps in Coulomb-peak position and amplitude versus B are observed up to a magnetic field of $B \sim 9.2$ T (dashed line). This is attributed to the spin polarization of the dot at $1 < \nu_{dot} < 2$. We identify filling factor $\nu_{dot} = 1$ at the dashed line. The observation of filling factor $\nu_{dot} = 1$ at $B \sim 9.2$ T confirms the identification of filling factor $\nu_{dot} = 2$ at $B \sim 4.7$ T.

Due to the high number of electrons on our dot ($N > 100$) it is not clear whether the ground state is really a compact MDD state or a less compact LDD state as the width of the MDD region becomes narrower in B with increasing electron number [60, 61, 62, 64]. In the figure, a flat region with only very few, less regular features follows (dotted lines).

Sample	1129-8-7.3	1129-1-2.2
Regime	$V_G \sim -1.15$ V	$V_G \sim -0.65$ V
from $\alpha_G \Delta V_G$ in Coulomb oscillations		
charging energy U	0.59 meV	4.2 meV
total capacitance $C_{\Sigma,G}$	270 aF	38 aF
gate capacitance	12 aF	5 aF
from temperature dependence of Coulomb lineshapes		
lever arm α_G	0.045	—
intrinsic linewidth $\hbar\Gamma$	100 μ eV	—
from the Coulomb diamond width ΔV_{SD}		
charging energy U	0.60 meV	4.5 meV
total capacitance $C_{\Sigma,SD}$	270 aF	36 aF
from slopes in Coulomb diamonds		
lever arm α_D	0.3	0.4
lever arm α_G	0.045	0.13
drain capacitance C_D	90 aF	15 aF
gate capacitance C_G	12 aF	4.8 aF
from excitation spectroscopy		
excitation energy $\Delta\varepsilon$	~ 100 μ eV	~ 1 meV

Table 4.1: Data extracted from Coulomb-blockade measurements for two characteristic SET samples.

These are attributed to the infrequent transitions between MDD and various LDD states.

4.5 Conclusions

A summary of the results obtained in the Coulomb-blockade regime is provided in tables 4.1 and 4.2. They stem from measurements of Coulomb oscillations in the linear conductance at base temperature, from the variation of the Coulomb-resonance lineshape as a function

Dot filling factor	$\nu_{dot} = 1$	$\nu_{dot}=2$
$V_G \sim -1.1$ V	n. o.	3.8 T
$V_G \sim -0.8$ V	n. o.	4.0 T
$V_G \sim -0.5$ V	9.2 T	4.7 T

Table 4.2: Results from magneto-transport investigations on sample 1129-8-7.3. The approximate magnetic fields of integer dot filling factors are given for three gate voltage regimes. $\nu_{dot} = 1$ is observed only at $V_G \sim -0.5$ V (n. o. in the other rows means not observed).

temperature and from the Coulomb diamonds probed in nonlinear conductance measurements. Key parameters are different characteristic capacitances in the SETs, their lever arm, excitation energy and intrinsic linewidth. A number of capacitances of the SET is determined in different types of measurement and cross-checked. The results agree very well. The magnetic field values for the assumed positions of the dot filling factors $\nu_{dot} = 1$ and $\nu_{dot} = 2$ are independently extracted from magneto-conductance measurements. The fields for $\nu_{dot} = 1$ and $\nu_{dot} = 2$ are consistent. In addition, spin blockade observed in sample 1129-8-7.3 provides clear evidence of an effective spin polarization in the emitter.

The results from sample 1129-8-7.3 were roughly reproduced in another quantum dot, while the data from 1129-1-2.2 represents a random but well-defined smaller system. Sample 1129-8-7.3 is used in the experiments in the rest of this work.

In the discussion on magneto-transport, some fundamental questions on the state of a multi-electron dot in high magnetic fields were addressed. Today, the formation of maximum- and lower-density droplets and their transitions are not fully understood. In the discussion on spin blockade a better understanding of the emitter edge states in the smooth potential created by the split gates would be desirable.

To conclude, sample 1129-8-7.3 has been thoroughly characterized in Coulomb and magneto-transport measurements. Moreover, important concepts have been introduced and applied to this dot. In the classical Coulomb-blockade regime this multi-electron dot is understood very well which allows to explore new regimes in a controlled manner.

5 Kondo regime

In the split-gate single-electron transistors introduced in the previous chapters a great number of parameters can be controlled over a wide range. This allows to investigate novel transport regimes completely different from the well-known Coulomb blockade. The present chapter is devoted to one such alternative transport regime where a strong coupling of the quantum dot to its leads gives rise to the Kondo effect, a many-body interaction phenomenon between dot and lead electrons.

After an introduction to the Kondo effect and its theoretical description this framework is applied to the present quantum dot. Typical fingerprints of a Kondo effect are identified and compared to the features in the measurements at zero magnetic field. The influence of gate voltage and magnetic field on the Kondo effect in our highly correlated multi-electron quantum dot is studied in detail. Finally, Coulomb-peak positions and amplitudes are analyzed in the Kondo regime, allowing to determine how the degree of spin polarization in the emitter affects a Kondo effect.

5.1 Introduction to the Kondo effect

The Kondo effect describes the influence of a magnetic impurity on a sample's resistivity as a function of temperature. The Kondo effect has attracted theorists and experimentalists alike in the past [65] and is the subject of continuous interest [66] due to its recent observation in semiconductor quantum dots. This section gives a short review of Kondo physics and its application to quantum dots.

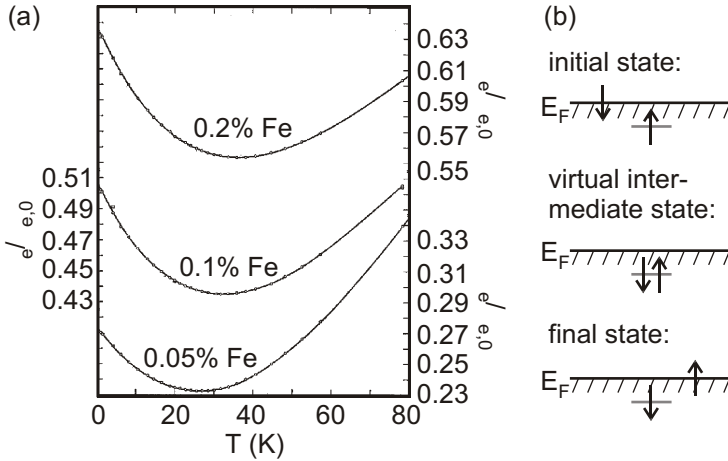


Figure 5.1: Kondo effect in magnetic alloys: (a) Relative resistivity of a copper sample for different iron impurity concentrations as a function of temperature [67]. (b) Scheme of the mechanism of the Kondo effect. An electron experiences a spin-flip scattering process at a magnetic impurity (see text).

5.1.1 Low-temperature resistivity in the presence of magnetic impurities

We usually understand the resistivity of pure metals to be composed of a phonon contribution which increases with temperature plus a temperature independent value due to imperfections in the lattice. In the 1930s one was convinced to have found deviations from this behavior which were later found to be caused by magnetic impurities in the samples. The temperature dependence of the resistivity found in the 1930's experiments is depicted in Figure 5.1(a), showing an unexpected minimum and a rise in resistivity for decreasing temperature. This behavior was later named Kondo effect.

It was 1964 that J. Kondo proposed his s-d model which is able to explain the resistivity minimum. He assumed that there were magnetic moments in the sample which he associated with spins \mathbf{S}_{imp} at the impurities. Each impurity spin is coupled via an exchange interaction J

with incident conduction electrons with spin \mathbf{S}_{in} [10]. With an anti-ferromagnetic coupling $J < 0$, $E_{int} = -2J\mathbf{S}_{imp} \cdot \mathbf{S}_{in}$ describes this interaction. Using third order perturbation theory, Kondo showed that this interaction leads to extra scattering of the conduction electrons near the Fermi level and an additional contribution to the resistivity

$$\rho_e \propto J \cdot \ln(T).$$

This term together with the phonon contribution is able to explain the resistivity minimum. For $T \rightarrow 0$, however, it becomes unphysical and diverges. To describe also the extreme low-temperature properties correctly, more sophisticated methods like the numerical renormalization-group technique developed by Wilson [68] or the Bethe ansatz [69, 70, 71] are needed. Wilson was rewarded with a Nobel prize for his work in 1982. A review on the theory of the Kondo problem is found in [72, 73].

The interaction constant J in the Kondo model sets the energy scale of the Kondo effect. It is often expressed in terms of the so-called Kondo temperature T_K which can be determined from experimental data more easily. While the Kondo effect determines the conductance at low temperatures below T_K , at temperatures above T_K the interaction of impurity and conduction electrons is disturbed by thermal energy.

Figure 5.1(b) schematically depicts the scattering process behind the Kondo effect: An incident electron with spin down $|\downarrow\rangle$ at the Fermi level E_F and an electron with opposite spin $|\uparrow\rangle$ trapped at a magnetic impurity form a virtual intermediate state with both electrons on the impurity site. This state is forbidden since all accessible states up to the Fermi level are already occupied. Within a maximal lifetime determined by the Heisenberg uncertainty relation it decays into the impurity being occupied by the $|\downarrow\rangle$ electron and the $|\uparrow\rangle$ electron at the Fermi level. Thus the spin on the impurity site has flipped. In the Kondo ground state of the system, the impurity spin is continuously flipped in such processes and thus the conduction electrons completely screen the impurity spin. This additional scattering process gives rise to the increased resistivity at low temperatures.

The Kondo ground state can also be interpreted as a correlated state consisting of singlets between the single impurity electron and

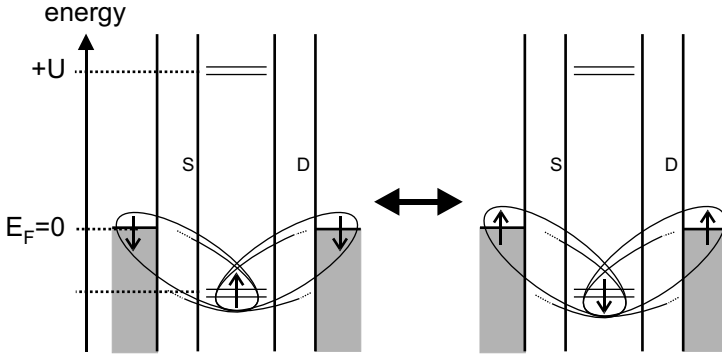


Figure 5.2: Sketch of the Anderson impurity model with the Kondo singlets marked by the ellipses. The spin-degenerate level at ε is singly occupied. To add another electron the interaction energy U has to be employed. The system fluctuates between both configurations shown.

many reservoir electrons. The Kondo temperature T_K then describes the binding energy of the singlets. The vanishing of the Kondo effect at high temperatures $T > T_K$ is understood as the singlets being broken up by thermal energy. At low temperatures $T < T_K$, the singlets form the so-called Kondo cloud. Its extension is estimated

$$l_K = \frac{\hbar v_F}{k_B T_K} \quad (5.1)$$

with Fermi velocity $v_F = \hbar k_F / m^*$ and Fermi wave vector $k_F = \sqrt{2\pi n_e}$. n_e denotes the electron density. The size of the Kondo cloud gives the extension of the singlet states formed by impurity and conduction electrons.

5.1.2 Anderson impurity model in quantum dots

A description of a Kondo system equivalent to the one discussed above was introduced in 1961 by P. W. Anderson [74]. He originally considered only one electron reservoir, but we focus on the extended version of his model including a second reservoir better resembling quantum dots with two leads. This model is sketched in Figure 5.2. We model

the magnetic impurity as a twofold (spin-) degenerate energy level ε below the Fermi level E_F of two reservoirs. It is singly occupied. A Coulomb energy U large compared to all other relevant energy scales has to be employed to bring a second electron onto the impurity site, thus $\varepsilon + U > E_F$. The impurity is tunnel coupled to the source and drain electron reservoirs with couplings Γ_S, Γ_D . Large couplings allow the formation of singlet states consisting of the impurity spin and reservoir spins. The impurity spin is screened in these states, thus the system fluctuates between both configurations shown in the figure. This allows transport of electrons from one reservoir to the other one despite the impurity level ε not being aligned with the Fermi levels.

The equivalence of the Anderson model and the Kondo system was first discussed by Schrieffer and Wolff [75]. We use a definition of the Kondo temperature according to Haldane [76, 77] which allows to determine T_K from the Anderson model parameters. For a Fermi energy $E_F = 0$ and a spin-degenerate level below the Fermi energy at $\varepsilon < 0$ (Figure 5.2) he found:

$$T_K = \frac{\sqrt{U\hbar\Gamma}}{2k_B} \cdot \exp\left(\pi \frac{\varepsilon(U + \varepsilon)}{U\hbar\Gamma}\right). \quad (5.2)$$

This allows a direct mapping between both models. The dependence of the Kondo temperature T_K on the model parameters will be discussed further in a later section.

The possibility of a mapping of the Anderson model to quantum dots was realized in 1988 [11, 12, 78]. Like a quantum dot, an Anderson model consists of reservoirs (leads), tunnel barriers and the impurity (dot) itself. However, in quantum dot experiments the formation of singlet states and the increased scattering due to the Kondo effect increases the conductance and not the resistivity. This is because quantum dot experiments measure the conductance *through* the essentially non-conducting impurity, in contrast to the traditional Kondo experiments probing a *perturbation* of the conductance in an anyway conducting metal. After the discovery of Kondo physics in defects in metal point contacts in 1992 [79], it was until 1998 that the Kondo effect was observed in intentional, well-controlled quantum dots for the first time [13, 14, 15, 16]. Despite some deviations from nearby levels

[80], these experiments closely resembled the Anderson model. In recent experiments a Kondo effect was not only observed in traditional quantum dots but also in carbon nanotube SETs [18] and single-atom SETs [81].

Anderson Hamiltonian

It is instructive to consider the Hamiltonian of the Anderson model. The Hamiltonian is constructed from the components of the model, namely reservoirs (\mathbf{H}_r), impurity (\mathbf{H}_i) and the tunnel coupling in between (\mathbf{H}_t):

$$\mathbf{H} = \mathbf{H}_r + \mathbf{H}_i + \mathbf{H}_t. \quad (5.3)$$

The electron reservoirs are described by

$$\mathbf{H}_r = \sum_{r,k,s} \varepsilon_{rks} \mathbf{a}_{rks}^+ \mathbf{a}_{rks}. \quad (5.4)$$

The single-particle creation operator \mathbf{a}_{rks}^+ generates an electron with energy ε_{rks} in reservoir $r \in \{\text{source, drain}\}$ in the momentum eigenstate k and with spin $s = \pm 1/2$. \mathbf{a}_{rks} is the corresponding annihilation operator. $\mathbf{n}_{rks} = \mathbf{a}_{rks}^+ \mathbf{a}_{rks}$ gives the number of particles in state rks .

The impurity is characterized by the Hamiltonian

$$\mathbf{H}_i = \sum_s \varepsilon_s \mathbf{c}_s^+ \mathbf{c}_s + U \mathbf{c}_{+1/2}^+ \mathbf{c}_{-1/2}^+ \mathbf{c}_{-1/2} \mathbf{c}_{+1/2}. \quad (5.5)$$

Here, \mathbf{c}_s^+ and \mathbf{c}_s are the corresponding creation and annihilation operators with $\mathbf{n}_s = \mathbf{c}_s^+ \mathbf{c}_s$ giving the number of electrons with spin s on the impurity. The first term describes the single particle energies with $\varepsilon_{+1/2} = \varepsilon_{-1/2} = \varepsilon$ in the degenerate case considered here. The second term accounts for Coulomb interaction and due to the large charging energy U prevents double occupancy of the impurity.

Since in a tunnelling process an electron in a reservoir is annihilated and another one on the impurity is created or vice versa, the corresponding Hamiltonian is

$$\mathbf{H}_t = \sum_{rks,q} t_{rks,q} \mathbf{a}_{rks} \mathbf{c}_q^+ + h.c. \quad (5.6)$$

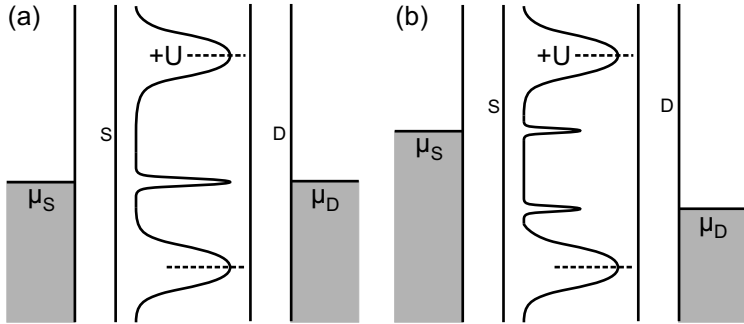


Figure 5.3: Schematic spectral density in the Anderson impurity model for (a) zero bias voltage and (b) finite bias voltage.

The tunnel matrix element $t_{rks,q}$ parameterizes this process and contains contributions from $\Gamma_{S,D}$.

All key ingredients of the Anderson model are found again in this Hamiltonian.

Spectral density and Kondo conductance in quantum dots

The spectral density $A(E)$ of a quantum dot is an extension to the concept of a local density of states (LDOS). It is based on the observation that a Kondo system acts as if the density of states had a resonance at the Fermi surface [73]. Despite a LDOS the spectral density reflects correlation with the leads and hence a Kondo effect. Its value at the Fermi level determines the conductance of the SET. A typical spectral density for a dot in the Kondo regime is depicted in Figure 5.3(a). It consists of two wide peaks corresponding to subsequent Coulomb resonances of a quantum dot and a sharp peak for the Kondo resonance in between. The Kondo peak is pinned at the Fermi levels of the reservoirs and gives rise to a finite Kondo conductance in a quantum dot at zero bias voltage even in Coulomb blockade valleys. In the unitary limit, this Kondo conductance can reach up to $2e^2/h$ [82].

Out of equilibrium at finite bias voltage, the sharp Kondo peak splits into two, one pinned at each reservoir's Fermi level (Figure 5.3(b)). The conductance of the impurity is zero in this situation which can

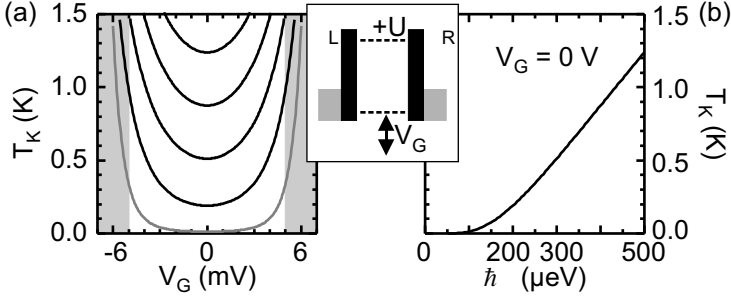


Figure 5.4: Dependence of the Kondo temperature T_K on the Anderson model parameters for a realistic SET ($\alpha = 0.05$, $U/\alpha = 12$ mV). (a) The dot energy level ε is tuned by varying the SET gate voltage V_G for Coulomb-resonance linewidths between $\hbar\Gamma = 100$ μeV (grey) and 500 μeV (topmost curve). The model becomes invalid in the grey areas near the Coulomb resonances at $V_G = \pm 6$ mV. (b) T_K strongly depends on the tunnelling rate Γ ($\varepsilon = -U/2$, $V_G = 0$). Inset: Parameters in the Anderson impurity model.

be seen from energy conservation when an electron is transferred from one reservoir to the other in a Kondo scattering process. Detailed calculations are found in [83, 84, 85, 86].

5.1.3 Estimation of the Kondo temperature

The Kondo effect reigns the conductance of a quantum dot at temperatures $T < T_K$. In this section, we estimate the Kondo temperature T_K for our quantum dot with Haldane's equation 5.2. We use the parameters found from measurements in the Coulomb-blockade regime discussed in chapter 4 and summarized in table 4.1 on page 62. Figure 5.4 depicts the Kondo temperature as a function of gate voltage V_G and Coulomb-resonance linewidth $\hbar\Gamma$.

In Figure 5.4(a) T_K exhibits a minimum in the middle of the Coulomb valley at $V_G = 0$ ($\varepsilon = -U/2$) and strongly rises near the resonance positions at $V_G = \pm 6$ mV ($\varepsilon = 0, U$). Near the resonances, the so-called mixed valence and empty orbital regimes are entered and our description of T_K becomes invalid. The mixed valence regime is entered when

the Kondo resonance comes into the vicinity of a Coulomb resonance [87, 88, 89].

The dependence of T_K on the resonance linewidth $\hbar\Gamma$ is shown in Figure 5.4(b) and is rather strong. T_K rises when increasing $\hbar\Gamma$, exhibiting a nonlinearity for an experimentally realistic linewidth of $\hbar\Gamma \sim 200 \mu\text{eV}$ (for the linewidth compare Figure 4.3 and the corresponding discussion in chapter 4.2). Because of the large error inherent when determining the linewidth this makes it difficult to predict an exact Kondo temperature from the quantum dot parameters U and $\hbar\Gamma$. $U = 600 \mu\text{eV}$ and $\hbar\Gamma = 200 \mu\text{eV}$ are realistic values for our quantum dot as determined in chapter 4. We get $T_K = 190 \text{ mK}$ in the centre of the Coulomb valley ($\varepsilon = -U/2$) and 340 mK at $\varepsilon = -U/4$. We cannot expect to find exactly these values in our quantum dot, but a Kondo temperature of a few hundred millikelvin seems realistic. Such temperatures are within reach of low temperature experiments.

5.1.4 Kondo resonances with lifted degeneracy

Until here we discussed Kondo resonances only for a spin degenerate level. But Kondo resonances might also be observed for non-degenerate levels. For simplicity, we consider a magnetic field B applied to the spin-degenerate Anderson model discussed above. Zeeman splitting of the $|\uparrow\rangle$ and $|\downarrow\rangle$ states then lifts the degeneracy. An energy difference $\Delta\varepsilon = g\mu_B B$ between the contributing levels inhibits the formation of a Kondo resonance at zero bias voltage. However, for finite bias voltages $V_{SD} = \pm\Delta V_{SD} = \pm\Delta\varepsilon/e$ the energy difference of the reservoirs can compensate for this splitting. Then the Kondo resonance is split with peaks at the respective bias voltages V_{SD} [13, 85, 90]. Energy is conserved in spin-flip processes analogous to Figure 5.1. Figure 5.5 shows the formation of spin singlets in such a situation and the resulting source-drain voltage dependent differential conductance.

Even when degeneracy is lifted, for the observation of a Kondo effect the other prerequisites must still hold. In particular the participating levels must differ in spin as the Kondo effect is a spin effect. Obviously this condition is fulfilled for the Zeeman split levels discussed above. The coupling of the levels to the leads must also be sufficiently strong.

Finally, we want to introduce another, more complicated but never-

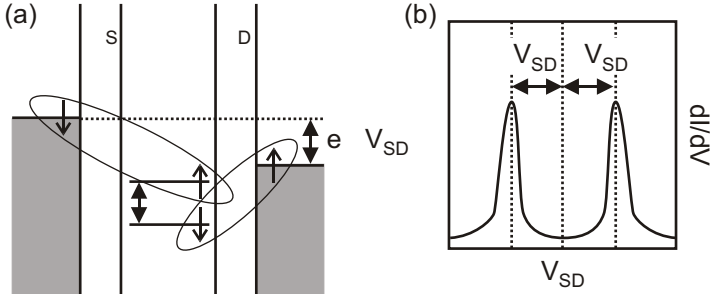


Figure 5.5: (a) Kondo resonance with lifted degeneracy. The reservoirs differ in chemical potential by the same energy as the split dot levels, $\Delta\varepsilon = e\Delta V_{SD}$. (b) In the resulting source-drain voltage dependent differential conductance two resonances at $\pm\Delta V_{SD}$ are found instead of the zero-bias resonance.

theless highly relevant situation where a Kondo effect involving non-degenerate levels might arise. It is linked to inelastic cotunnelling through excited states [38, 17]. Inelastic cotunnelling was introduced in chapter 2.3.5. We refer to process (4) in Figure 2.11 on page 26. At the onset of inelastic cotunnelling the source drain voltage V_{SD} just compensates the energy difference between the two contributing levels which are situated below the Fermi energy. From the energy conservation arguments presented above this may give rise to a Kondo effect. Such a Kondo effect would become visible in differential conductance as a peak at the edge of the inelastic cotunnelling step. In this Kondo effect, the finite source-drain voltage compensates for the lack of degeneracy.

5.1.5 Kondo effect for odd and even electron numbers

In a simple spin-1/2 Anderson model one would expect a Kondo effect for an odd number of electrons N on the dot because of the unpaired spin. Then in a single particle model we neglect all electrons on the dot but the last one and apply the Anderson model. For an even number of electrons, one might naively think that all spins are paired and thus a Kondo effect has to be absent. Indeed such an odd-even behavior

was found in the first observations of Kondo physics in quantum dots [13, 14].

However, it later became clear that such a modulation of the Kondo effect with electron number N depends on the details of the involved quantum dot ground states [56], in particular on the question whether electrons are added to the dot according to Hund's rule or not. This depends on the magnitude of exchange energy in the dot compared to the single particle level spacing [2]. According to Hund's rule, the spin of electrons added to a dot is aligned to maximize the total spin. Then unpaired spins are present for even as well as odd electron number, and so is the Kondo effect. Both situations, absence as well as presence of Hund's rule, were observed in quantum dots [91] which affects the odd-even modulation of a Kondo effect.

5.1.6 Deviations from the spin-1/2 Anderson model

Although the Anderson model describes the situation in quantum dots in certain regimes very well, such a resemblance is never perfect. Deviations from the model are e. g. observed when the coupling of the dot to the leads is not small compared to the electronic level spacing and the multi-level regime is entered [88, 92, 93, 94]. Another deviation was already mentioned: When the dot is tuned close to a Coulomb resonance [87, 89] the mixed valence regime is entered.

Coupling of several electron spins

The splitting of Kondo resonances with $2e\Delta V_{SD} = 2g\mu_B B$ in a magnetic field was used as a test in the first Kondo experiments in SETs [13, 14]. It is a typical property of the spin-1/2 Kondo effect discussed so far. In particular in quantum dots containing many electrons, however, the single-electron approximation breaks down. The spin structure becomes more complicated because of many correlated electrons on the dot coupling to a $S \neq 1/2$ state. A magnetic field influences this correlated state in a nontrivial manner.

The simplest example which is analytically understood is a two electron system coupling to singlet ($S = 0$) and triplet states ($S = 1$) [95, 96, 97, 98, 99, 100]. The degeneracy of these states is tuned in

a magnetic field with a B -dependence completely different from the spin-1/2 situation. At singlet-triplet degeneracy, a strong Kondo effect is found [17, 18].

With more than two electrons even more complex magneto-conductance patterns are theoretically predicted [101, 102] and experimentally observed [103, 104]. These experiments will be discussed in detail in section 5.5. The properties of the Kondo effect in such a situation deviate from what is expected from the spin-1/2 Anderson model since the single-electron approximation no longer holds.

5.2 Quantum dot parameters

For the Kondo experiments we focus on structure 1129-8-7.3 thoroughly characterized in the previous chapter (Tables 4.1 and 4.2). Similar results were obtained for another sample (1129-1-2.2) in a different measurement.

Typical energies involved in tunnelling through dots resembling the Anderson impurity model can be depicted like in Figure 5.6(a). The situation in the dot under study here, however, is more like in Figure 5.6(b). Different from the Coulomb blockade regime observed at $V_G \lesssim -1$ V, to observe a Kondo effect the coupling of the dot to the leads must be large. Therefore the plunger gate voltage was tuned to $V_G \gtrsim -1$ V, which due to the spatial proximity to the tunnel barriers results in the desired increased coupling, $\hbar\Gamma \approx 250 \mu\text{eV}$. The charging energy in this regime is $U \approx 500 \mu\text{eV}$. Due to the large size of the dot, the internal level spacing $\Delta\varepsilon$ is comparably small, $\Delta\varepsilon \approx 100 \mu\text{eV}$ (equation 2.3), so that $\Delta\varepsilon \lesssim \hbar\Gamma$. Kondo as well as mixed valence effects should play a role. In addition, the large number of electrons in our dot provides electronic ground states complex enough to allow a variety of Kondo effects beyond spin-1/2 like a singlet-triplet Kondo effect or even more complicated ones.

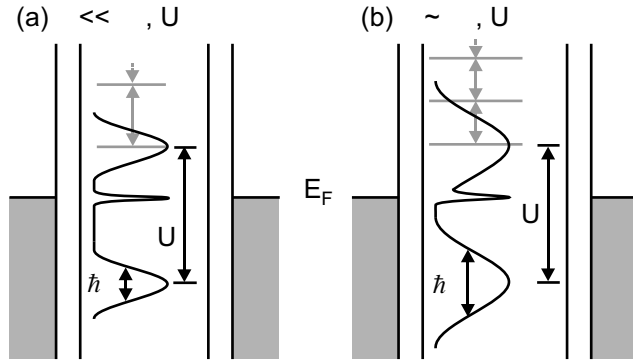


Figure 5.6: Schematic energy diagrams of quantum dots with charging energy U , level spacing $\Delta\varepsilon$ and tunnel coupling Γ . (a) A dot in the Kondo regime with the characteristic narrow resonance in the density of states at the Fermi energy E_F . (b) The situation in our dot, where U , $\Delta\varepsilon$ and $\hbar\Gamma$ are of similar magnitude.

5.3 Kondo effect at zero magnetic field

In this chapter, the Kondo effect in a quantum dot will be investigated at zero magnetic field. Nonlinear and temperature dependent differential conductance measurements will be discussed.

5.3.1 Nonlinear conductance

The simplest experimental signature of a Kondo effect in a quantum dot is the finite conductance peak as a function of bias voltage at $V_{SD} = 0$ within a Coulomb-blockade valley. We observe this signature in nonlinear differential conductance measurements shown in Figure 5.7. The grey scale plot is from the same measurement as the Coulomb diamonds in Figures 4.4 and 4.6(a). In several consecutive Coulomb diamonds a clear Kondo signature is visible. We observe a distinct zero-bias peak in the middle of a Coulomb blockade valley in the exemplary cut at $V_G = -0.9965$ V. This zero-bias anomaly is absent in the cuts at $V_G = -0.9095$ V and -1.0475 V where the zero-bias Kondo effect has vanished. As the Kondo resonance extends over sev-

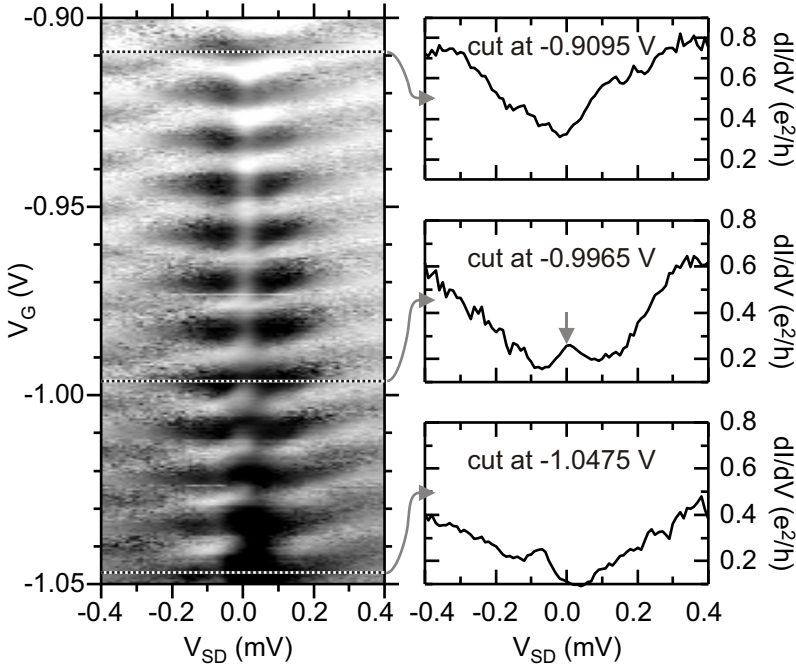


Figure 5.7: Kondo effect in nonlinear differential conductance. The Coulomb diamonds in the grey scale plot on the left (log scale with black: $dI/dV_{SD} = 0.2 e^2/h$ and white: $dI/dV_{SD} = 0.8 e^2/h$) exhibit a Kondo resonance at zero bias voltage in subsequent valleys. The zero-bias anomaly is pronounced in the $V_G = -1$ V to -0.92 V range and vanishes below $V_G = -1.0475$ V and above $V_G = -0.9095$ V as visible from the cuts on the right. The Kondo resonance is marked by an arrow in the middle cut.

eral consecutive Coulomb valleys, electrons are not added pairwise and the dot is filled according to Hund's rule.

A side peak at $V_{SD} \approx -80 \mu\text{V}$ becomes apparent in the Coulomb blockade valleys at plunger gate voltages $V_G \leq -1.02 \text{ V}$ when the central Kondo peak has vanished. This peak is located at the edge of a step in the differential conductance. The step is probably due to inelastic cotunnelling through an excited state. We recall an excitation energy of roughly $\Delta\varepsilon \approx 100 \mu\text{eV}$. We attribute the peak to a Kondo effect involving the excited state and the ground state as described in section 5.1.4 on page 73. In Figure 5.7 this is observed much more clearly for negative bias voltages than for positive ones because of an asymmetry in the tunnelling barriers.

5.3.2 Temperature dependence

Measurements of the linear conductance versus temperature provide an additional method to check for a Kondo effect. Figure 5.8(a) shows such measurements in the gate voltage range already exploited in Figure 5.7. Since the focus is on the Kondo effect we are particularly interested in the Coulomb valleys. Therefore the valley conductance is further investigated in Figure 5.8(b) for the valleys marked in (a).

At $V_G \sim -1.05 \text{ V}$ and $V_G \sim -0.9 \text{ V}$ the Coulomb valleys exhibit the temperature dependence expected between wide Coulomb peaks. The conductance rises when increasing temperature. Due to the high coupling $\hbar\Gamma$ the Coulomb peaks are extremely wide and even overlap. Thus at increasing temperature when the peaks become even wider the valley conductance increases. We will name this contribution Coulomb conductance.

For gate voltages between -1 V and -0.92 V a reverse temperature dependence is observed, particularly pronounced around $V_G \sim -0.975 \text{ V}$. This falling conductance with increasing temperature is a clear signature of a Kondo effect. As known from chapter 5.1 the conductance in a quantum dot is increased due to the Kondo effect unless the latter is destroyed by thermal energy equal to or larger than the singlet binding energy, the Kondo temperature T_K . With temperature increasing further, in this gate voltage range the decreasing Kondo conductance is dominated by the increasing Coulomb conductance.

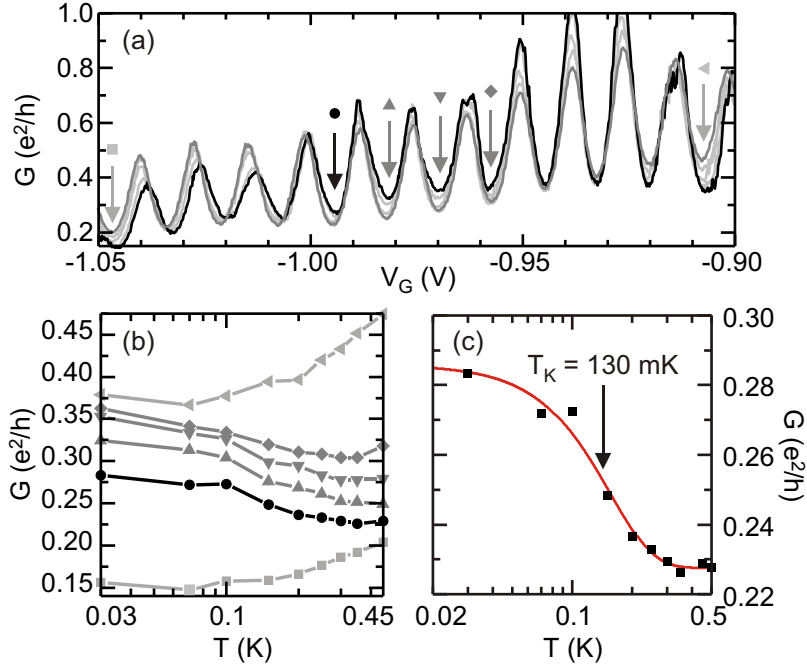


Figure 5.8: Temperature dependence of Kondo resonances: (a) Linear conductance as a function of plunger gate voltage V_G for temperatures $T = 30$ mK (black), 100 mK, 200 mK, 300 mK (light grey) and 450 mK (dark grey). (b) Temperature dependent linear conductance at the gate voltages marked in (a). (c) A fit of the black curve from (b) to equation 5.7 extended by a constant background conductance yields a Kondo temperature of $T_K = 130$ mK.

The exact temperature dependence of a Kondo resonance was calculated using a numerical renormalization group ansatz by Costi *et al.* [87]. They found a scaling behavior of the normalized conductance as a function of normalized temperature. The empirical formula

$$G(T) = G_0 \left(\frac{1}{1 + (T/T'_K)^2} \right)^s \quad (5.7)$$

with

$$T'_K = \frac{T_K}{\sqrt{2^{1/s} - 1}}$$

provides a good fit to their theory [105] and has become a widely accepted Kondo fingerprint in recent literature, starting with [89]. As shown in Figure 5.8(c) for the black curve in Figure 5.8(b) ($V_G = -0.995$ mV), our data is fit rather well by this formula if we assume a temperature independent background conductance A . The parameters from the fit are $A = (0.228 \pm 0.04) e^2/h$, $G_0 = (0.058 \pm 0.005) e^2/h$, $T_K = (0.13 \pm 0.01)$ K and $s = 5.5 \pm 4.5$. The Kondo temperature T_K from the fit describes the point where the Kondo conductance has reached one half of its maximum value quite well. An increasing background better resembling the Coulomb contribution in the lowest ($V_G = -1.045$ V) trace in Figure 5.8(b) yields a slightly larger value for T_K , thus we assume a Kondo temperature between 0.1 K and 0.2 K. The dimensionless parameter s is claimed to have a characteristic value of 0.2 [89] or 0.25 [106] for a spin-1/2 Kondo effect. Obviously, the large error of our fit does not allow further conclusions from this parameter.

We compare the Kondo temperature from the measurement to the Kondo temperatures calculated in section 5.1.3 for realistic dot parameters: For a charging energy U between 500 μeV and 600 μeV and a coupling between $\hbar\Gamma = 150$ μeV and 250 μeV we get a Kondo temperature between $T_K = 100$ mK and 400 mK. Calculated and experimental Kondo temperature roughly agree, both are on the range of a few hundred millikelvin.

5.4 Kondo effect at finite magnetic fields

In this chapter, we employ a magnetic field perpendicular to the quantum dot to tune the Kondo effect. We don't observe the Zeeman splitting expected for a spin-1/2 Kondo resonance because of the large number of correlated electrons on our dot. Instead we find a strikingly regular modulation of the Kondo effect in our magneto-conductance measurements. This modulation is analyzed with respect to its periodicity and the Kondo effect leading to this pattern is characterized.

5.4.1 Overview of the magneto-modulated Kondo conductance

Figure 5.9 shows an overview of the linear magneto-conductance G versus plunger gate voltage V_G and perpendicular magnetic field B . For magnetic fields $B \gtrsim 1$ T a diagonal stripe pattern is clearly visible. The striking regularity of this pattern vanishes only for low fields and strong coupling (upper left region in the figure) where $G(B, V_G)$ becomes rather complicated. This can be attributed to the increased influence of disorder in this regime. Chaotic effects typical for open quantum dots might also play a role. We will discuss the origin of the regular pattern - a modulated Kondo effect - in two different regimes of magnetic field in sections 5.4.2 and 5.4.3 below but will first focus on its periodicity.

Tile periodicity

The measured conductance was Fourier transformed along the B axis for several gate voltages V_G . Figure 5.10(a) shows a typical result of the power spectrum obtained. A clear peak is observed at a frequency of $f = 9.3 \text{ T}^{-1}$ corresponding to a periodicity of $\Delta B \approx 110 \text{ mT}$. Each such transformation exhibits such a peak, from which we find a periodicity varying from $\Delta B_1 = 130 \text{ mT}$ at $V_G = -1.2 \text{ V}$ to $\Delta B_2 = 75 \text{ mT}$ at $V_G = -0.4 \text{ V}$.

We have identified the periodicity with the addition of one flux quantum to the dot: $N_\phi = 1$ flux quanta ϕ_0 added per stripe period lead to

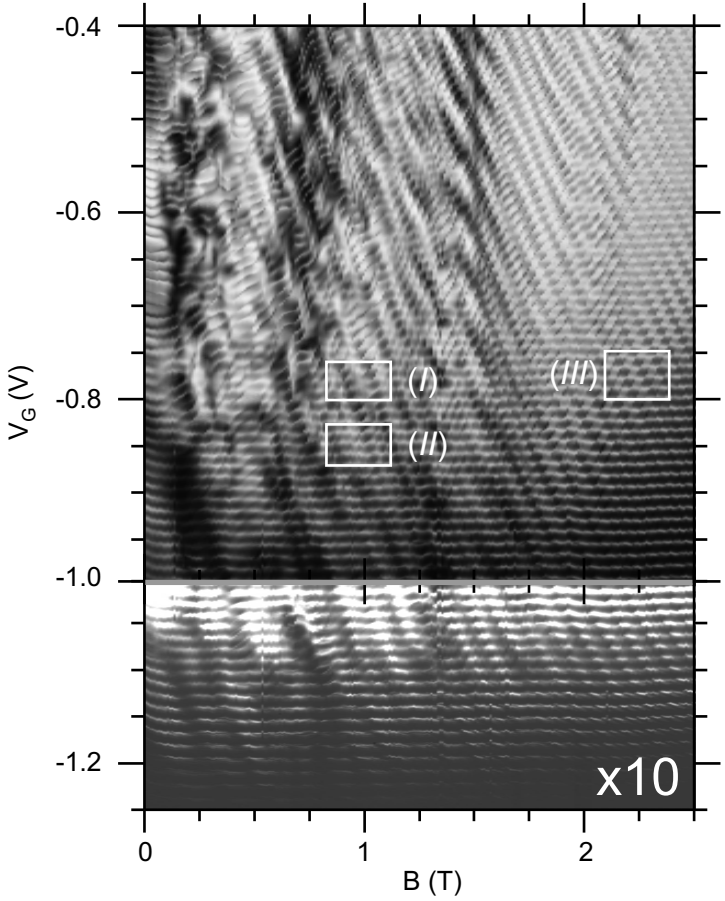


Figure 5.9: Grey scale plot of the linear conductance G as a function of plunger gate voltage and perpendicular magnetic field, black corresponds to zero conductance and white to $G = 1.8 e^2/h$ ($G = 0.18 e^2/h$ for $V_G < -1$ V). A striking, regular diagonal stripe pattern is visible especially for magnetic fields $B > 1$ T. Regions (I)-(III) marked by white rectangles will be further investigated in Figures 5.11 and 5.12.

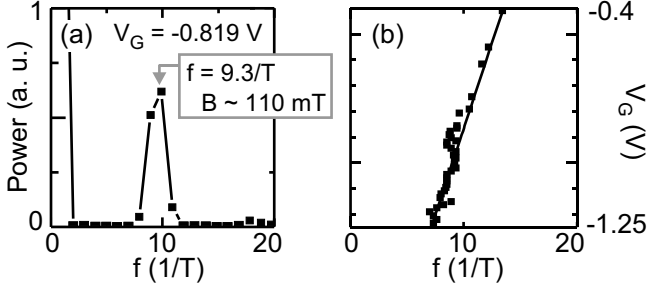


Figure 5.10: Analysis of the V_G dependent periodicity of the stripe pattern in Figure 5.9 between 1.5 T and 2.5 T, where the pattern is most clearly visible: (a) Fourier transform of one line in Figure 5.9 ($V_G = -0.819$ V) along the B axis, showing a distinct peak corresponding to a periodicity of $\Delta B \approx 110$ mT. (b) Evaluations like in (a) show a roughly linear variation of the peak position with gate voltage V_G .

dot diameters

$$d = 2\sqrt{N_\phi\phi_0/\pi\Delta B}$$

ranging from 200 nm ($V_G = -1.2$ V) to 265 nm ($V_G = -0.4$ V) which is in good agreement with the value of $d_{el} \approx 250$ nm estimated from the gate geometry. The smaller diameter for a more negative plunger gate voltage is expected due to an increased depletion region near the gates. From the calculated diameters and the 2DES electron density $n_e = 3.72 \cdot 10^{-15} \text{ m}^{-2}$ (appendix C) we expect a change in the number of electrons on the dot of $\Delta N = 87$ electrons which closely resembles $\Delta N = 75$ electrons as known from Coulomb blockade. The small difference could easily be attributed to the uncertainty in the charge density n and its unknown exact form in the presence of charged top gates.

The addition of a flux quantum to a many electron system will change its orbital and spin wave functions for magnetic fields smaller than the extreme quantum limit. As already discussed in chapters 2.2 and 4.4.2, electrons are redistributed between different Landau levels when a flux quantum is added. Thus we can link our stripe period to such redistributions of electrons. This interpretation is supported by

measurements of Coulomb-peak position and amplitude versus B in chapter 5.5.

5.4.2 Modulated Kondo effect at low magnetic fields

To clarify the origin of the stripe pattern, we will now focus on more detailed measurements in the fairly regular $B \sim 1$ T regime as marked in Figure 5.9 by (I). The filling factor in the dot at these magnetic fields is extrapolated to $\nu_{dot} \sim 8$ using the results from chapter 4.4.3. However, it is not clear whether it is still correct to assume Landau quantization in the dot at such low magnetic fields.

The stripe pattern is made up of regions of enhanced conductance in the Coulomb *blockade* regions (Figure 5.11(a)), which together with the Coulomb peaks form tiles of increased conductance.

We have performed temperature and source-drain voltage dependent measurements at the marked gate voltage and magnetic field values to analyze this effect (Figure 5.11(c)). In the high conductance regions, a zero-bias peak is observed (circle in the figure). It vanishes with increasing temperature and disappears at a temperature of $T \approx 1$ K. This zero-bias peak is a clear signature of an interaction effect. It can be attributed to the Kondo effect which is illustrated by the characteristic temperature dependence in Figure 5.11(d). Due to the high and increasing background conductance it is difficult to determine an exact Kondo temperature T_K . After subtracting the exponential background known from the low conductance regions (triangle), the temperature dependence can be fit by the empirical formula from equation 5.7. We extract a Kondo temperature $T_K \approx 0.4$ K and $s \approx 1.1 \pm 0.2$. Although the value of s strongly depends on the other fit parameters, in contrast to the analysis from chapter 5.3.2 it clearly deviates from $s = 0.2$ characteristic for a spin 1/2 system in the Kondo regime.

For the low conductance regions, the central Kondo peak is suppressed (Figure 5.11(c)). Here the two small side peaks at ± 170 μeV which are also visible in the high conductance trace become more prominent. We expect them to be related to a Kondo effect involving inelastic cotunnelling through excited states as discussed in chapter 5.1.4 on page 73. This would be roughly consistent with the level spacing $\Delta\varepsilon \approx 100$ μeV stated above and also explains the background con-

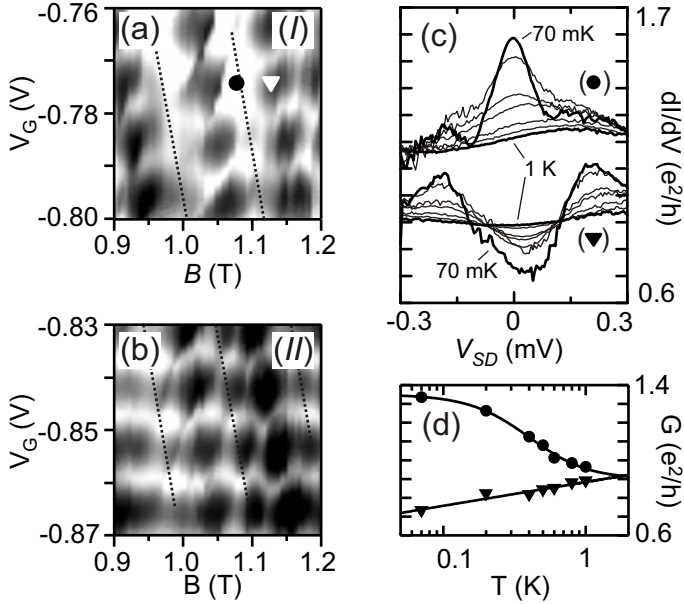


Figure 5.11: (a) and (b) A more detailed view into the regions (I) and (II) marked in Figure 5.9 with the extrapolated stripe positions highlighted by dotted lines (black corresponds to $G = 0.4 e^2/h$ and white to $1.2 e^2/h$). (c) Differential conductance versus V_{SD} in high (●) and low (▼) conductance regions marked in (a) for temperatures $T = 70, 200, 400, 500, 600, 800$ and 1000 mK. (d) Temperature dependence of linear conductance ($V_{SD} = 0$ V) at the positions marked in (a) and corresponding fits.

ductance increasing exponentially with temperature in Figure 5.11(d) (triangle).

In linear conductance ($V_{SD} = 0$ V), the central Kondo peak appears as a high conductance tile and the absence of a Kondo peak as a low conductance tile. Stripe and tile patterns can thus be explained with a magnetically modulated Kondo effect.

In the $B \sim 1$ T regime, in some areas the situation is not as clear cut and deviations from the regular magneto-conductance pattern are found. In Figure 5.11(b) corresponding to region (II) in Figure 5.9, we observe a more honeycomb-like structure made up of narrow high-conductance lines between two adjacent Coulomb blockade peaks instead of a high-conductance tile. This less regular magneto-conductance is attributed to the high dot filling factor at $\nu_{dot} \sim 8$ at these magnetic fields.

5.4.3 Modulated Kondo effect at high magnetic fields

Compared to the low magnetic field regime at $B \sim 1$ T, for a higher magnetic field, e. g. at $B \sim 2.2$ T, the stripe pattern is much clearer and extremely regular. This is seen in Figure 5.12(a) corresponding to region (III) from Figure 5.9. Different from the low field regime, the high field regime is characterized by a periodic magneto-conductance extending over a wide range of gate voltage and magnetic field. Like in region (I) discussed above, it consists of alternating tiles of enhanced and suppressed conductance within the Coulomb blockade regions. The filling factor of the dot in this regime is $3 < \nu_{dot} < 4$ (chapter 4.4.3).

To investigate the nature of the Kondo physics found here, we examine the involved energy scales in V_{SD} dependent differential conductance measurements in Figure 5.12(b) and (c). In tiles of enhanced conductance, a clear zero-bias Kondo anomaly is observed. This Kondo peak is the reason for the conductance enhancement in high-conductance tiles. In contrast, in tiles of suppressed conductance a split Kondo peak is found. In Figure 5.13 we verify that this observation holds over complete tiles instead of being valid only for single magnetic fields. Non-linear conductance is plotted at a fixed gate voltage as a function of B and V_{SD} . The central and split Kondo peaks are clearly visible, but we don't observe any smooth variation of the splitting within the

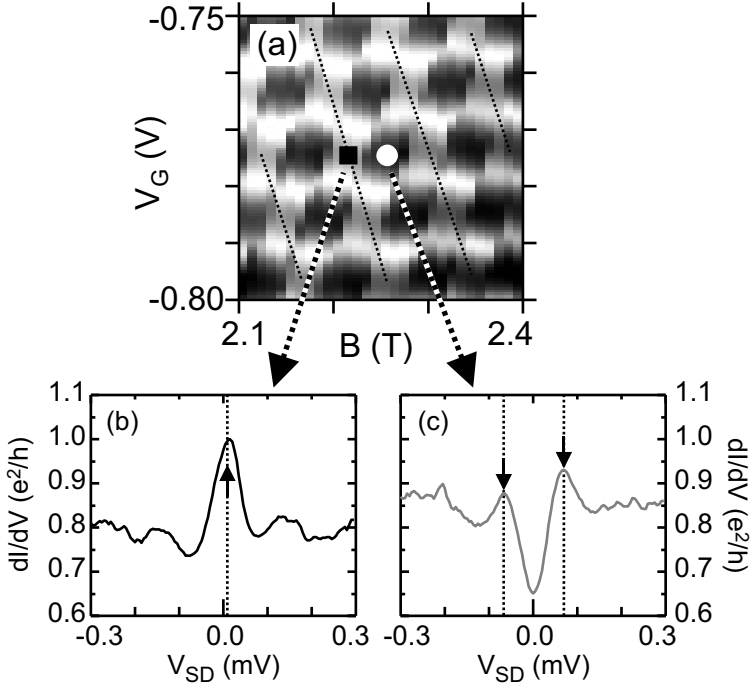


Figure 5.12: Analysis of region (III) from Figure 5.9, $B \approx 2.2$ T: (a) Over a wide parameter range the stripe pattern is formed by tiles of increased conductance between Coulomb blockade peaks. The black dotted lines illustrate the stripes. (b) and (c) Nonlinear conductance measurements at the positions marked in (a) show Kondo conductance anomalies marked by arrows.

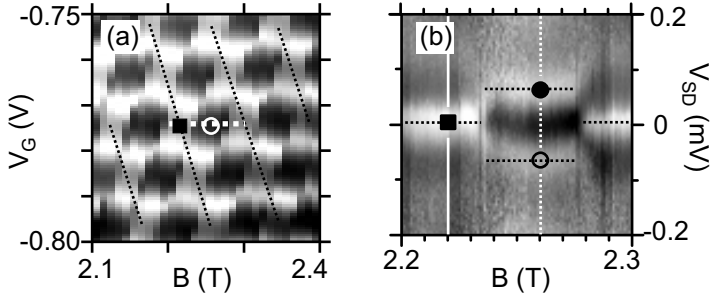


Figure 5.13: (a) Chessboard pattern from the previous figure. (b) Nonlinear magneto-conductance along the white dotted line in (a) in the Coulomb blockade valley at a fixed $V_G = -0.775$ V. Conductance maxima are highlighted with horizontal dotted lines. The positions of the cuts in Figure 5.12(b) and (c) are marked.

high- or low-conductance tiles. The transition between both situations is abrupt. The chessboard pattern is explained with this modulation of a Kondo effect as a function of magnetic field. More data on the transition between high- and low-conductance tiles is found in appendix D.2.

A closer look at Figure 5.12 reveals that the central Kondo peak is accompanied by additional side peaks at $V_{SD} = \pm 140 \mu\text{V}$ in high conductance tiles. These are marked in Figure 5.14(c). In low conductance tiles, not only the split Kondo peaks at $V_{SD} = \pm 70 \mu\text{V}$ but also a side peak at $V_{SD} = -210 \mu\text{V}$ is visible (Figure 5.14(f)). A side peak at $V_{SD} = 210 \mu\text{V}$ is not clearly observed. The spacing of the peaks is $\Delta V_{SD} = 140 \mu\text{V}$ in both situations.

We attribute the structure of Kondo peaks in high- and low-conductance tiles to a Kondo effect involving excited states and inelastic cotunnelling as introduced in chapter 5.1.4 on page 73. The following discussion first focuses on the high-conductance tiles.

The situation in high-conductance tiles is illustrated in Figure 5.14(a)-(c). The central Kondo peak in (c) must be due to a Kondo effect involving a degenerate level as illustrated in (a). The level splitting must be $\Delta\varepsilon = 0$ because no Kondo peak splitting is observed. This

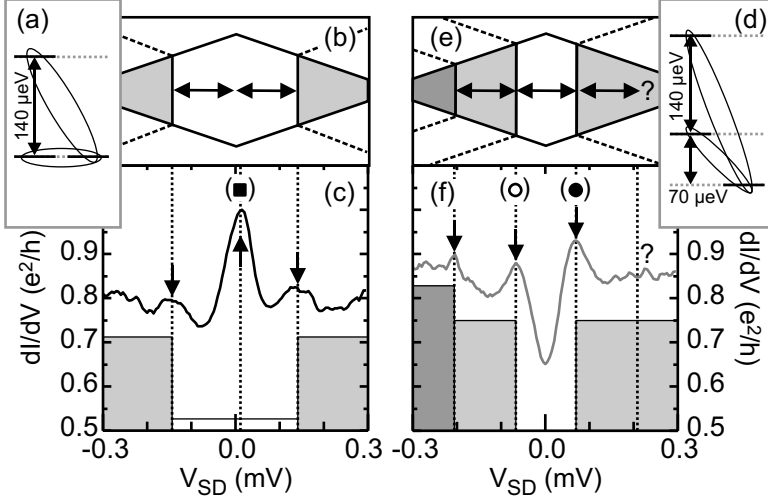


Figure 5.14: Composition of the nonlinear conductance in (a)-(c) high-conductance tiles corresponding to Figure 5.12(b) and in (d)-(f) low-conductance tiles corresponding to Figure 5.12(c). In (c) and (f) we have illustrated a background conductance due to inelastic cotunnelling as grey rectangles. Superimposed Kondo peaks are marked by arrows. In (b) and (e) sketches of corresponding Coulomb diamonds are shown for comparison with Figure 2.11 on page 26. (a) and (d): Energy levels involved in the Kondo effects (ellipses).

is despite the magnetic field from which a Zeeman splitting of $E_Z = g_{GaAs}\mu_B B = 55 \mu\text{eV}$ would be expected for a spin-1/2 system. We would clearly be able to observe such a Zeeman splitting in this measurement due to the low ratio $k_B T_K / E_Z = 0.3 < 1$. As no splitting is observed, either a many-electron state with total spin $S = 0$ (and consequently $E_Z = 0$) is responsible for this Kondo peak or Zeeman energy and other energies cancel, e. g. due to orbital effects. These scenarios cannot be distinguished because the Zeeman energy varies too slowly with magnetic field, thus the Zeeman contribution to the energy levels cannot be varied effectively. At $V_{SD} = \pm 140 \mu\text{V}$ we observe the onset of inelastic cotunnelling through an excited state. The

grey rectangles illustrate the background conductance caused by this effect. At the onset of inelastic cotunnelling, ground state and excited state with $\Delta\varepsilon = 140 \mu\text{eV}$ contribute to Kondo peaks superimposed on the inelastic cotunnelling conductance. As decoherence is introduced due to the finite source-drain voltage V_{SD} [82, 107], the amplitude of the excited Kondo peaks is considerably suppressed. The Coulomb diamond depicted in (b) relates this situation to the one discussed in Figure 2.11 on page 26.

An excitation spectrum consistent with the three Kondo peaks is shown in (a). The energy difference between pairs of levels exhibiting a Kondo effect is given by the nonlinear conductance data. Not every pair of levels exhibits a Kondo effect – for example, there could be no spin difference between the two states. Hence, it should be noted that not necessarily every level is included in such a spectrum but only a subset of the available levels.

For the low-conductance tiles, the analysis is much the same as for the high-conductance tiles. It is shown in Figure 5.14(d)-(f). Here, at zero source-drain voltage no degenerate level is present to show a Kondo effect. However, the ground state together with excited states at $\Delta\varepsilon = 70 \mu\text{eV}$ and $210 \mu\text{eV}$ does show Kondo effects, also involving inelastic cotunnelling. This feature is suppressed at $V_{SD} = +210 \mu\text{V}$, likely due to an asymmetry in the tunnel barriers. The lack of a side peak at positive bias voltage was already observed in the measurements presented in section 5.3.1.

We want to point out that the low conductance situation is explained solely by split Kondo peaks and not by a two-stage Kondo effect [94, 92, 93]. A two-stage Kondo effect consists of two Kondo peaks of different widths superimposed at $V_{SD} = 0$ with different phases, also leading to a double peak structure. Therefore the peak width of the second Kondo peak must be very high which would require an extremely high Kondo temperature in the case considered here. This effect would also be unable to explain the side peaks at $V_{SD} = -140 \mu\text{eV}$ and $V_{SD} = -210 \mu\text{eV}$.

To verify that the peak structure is indeed related to Kondo physics, the Kondo conductance is shown in Figure 5.15 as a function of temperature. The central Kondo peak in the high conductance situation shows the expected decrease with increasing temperature. We extract

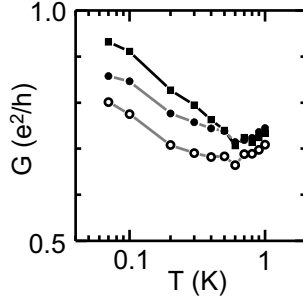


Figure 5.15: Temperature dependent linear ($V_{SD} = 0$ V) conductance of a zero-bias Kondo peak (squares) and finite bias Kondo peaks (circles/discs) at $V_{SD} = \pm 70 \mu\text{V}$ as marked in Figure 5.13(b).

a Kondo temperature of roughly $T_K \approx 0.2$ K. The increase in conductance for $T > 0.5$ K is attributed to the thermally activated inelastic cotunnelling contribution. For the split peaks, we measure the peak conductance as a function of temperature at finite source-drain voltage. It shows basically the same Kondo temperature dependence as the single peak. Although no exact calculations exist for such a situation, this is generally expected [108]. The temperature dependence of further side peaks was not investigated because of their extremely low amplitude and the unknown influence of high source-drain voltages. The Kondo chessboard conductance pattern completely vanishes with increasing temperature as shown in Figure 5.16, i. e. at temperatures above $T \approx 0.5$ K only regular Coulomb blockade resonances are observed.

Our results are different from the chessboard-like magneto-conductance pattern investigated previously by Keller *et al.* [103] who observed an alternation between Zeeman split spin-1/2 Kondo peaks in their high conductance regions and no Kondo effect at all. Both experiments were conducted in the same dot filling factor regime $2 < \nu_{dot} < 4$. We attribute this discrepancy to a steeper confinement potential in their reactive ion etched dot and to a lower Kondo temperature and coupling in comparison to our system. Theoretical investigations [101, 102, 109] explain the large scale chessboard conductance pattern but cannot make

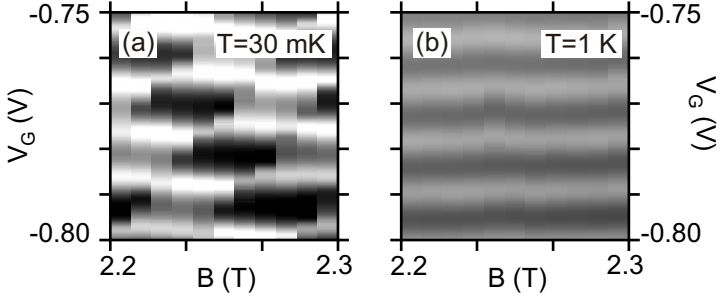


Figure 5.16: Chessboard Kondo conductance from Figure 5.13(a), at (a) base temperature $T = 30$ mK and (b) at $T = 1$ K. At high temperatures the tile pattern completely vanishes.

predictions on nonlinear conductance measurements. Further theoretical work is needed to fully understand the splitting at finite source-drain voltage. The source-drain dependent measurements presented here could be a starting point for a better understanding of the spectra of multi-electron quantum dots and their evolution in a magnetic field as they contain information on the energy spectrum.

5.5 Coulomb-peak positions and amplitudes in the Kondo regime

The analysis of Coulomb-peak positions and amplitudes in magneto-transport measurements was already introduced in chapter 4.4.2 as a spectroscopic tool to understand the effect of a magnetic field on the electronic ground state of quantum dots. In the present chapter, this technique is applied to a quantum dot in the Kondo regime. As in chapter 4.4.2, two regimes, namely absence and presence of spin blockade, are distinguished. Indications for a suppression of the Kondo effect due to a spin polarization of the emitter are found.

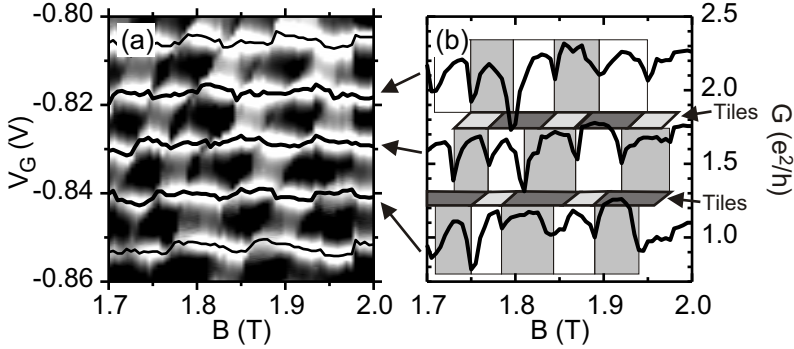


Figure 5.17: (a) Grey scale plot of the chessboard-like linear conductance G as a function of magnetic field B and plunger gate voltage V_G (black: $G = 0.4 e^2/h$, white: $G = 1 e^2/h$). Coulomb-peak positions are marked by the black lines. (b) Coulomb-peak amplitudes from (a) (curves are offset for clarity). Between the curves, tiles from the chessboard pattern are shown. The curve segments are highlighted as described in the text.

5.5.1 Absence of spin blockade

The Coulomb-peak positions in plunger gate voltage V_G are expected to exhibit a zig-zag pattern in an increasing magnetic field B . They reflect the energy of the dot state involved in the tunnelling process. Although we observe such a pattern in the Coulomb-blockade regime at weak dot-lead coupling (chapter 4.4.2, in particular Figure 4.11), in the higher coupling regime investigated here such a pattern is not clearly visible. Figure 5.17(a) shows that the Coulomb-peak positions in the Kondo regime are dominated by a shift towards Kondo valleys obscuring the zig-zag pattern. This shift of the peak position in the Kondo regime is not unexpected and was already observed in the first studies by Goldhaber-Gordon *et al.* [89].

However, the amplitude modulation of the Coulomb peaks still closely resembles the results known from measurements in the traditional regime of weak coupling. This is shown in Figure 5.17(b) for three consecutive Coulomb peaks from Figure 5.17(a). Corresponding curve

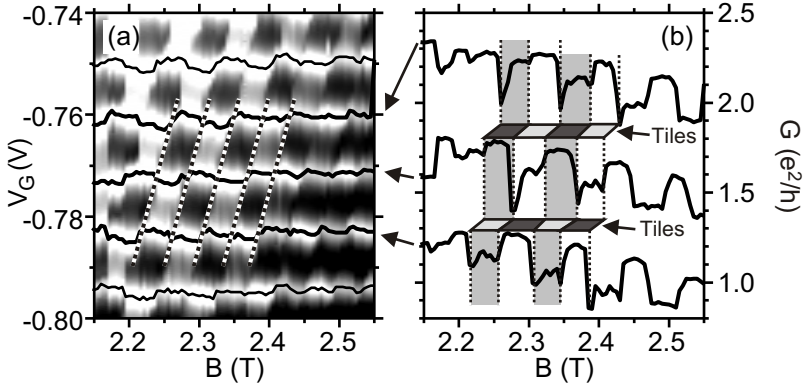


Figure 5.18: Equivalent of Figure 5.17 for a slightly different magnetic field B and plunger gate voltage V_G . (a) Grey scale plot of the linear conductance G (black: $G = 0.5 e^2/h$, white: $G = 1 e^2/h$) with Coulomb-peak positions. (b) Coulomb-peak amplitudes from (a) (curves are offset for clarity) with corresponding curve segments highlighted. The alternating high and low conductance maxima are a signature of spin blockade. The tiles from the chessboard pattern are sketched between the curves.

segments are highlighted by a white (light grey) background with high-(low-) conductance tiles from the Coulomb valleys in between. At the downward cusps, the electrons are redistributed between two Landau levels. Thus the ability of the system to show a zero-bias Kondo effect reflected in the tile pattern is switched. The coincidence between the switching of the Kondo effect and cusps in the Coulomb-peak amplitude is nicely reflected in the measurement.

5.5.2 Spin blockade and vanishing Kondo effect

In Figure 5.18 an analysis similar to the previous one is shown for slightly different magnetic fields and plunger gate voltages. In the range from $B = 2.15$ T to $B = 2.55$ T shown here we clearly observe the onset of spin blockade. The amplitude modulation found in Figure 5.18(b) for high magnetic fields $B \gtrsim 2.4$ T closely resembles the modulation found

for spin blockade in the Coulomb regime. For lower fields $B \lesssim 2.2$ T no spin blockade is found and the amplitude modulation is comparable to the one discussed in the previous section. The magnetic field values for the onset of spin blockade agree in Kondo and Coulomb regimes at least for some peaks, e. g. for the peak shown in Figure 4.11. Thus the outer edge state in the leads which is most important for transport becomes spin polarized just in the transition regime shown in the figure.

We remind that both, the alternating medium-conductance and high-conductance plateaus in the spin blockade regime, are attributed to transport due to electrons tunnelling through outer edge states. The difference in their amplitudes is due to the modulation of spin blockade. The Coulomb-peak amplitude is suppressed when the spins of the spin-polarized emitter and the transport state on the dot don't match and unsuppressed if they do match. The cusps between the plateaus are attributed to transport due to electrons utilizing inner Landau levels. In comparison, in absence of spin blockade only high-conductance plateaus are present. Hence the observation of spin blockade indicates a spin polarization of the emitter. The effective spin polarization of a 2DES emitter due to the formation of spin-polarized edge states coupling to the quantum dot with different strengths was discussed in chapter 4.4.2 of page 54.

Simultaneously with the onset of spin blockade we observe a suppression of the high-conductance tiles in the chessboard pattern. This in turn is attributed to a suppression the zero-bias Kondo effect because this Kondo effect is responsible for the increase of conductance in high-conductance tiles. Approximately at $B = 2.5$ T when full spin blockade has been reached the Kondo effect has completely vanished. Figure 5.19 shows the relevant data over a wider range of magnetic field. The onset of spin blockade is clearly observed in the Coulomb peak positions in Figure 5.19(b). Simultaneously the high-conductance tiles in the chessboard-like magneto conductance are suppressed. This is also reflected in Figure 5.19(c) which shows how the modulated Kondo effect in the Coulomb valley vanishes. At still higher magnetic fields spin blockade vanishes and the Kondo effect is restored.

Although the zero-bias Kondo effect might be destroyed by a lifted degeneracy of two levels due to the magnetic field, the coincidence with the observation of spin blockade suggests another explanation:

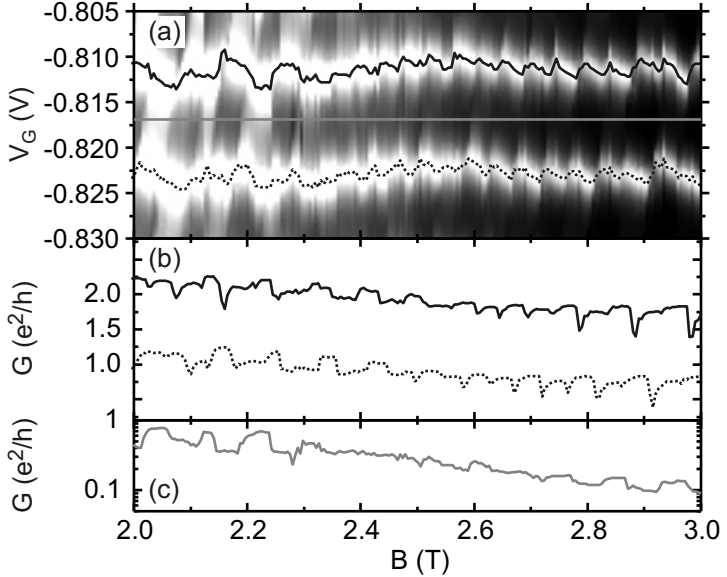


Figure 5.19: (a) Linear conductance G versus plunger gate voltage V_G and magnetic field B . Coulomb-peak positions are highlighted. The grey line in the middle of the Coulomb valley marks the cut used for (c). (b) Coulomb-peak amplitudes from (a), curves are offset for clarity. (c) Logarithmic Kondo conductance in the Coulomb valley as marked in (a).

The Kondo effect is a spin scattering process. A prerequisite for a Kondo effect is that both spin orientations must be present in the emitter. Thus if only one spin orientation from the emitter couples to the quantum dot, the dot spin cannot be screened and the Kondo effect vanishes.

We illustrate this situation in Figure 5.20 in more detail. In chapter 5.1.2 we have understood that a Kondo effect is a singlet state between dot and lead electrons. Since such a singlet is a superposition of both spin orientations, $|\uparrow\rangle$ and $|\downarrow\rangle$, on both sites, in the emitter and on the dot, it in particular requires the presence of both, $|\uparrow\rangle$ and $|\downarrow\rangle$ electrons,

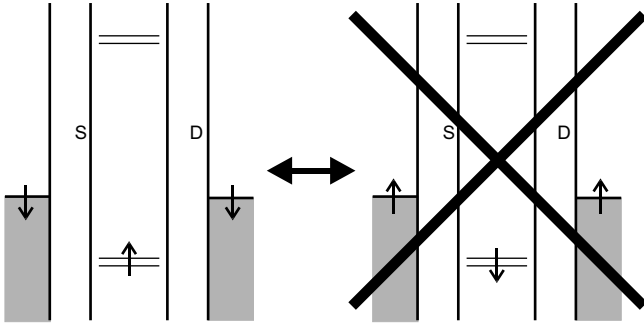


Figure 5.20: Spin polarization in the emitter suppresses the formation of a Kondo singlet which is a superposition of both states depicted. The cancelled state would require emitter electrons of the spin orientation which is not present.

in the emitter. Obviously in a spin polarized emitter only one spin orientation is present. Thus no Kondo singlet can be formed, the Kondo effect is suppressed. The measurements demonstrate this dependence of the Kondo effect on the presence of both spin orientations in the emitter for the first time.

5.6 Conclusions

Based on the results from the Coulomb-blockade regime discussed in chapter 4 we have explored Kondo physics in a large quantum dot with strong coupling to the leads. The high number of interacting electrons on the dot gives rise to a rich structure of the Kondo physics.

At zero magnetic field, we have observed a zero-bias Kondo effect in subsequent Coulomb-blockade valleys showing that exchange interaction is large enough in our multi-electron dot for Hund's rule to be applicable. We have verified the typical temperature dependence of the zero-bias anomaly as a further fingerprint for Kondo physics. Indications for a finite-bias Kondo effect involving inelastic cotunnelling through excited states were also observed.

Tuning the quantum dot in a magnetic field revealed a flux quan-

tum modulation of the Kondo effect over a wide parameter range in magnetic field and in the number of electrons. While we do observe deviations at high dot filling factors, for $3 < \nu_{dot} < 4$ the modulation results in a strikingly regular chessboard pattern in the magneto conductance. Nonlinear conductance measurements in this regime reveal that Kondo physics is present everywhere in the chessboard pattern, in high- as well as in low-conductance tiles. We find that not the presence of a Kondo effect but its peak splitting in V_{SD} is modulated by the magnetic field. The magnitude of the splitting allows conclusions on the spectrum of the quantum dot and might be used as a spectroscopic tool in other experiments. The splitting of the Kondo peaks changes nearly abruptly between high- and low-conductance tiles indicating a sharp transition between different ground states. This Kondo effect needs an explanation which goes beyond the classical spin-1/2 Anderson model and must be more complicated than a simple hybridization between leads and one single electron on the dot. Correlated many-electron effects on the dot must play a role.

By combining an analysis of Coulomb-peak amplitudes to detect a spin polarization of the outer emitter edge states with the observation of the modulated Kondo effect we have demonstrated the dependence of the spin Kondo effect on the presence of both spin polarizations in the leads.

6 Fano regime

In this thesis, first the properties of a quantum dot in the Coulomb blockade regime, i. e. at weak coupling to the leads, have been analyzed (chapter 4). In the gate-voltage dependence of the transmission of the dot, we observed narrow, symmetric Coulomb resonances with nearly zero conductance in between. At increased coupling, the Kondo effect leads to an increased transmission *between* these Coulomb resonances at zero bias voltage (chapter 5). The present chapter is devoted to a regime characterized by a still larger coupling of the dot to the leads, where we observe symmetric and asymmetric Fano resonances and anti-resonances instead of Coulomb peaks. Our dot can be tuned continuously between all three regimes, Coulomb blockade, Kondo and Fano. This allows to study Fano resonances in a system well characterized in the other regimes.

After introducing Fano resonance we develop a two-channel model to explain and parameterize the emergence of Fano resonances in SETs. We analyze the experimentally observed Fano lineshapes as a function of bias voltage V_{SD} , temperature T , and magnetic field B and extract information on decoherence and on the second conductance channel in the Fano system. Finally we discuss the origin of this channel.

6.1 Introduction to Fano resonances

The theory of Fano resonances was originally developed in the context of electron-atom scattering [19] but by now is ubiquitous in resonant scattering theory. Fano resonances have been observed in a wide variety of experiments like atomic photoionization [110], electron-neutron scattering [111], Raman scattering [112], photoabsorption in quantum

well structures [113, 114] or scanning tunnelling microscopy [115]. Since transport in mesoscopic systems can be described in a framework similar to the above systems [116, 117], Fano resonances have been predicted also for semiconductor nanostructures (Reference [118] and references in Reference [20]).

Fano resonances are observed whenever a resonant scattering channel interferes with a non-resonant contribution as illustrated in Figure 6.1(a). In electronic transport experiments this occurs if the quantum mechanical wave function of incident electrons is split into two parts (one for each channel) at the entrance of some structure. Both parts interfere at the exit of the structure. Hence the scattered wave function is the result of interference of an incident electronic wave function transmitted through both channels. This is similar to Aharonov-Bohm or double-slit experiments. Special about Fano experiments is the phase shift in the resonant channel which depends on the energy of the incident electrons. It varies between $-\pi/2$ and $\pi/2$. In contrast, the non-resonant channel's phase shift is energy independent. Thus the total transmission amplitude resulting from the interference of both channels is a function of the energy of the incident electrons. Although Fano transmission lineshapes include the Breit-Wigner shape well-known from single channel resonant scattering theory, their general shape is more generic as can be seen from Figure 6.1(b). Fano lineshapes will be explained in more detail below.

We consider Fano systems in semiconductor nanostructures containing a SET in the resonant channel. In such systems, Fano resonances reflect the phase shift due to the SET when crossing its resonances. We distinguish three types of structures:

1. The obvious implementation of a Fano system is an Aharonov-Bohm interferometer [119] with a SET embedded in one arm of the ring structure [120]. Similar experiments are conducted in ballistic two-path double-slit interferometers with the SET embedded in one path [121, 122]. The path or ring arm containing the SET is mapped to the resonant channel in a Fano system, and the other arm is related to the non-resonant channel. The phase shift of the non-resonant channel is controlled by application of a magnetic field perpendicular to the interferometer which permits

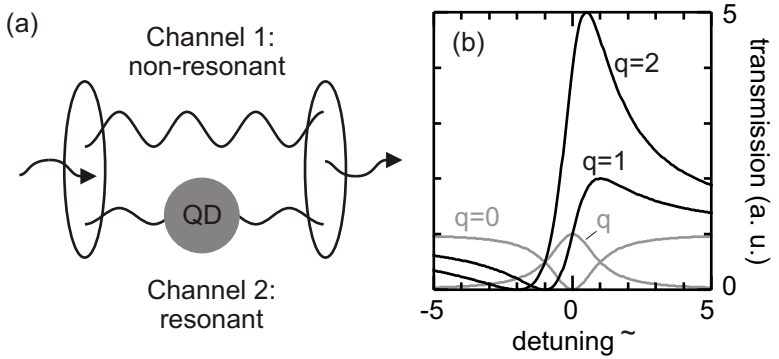


Figure 6.1: The two-channel scattering process schematically depicted in (a) generally leads to Fano resonances with their wide variety of lineshapes, some of them shown in (b). Depending on phase φ and transmission t of the two channels, different values of the Fano parameter q lead to symmetric Breit-Wigner (anti-) resonances or completely asymmetric transmission lineshapes as functions of the detuning from the resonance, $\tilde{\epsilon}$. For negative values of q the resonances are mirrored at the ordinate, i. e. $\tilde{\epsilon} \rightarrow -\tilde{\epsilon}$.

to measure the phase shift in the SET [122]. Due to the high complexity of these experiments the results sometimes are not very clear cut [123, 124].

2. Fano resonances are also observed in ordinary SETs [20, 21] in the regime of very strong coupling to the leads, the system studied in this work. Like for the structures discussed above, the Coulomb resonances of the SET explain a resonant transmission channel through the system. The origin of the second, non-resonant transmission channel is not obvious. We will discuss its nature extensively in section 6.3.
3. Small quantum rings [125, 126] are the third type of structures exhibiting Fano resonances [57]. They combine properties of Aharonov-Bohm rings and quantum dots. In these structures, resonant and non-resonant channels cannot easily be distinguished.

6.1.1 General properties of Fano resonances

Fano considered a scattering problem with unperturbed continuum states $|\psi\rangle$, discrete states $|\varphi\rangle$ and states of the whole system $|\Psi\rangle$ [19]. With an operator \mathbf{T} describing the transition between an initial state $|i\rangle$ and the state $|\Psi\rangle$ he found that the ratio of the transition probability $|\langle\Psi|\mathbf{T}|i\rangle|^2$ to the probability $|\langle\psi|\mathbf{T}|i\rangle|^2$ of transition to the unperturbed continuum can be described by a single family of curves:

$$f_{Fano}(\tilde{\varepsilon}) = \frac{|\langle\Psi|\mathbf{T}|i\rangle|^2}{|\langle\psi|\mathbf{T}|i\rangle|^2} = \frac{(\tilde{\varepsilon} + q)^2}{\tilde{\varepsilon}^2 + 1}. \quad (6.1)$$

These curves are functions of a normalized detuning $\tilde{\varepsilon}$ which is calculated from the resonance energy ε_0 and the resonance width $\hbar\Gamma$,

$$\tilde{\varepsilon} = (\varepsilon - \varepsilon_0)/(\hbar\Gamma/2). \quad (6.2)$$

The so-called asymmetry parameter q is crucial for the actual shape of a Fano resonance. We consider states $|\Phi\rangle$ which are the discrete states $|\varphi\rangle$ modified by the admixture of the continuum. q is then calculated from the ratio of the transition probabilities to the modified discrete states $|\Phi\rangle$ and to a band of width Γ of unperturbed continuum states $|\psi\rangle$ [19]:

$$\frac{1}{2}\pi q^2 = \frac{|\langle\Phi|T|i\rangle|^2}{|\langle\psi|T|i\rangle|^2\Gamma}. \quad (6.3)$$

Figure 6.1(b) illustrates typical Fano lineshapes for various values of q : For large q , $q \rightarrow \infty$, we get the symmetric Breit-Wigner lineshape [40] (a prefactor $\sim 1/q^2$ has to be introduced for normalization to avoid divergence as $q \rightarrow \infty$, but leaving the shape of the resonance unaffected),

$$f_{BW}(\tilde{\varepsilon}) = \frac{1}{\tilde{\varepsilon}^2 + 1}. \quad (6.4)$$

This lineshape was already found in the low temperature limes of SETs in the Coulomb regime (equation 2.21 on page 29). With decreasing q we get asymmetric lineshapes with a maximum for positive detuning $\tilde{\varepsilon}$, while for negative detuning a minimum with vanishing transmission is observed at $\tilde{\varepsilon} = -q$. At vanishing $q = 0$ the lineshape becomes

symmetric again and anti-resonances with a minimum at $\tilde{\varepsilon} = 0$ are observed. These dips have a Breit-Wigner lineshape, $f_{Fano}(\tilde{\varepsilon}) = 1 - f_{BW}(\tilde{\varepsilon})$. Negative asymmetry parameters q lead to Fano lineshapes mirrored at the ordinate, i. e. $\tilde{\varepsilon} \rightarrow -\tilde{\varepsilon}$.

6.1.2 Fano resonances in a realistic SET experiment

In a real SET experiment, there might be a background conductance in addition to Fano resonances. This part does not contribute to the interference of the two channels. Reasons for such a contribution include thermally activated transport, cotunnelling, decoherence or a reduced transmission amplitude in one of the two interfering channels. The last point leads to an imbalance of both channels, e. g. due to backscattering in one of the channels. The excess transmission remains unaffected from the interference and does not contribute to the Fano lineshape but to the background.

In presence of a background we cannot expect to observe the transmission to reach zero at $\tilde{\varepsilon} = -q$ as expected from the original transmission lineshape from equation 6.1. Instead it will remain finite at all energies. Hence the function

$$f_{Exp}(\tilde{\varepsilon}) = A_{Exp} \cdot f_{Fano}(\tilde{\varepsilon}) + B_{Exp} \quad (6.5)$$

resembles the lineshape expected from an experiment better than equation 6.1. It is later successfully employed in fitting the data. The parameter A_{Exp} scales the Fano function and B_{Exp} accounts for the excess background.

To get a realistic lineshape one may alternatively introduce a complex Fano parameter which implicitly accounts for the excess background. In References [120, 127] the transmission lineshape

$$f_C(\tilde{\varepsilon}) = A_C \frac{(\tilde{\varepsilon} + q_C)^2}{\tilde{\varepsilon}^2 + 1} = A_C \frac{(\tilde{\varepsilon} + \text{Re}(q_C))^2 + \text{Im}(q_C)^2}{\tilde{\varepsilon}^2 + 1} \quad (6.6)$$

with a complex Fano parameter q_C was used to fit the experimental data. The introduction of a complex Fano parameter has created some confusion and is not necessary if the excess background transmission is explicitly considered as in equation 6.5. Both equations, 6.5 and

6.6, are equivalent. Equation 6.5 more clearly describes the underlying physics.

6.1.3 Two-channel model of Fano resonances in SETs

In this section, we will develop a two-channel model to describe the emergence of Fano resonances in SETs. We first discuss the resonant channel, which in SET experiments is identified with the regular path of an electron through the quantum dot. We restrict our investigation to the Coulomb regime and neglect higher order contributions to the conductance like the Kondo effect. Considering a Coulomb resonance at zero temperature $T = 0$, according to Schuster *et al.* the complex transmission amplitude can be modelled using the Breit-Wigner formula [122]:

$$t_r(\tilde{\varepsilon}) = a_r \cdot \frac{i}{\tilde{\varepsilon} + i}. \quad (6.7)$$

a_r is the peak transmission amplitude and is considered a real quantity. The conductance of a quantum dot measured in an experiment is proportional to the transmission probability $T_r(\tilde{\varepsilon})$, which is easily determined from the complex transmission amplitude:

$$T_r(\tilde{\varepsilon}) = |t_r(\tilde{\varepsilon})|^2 = \frac{a_r^2}{\tilde{\varepsilon}^2 + 1}. \quad (6.8)$$

Equation 6.8 is equivalent to the Breit-Wigner formula describing Coulomb resonances (equations 2.21 and 6.4). The resonance phase shift $\varphi_r(\tilde{\varepsilon})$ of transmitted electrons is

$$\varphi_r(\tilde{\varepsilon}) = \arg(t_r(\tilde{\varepsilon})) = \arctan \tilde{\varepsilon}. \quad (6.9)$$

The transmission probability T_r and the transmission phase shift φ_r of a Coulomb resonance in a quantum dot are depicted in Figure 6.2(a). The phase shift φ_r varies from $-\pi/2$ before reaching the resonance ($\tilde{\varepsilon} \rightarrow -\infty$) to $\pi/2$ after crossing it ($\tilde{\varepsilon} \rightarrow \infty$). At the resonance position $\tilde{\varepsilon} = 0$ the phase shift is zero.

The non-resonant channel from Fano theory originates from a background conductance independent of the path through the dot and can

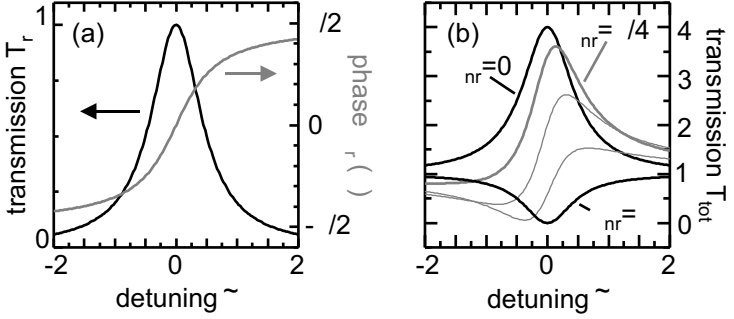


Figure 6.2: (a) Transmission probability (black) and phase shift (grey) as functions of the dimensionless detuning $\tilde{\varepsilon} = (\varepsilon - \varepsilon_0)/(\Gamma/2)$ for a quantum dot when crossing a Coulomb resonance. (b) Fano resonances in the transmission probability resulting from interference with a non-resonant background conductance with $a_{nr} = 1$ and the indicated values of φ_{nr} .

be described with the energy independent complex transmission amplitude

$$t_{nr}(\tilde{\varepsilon}) = a_{nr} \cdot e^{i\varphi_{nr}}. \quad (6.10)$$

a_{nr} is the real transmission amplitude and φ_{nr} accounts for the phase shift of the non-resonant background channel. The transmission probability of the non-resonant channel is

$$T_{nr} = |t_{nr}|^2 = a_{nr}^2. \quad (6.11)$$

To calculate the total transmission probability of an electron coherently traversing both channels including interference, we have to first sum up the transmission amplitudes and then to determine the transmission probability:

$$\begin{aligned} T_{tot}(\tilde{\varepsilon}) &= |t_r(\tilde{\varepsilon}) + t_{nr}(\tilde{\varepsilon})|^2 \\ &= \frac{a_{nr}^2(\tilde{\varepsilon}^2 + 1) + a_r^2 + 2a_{nr}a_r(\tilde{\varepsilon} \sin \varphi_{nr} + \cos \varphi_{nr})}{\tilde{\varepsilon}^2 + 1} \end{aligned} \quad (6.12)$$

Figure 6.2(b) illustrates the Fano lineshapes resulting from this coherent superposition for various phase shifts φ_{nr} of the non-resonant channel.

In presence of decoherence between the channels, the interference term in equation 6.12 vanishes. For a totally incoherent superposition, equation 6.12 is replaced by

$$T_{tot,inc}(\tilde{\varepsilon}) = |t_r(\tilde{\varepsilon})|^2 + |t_{nr}(\tilde{\varepsilon})|^2 \quad (6.13)$$

Then we get Coulomb resonances atop of the non-resonant background irrespective of the non-resonant phase φ_{nr} .

We map the parameter set $(a_r, a_{nr}, \varphi_{nr})$ in the transmission probability from equation 6.12 to the experimental fit parameters (A_{Exp}, B_{Exp}, q) from equation 6.5. After bringing both equations into the same form we identify:

$$q \left(\frac{a_{nr}}{a_r}, \varphi_{nr} \right) = \frac{1 + 2 \frac{a_{nr}}{a_r} \cos \varphi_{nr} + \sqrt{1 + 4 \frac{a_{nr}}{a_r} \cos \varphi_{nr} + 4 \left(\frac{a_{nr}}{a_r} \right)^2}}{2 \frac{a_{nr}}{a_r} \sin \varphi_{nr}} \quad (6.14)$$

$$A_{Exp}(a_r, a_{nr}, \varphi_{nr}) = \frac{a_r a_{nr} \sin \varphi_{nr}}{q(a_{nr}/a_r, \varphi_{nr})} \quad (6.15)$$

$$B_{Exp}(a_r, a_{nr}, \varphi_{nr}) = a_{nr}^2 - A_{Exp}(a_r, a_{nr}, \varphi_{nr}) \quad (6.16)$$

The equation for q is valid only for $\varphi_{nr} \neq 0, \pi, \dots$. For phase shifts φ_{nr} of zero or π we get Coulomb resonances, $q \rightarrow \infty$, and anti-resonances, $q = 0$. Note that we have neglected an incoherent contribution to the background B_{Exp} and only consider the coherent part. Although an incoherent contribution could easily be incorporated, the equations given here are sufficient to describe and interpret our data. The analytical result proves that our model of a resonant quantum dot channel interfering with a constant, non-resonant background transmission channel indeed exhibits Fano resonances.

The particularly important dependence of the experimental Fano symmetry parameter q on the non-resonant background transmission phase shift φ_{nr} is plotted in Figure 6.3 for various combinations of a_r and a_{nr} . For realistic combinations of these parameters, q does not strongly depend on a_r and a_{nr} . The variation of q as a function of

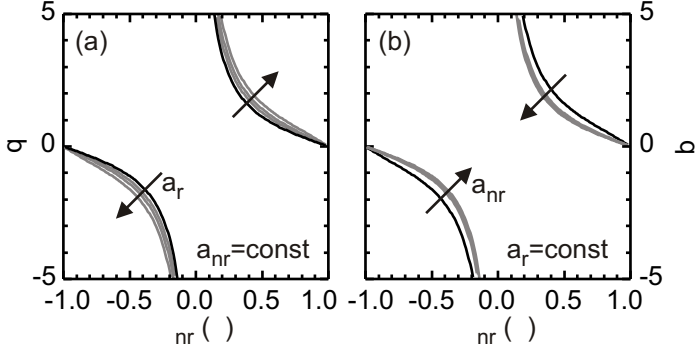


Figure 6.3: Fano symmetry parameter q as a function of the background phase shift φ_{nr} . (a) The non-resonant background transmission amplitude $a_{nr} = \sqrt{2}$ is kept constant and the resonant channel's transmission is varied from $a_r = \sqrt{0.1}$ (black line) to $\sqrt{0.5}$, 1 and $\sqrt{2}$. (b) The resonant transmission amplitude is constant, $a_r = \sqrt{0.1}$, and the non-resonant transmission amplitude varies from $a_{nr} = \sqrt{0.1}$ (black line) to $\sqrt{0.5}$, 1 and $\sqrt{2}$.

φ_{nr} can also be seen from Figures 6.1(b) and 6.2(b) which show Fano lineshapes as a function of q and φ_{nr} , respectively.

The transformation discussed so far describes how to compute the Fano parameter set (q, A_{Exp}, B_{Exp}) from the physically more descriptive parameters $(a_r, a_{nr}, \varphi_{nr})$ of our two-channel model. A reverse transformation particularly useful in analyzing experimental data is computed straight forward. The total transmission probability $T_{nr} = a_{nr}^2$ for the non-resonant background channel neglecting an incoherent contribution is

$$T_{nr} = a_{nr}^2 = A_{Exp} + B_{Exp}. \quad (6.17)$$

Because of the trigonometric functions in equations 6.14 and 6.15, a general result for a_r and φ_{nr} is complex and ambiguous. Therefore we give only the more compact set of equations

$$a_r = \frac{A_{Exp}q}{\sqrt{A_{Exp} + B_{Exp}} \sin \varphi_{nr}} \quad \text{and} \quad (6.18)$$

$$0 = (q^2 - 1) \sin^2 \varphi_{nr} - q \sin(2\varphi_{nr}) - \frac{A_{Exp} q^2}{A_{Exp} + B_{Exp}} \quad (6.19)$$

from which a_r and φ_{nr} can be determined. Later we will compute a_r and φ_{nr} for given experimental fit parameters (q, A_{Exp}, B_{Exp}) .

6.2 Measurements on a quantum dot in the Fano regime

In this section we discuss measurements on a SET in the Fano regime. We interpret Fano resonances as a function of gate voltage V_G in terms of the two-channel model developed in the previous sections. Furthermore, their dependence on source-drain bias voltage V_{SD} , temperature T , and magnetic field B is discussed.

6.2.1 Tuning the SET into the Fano regime

In chapter 5 we tuned our SET from the Coulomb-blockade regime to the Kondo regime. This was achieved by increasing the coupling between the quantum dot and the leads by application of a more positive plunger gate voltage. Although the plunger gate in a split-gate SET is intended to influence only the internal energy levels of the quantum dot, due to the extremely small spatial dimensions of such a device it also influences the tunnel barriers. Here we employ the same technique to couple the quantum dot even stronger to the leads.

Figure 6.4 shows the linear conductance of sample 1129-8-7.3 over a large range of plunger gate voltage V_G . This is the same sample already used for the experiments in chapters 4 and 5. For low temperatures of $T = 70$ mK we observe Coulomb resonances at the lowest gate voltages of $V_G \sim -1.2$ V, Kondo resonances in the intermediate regime at $V_G \sim -1.0$ V and Fano resonances at still larger gate voltages $V_G \sim -0.6$ V.

With increasing plunger gate voltage, the amplitude of the resonance peaks in Figure 6.4 generally rises apart from small variations which are caused by the different coupling of different dot ground states to the leads. In addition, a large background conductance is observed

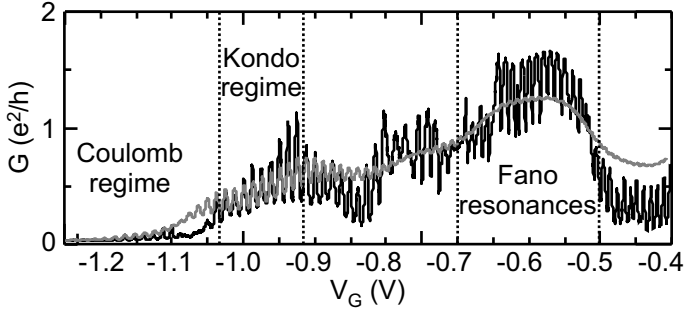


Figure 6.4: Overview of the linear conductance measurements at temperatures $T = 70$ mK (black) and $T = 1$ K (grey). Fano resonances are observed in the marked gate voltages range. They go along with an increased background conductance. The Fano regime is investigated more closely in the next figures.

which varies extremely slowly compared to the resonances. Like with the resonances, the background conductance generally increases with increasing plunger gate voltage except for the fall at $V_G \sim -0.5$ V. At high temperatures $T \sim 1$ K the features in the background conductance become more pronounced as the modulation of the superimposed Coulomb peaks decreases as indicated by the grey line in Figure 6.4. The background conductance is particularly important because Fano resonances in a SET require a non-resonant background conductance channel.

We will now turn to a detailed analysis of the Fano lineshapes between $V_G = -0.7$ V and -0.5 V.

6.2.2 Analysis of the Fano lineshapes

Detailed linear conductance measurements in the Fano regime are shown in Figure 6.5(a). Three regions marked (1) to (3) are clearly distinguished by characteristic lineshapes. In region (1), we observe asymmetric Fano resonances with $q < 0$, in region (2) symmetric anti-resonances with $q = 0$, and in region (3) asymmetric resonances with $q > 0$. Note the high background conductance of $1 - 2 e^2/h$.

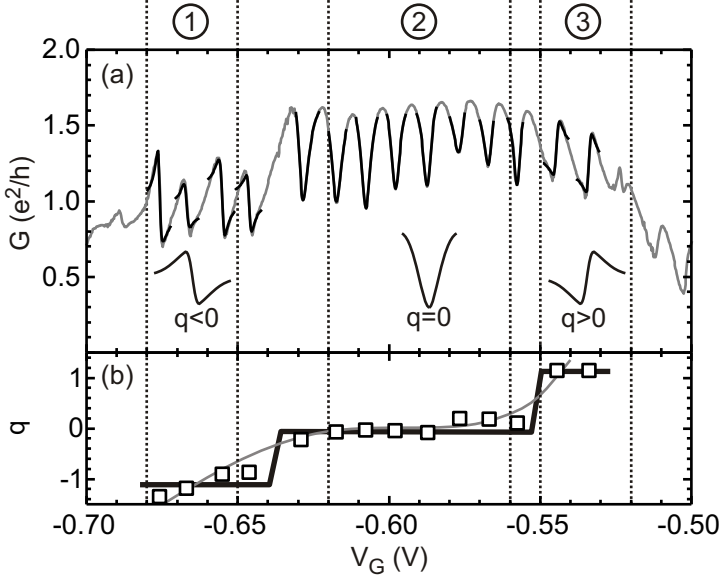


Figure 6.5: (a) Fits (black) to the Fano resonances in the linear conductance G (grey). Three regions (1)–(3) of similar lineshapes are marked, namely asymmetric Fano resonances with $q < 0$, symmetric anti-resonances with $q = 0$, and asymmetric resonances with $q > 0$. Characteristic lineshapes are sketched for the three regions. (b) Fano asymmetry parameter q determined from the above fits. The thick black and thin grey lines are guides to the eye representing two alternative interpretations of the data on q .

Fits to equation 6.5 of all measured resonances are shown by the black lines in Figure 6.5(a). Small deviations between fit and data at the edges of the region used in each fit are due to a beginning overlap with neighboring resonances. We determine the values of A_{Exp} , B_{Exp} , q , and the linewidth Γ of the resonant channel. The evolution of q as a function of plunger gate voltage is shown in Figure 6.5(b) together with two feasible interpretations of the data, namely a step-like and a smooth evolution of q . In region (2), we clearly observe $q \approx 0$, but the values of q we get from our fits in regions (1) and (3) span a wider range and critically depend on the upper and lower bounds of the fits. Roughly, all values are close to $q = +1$ or -1 , respectively. The other fit parameters are not shown as they have no direct physical meaning. Instead we determine the parameters of the two-channel model by the transformation from section 6.1.3.

Figure 6.6 shows the parameters from the two-channel model. The non-resonant conductance a_{nr}^2 clearly exhibits a step-like structure as a function of gate voltage V_G . It is $1.0 e^2/h$ in region (1), $1.7 e^2/h$ in region (2) and $1.3 e^2/h$ in region (3). Hence the non-resonant channel could be due to a one-dimensional spin-degenerate channel with a conductance of $2 e^2/h$ which is slightly reduced due to some form of scattering. Its step-like structure suggests that the step-like interpretation of the data on q from Figure 6.5(b) is more likely than the smoother one.

The resonant channel's transmission a_r^2 exhibits an unsystematic modulation. The height of the Coulomb resonances in the resonant channel strongly depends on the coupling of the involved quantum state to the leads, hence it varies from resonance to resonance which explains the modulation of a_r^2 .

The non-resonant channel's phase shift varies in a step-like fashion, much like its transmission probability a_{nr}^2 . Phase shifts of $\varphi_{nr} = 3\pi/2$, π and $\pi/2$ are observed for regimes (1), (2) and (3), respectively. However, the uncertainty in the determination of q is reflected in an uncertainty in φ_{nr} . The ambiguity in the transformation from section 6.1.3 is solved by choosing those parameters φ_{nr} from the results which reproduce the experimental lineshapes. In this way, we were able to reconstruct the parameters of the two-channel model from our experimental data.

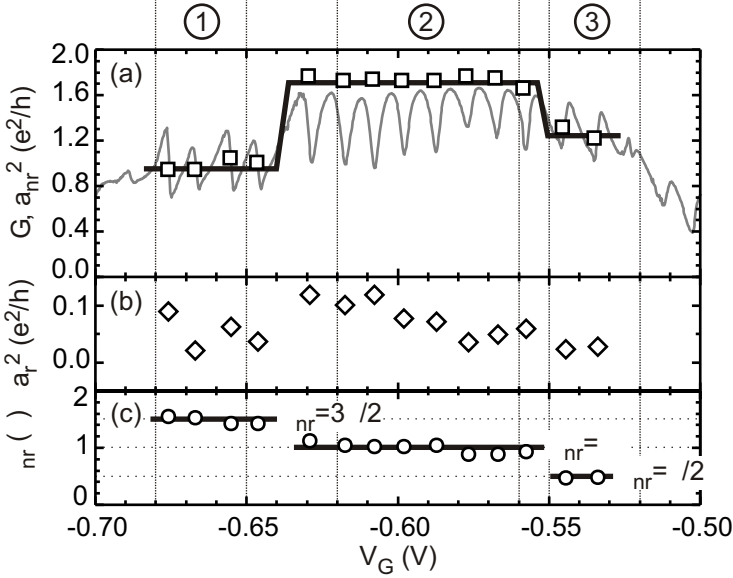


Figure 6.6: From fits to the experimental conductance we have determined (a) the non-resonant transmission probability a_{nr}^2 , (b) the resonant transmission probability a_r^2 and (c) the non-resonant channel's phase shift φ_{nr} . Regions (1)–(3) from Figure 6.5 are marked, and in (a) the experimental data is shown for comparison.

We know the Fermi wavelength $\lambda_F = 2\pi/\sqrt{2\pi n_e}$ in our sample which allows to relate a phase shift to a length. Considering $\lambda_F = 40$ nm, we identify a length of $\Delta\lambda \approx 10$ nm with the steps in the non-resonant channel's phase shift of $\Delta\varphi_{nr} = \pi/2$. Assuming that the jumps in the phase shift are due to switching between different non-resonant paths, we conclude a length difference of 10 nm between these paths. However, from our relative phase measurement we cannot determine whether there is an additional length difference of an integer multiple of λ_F .

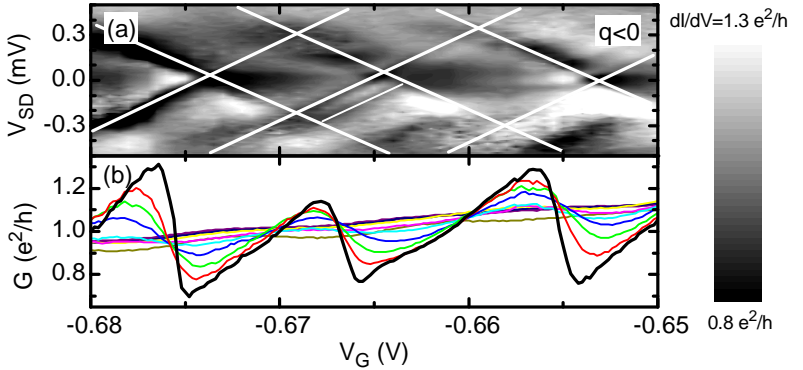


Figure 6.7: In region (1), for plunger gate voltages between $V_G = -0.68$ V and -0.65 V asymmetric Fano resonances with $q < 0$ are found: (a) Grey scale plot of the differential conductance with Coulomb diamonds highlighted by white lines. (b) Linear ($V_{SD} = 0$) conductance for temperatures $T = 0.07$ K (black), 0.2 K, 0.3 K, 0.4 K, 0.5 K, 0.6 K, 0.7 K, 0.8 K, 0.9 K (thin lines), and 1.0 K (dark grey).

6.2.3 Nonlinear and temperature dependent conductance

We investigate regions (1) to (3) from Figure 6.5 in temperature dependent and nonlinear conductance measurements. We first present the measurements for the three regimes going into detail only with specific features and thereafter discuss their general properties.

Region (1): Asymmetric resonances with $q < 0$

Region (1), corresponding to a plunger gate voltage range from $V_G = -0.68$ V to -0.65 V, is investigated in Figure 6.7. The lineshapes in the linear conductance measurement in (b) are clearly asymmetric Fano resonances. The fits from the previous section yield Fano asymmetry parameters $q = -1.4$, $q = -1.2$ and $q = -0.9$ for the three resonances shown. The Fano resonances decrease when the temperature is increased and totally vanish at $T = 1$ K. The background conductance is still present at $T = 1$ K and does not seem to be substantially

influenced. Increasing the temperature broadens the Fano resonances, so that in a simple model one could consider the negative edge of one resonance to cancel the nearby positive edge of the next resonance. This together with a decrease in amplitude explains the vanishing of the resonances at high temperatures. The Fano parameter q , however, does *not* depend on temperature.

In the nonlinear conductance measurements from Figure 6.7(a) we observe Coulomb diamonds. In contrast to the ordinary Coulomb blockade regime, the edges of the diamonds are not marked by peaks of high conductance but by a high-low conductance combination in agreement with the linear conductance lineshape. Additional high-low conductance features, e. g. the one highlighted by the thin white line, are attributed to tunnelling through excited states (section 2.3.4). The marked feature is about 2 mV in gate voltage apart from the edge of the Coulomb diamond, from which we estimate an excitation energy of $\Delta\varepsilon \sim 100 \mu\text{eV}$ consistent with the discussion in section 4.3.3.

The standard analysis for Coulomb diamonds following chapter 4.3 yields the following results: From the width of the Coulomb diamonds in V_{SD} , a charging energy of $U \approx \Delta V_{SD}/(2e) \approx 0.3 \pm 0.05 \text{ meV}$ and a total capacitance of $C_{\Sigma,SD} \approx 535 \text{ aF}$ is extracted. The slopes in the Coulomb diamonds are roughly $m_S = \Delta V_G/\Delta V_{SD} \approx 17 \pm 2$ and $m_D \approx 18 \pm 2$, leading to a lever arm of $\alpha_G \approx 0.029$ and a total capacitance of $C_{\Sigma,\alpha} \approx 550 \text{ aF}$. Both results for the total capacitance are in good agreement. This analysis is summarized in Table 6.1 on page 119.

Region (2): Anti-resonances with $q = 0$

Between plunger gate voltages of $V_G = -0.62 \text{ V}$ and -0.056 V we observe clear, fairly symmetric Fano anti-resonances (Figure 6.8). They correspond to a Fano asymmetry parameter of $q = 0$ as confirmed by the fits from the previous section from which we get $-0.2 < q < 0.2$ for all resonances shown. The temperature dependence is similar to region (1): The resonance dips become wider and decrease in amplitude when the temperature is increased. At $T = 1 \text{ K}$ the dip structure has almost vanished. From Coulomb blockade it is known that the valley conductance increases with increasing temperature, in particular if the peaks overlap. The valleys from the Coulomb regime correspond to

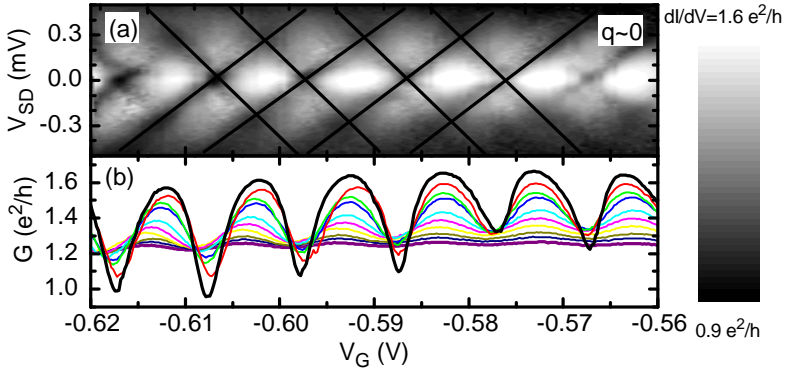


Figure 6.8: In region (2), between $V_G = -0.62$ V and -0.56 V we observe symmetric Fano-dips with $q = 0$ superimposed on a nearly level background conductance: (a) Grey scale plot of the differential conductance, showing Coulomb anti-diamonds highlighted by black lines. (b) Linear ($V_{SD} = 0$) conductance in the corresponding plunger gate voltage range for the same temperatures as in Figure 6.7(b). Clear anti-resonances vanishing with increasing temperature are found.

the maxima between the dips observed here. These maxima decrease with rising temperature which is attributed to the fact that we observe anti-resonances instead of resonances. The valley amplitude in the resonant channel increases when increasing T which results in an effectively decreased transmission after interference with the non-resonant background channel.

The nonlinear conductance measurement in Figure 6.8(a) looks similar to the results from the regular Coulomb blockade regime with the Coulomb diamonds inverted. We do not observe Coulomb diamonds but anti-diamonds. We have summarized the parameters extracted from these measurements in Table 6.1 on page 119.

Region (3): Asymmetric resonances with $q > 0$

The region $V_G = -0.55$ V up to -0.52 V investigated in Figure 6.9 is similar to region (1) ($V_G = -0.68$ V – -0.65 V) except for an opposite

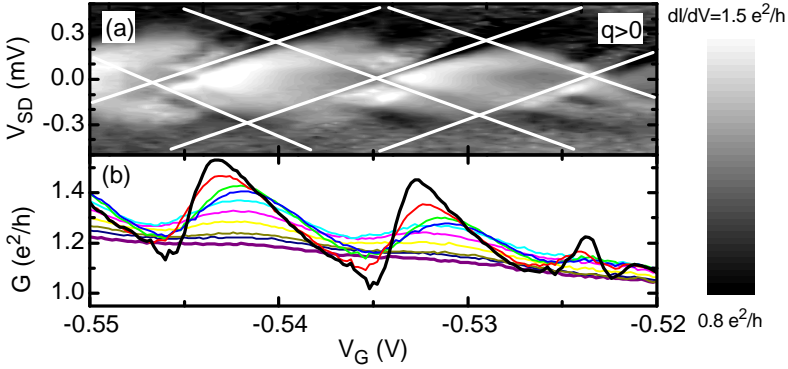


Figure 6.9: Asymmetric Fano resonances with $q > 0$ are found for plunger gate voltages from $V_G = -0.55$ V to -0.52 V in region (3): (a) Grey scale plot of differential conductance with Coulomb diamonds highlighted by white lines. (b) Linear ($V_{SD} = 0$) conductance for the same temperatures as in Figure 6.7(b).

symmetry of the Fano resonances. The fits yield $q = 1.2$ for both resonances shown here. Although the Coulomb diamonds are less clear than in the previous regions, we have extracted the relevant parameters which are presented in Table 6.1 on page 119 again.

Discussion of the “Coulomb diamonds” in the three Fano regions

The parameters extracted from the Coulomb diamonds in regions (1)-(3) are summarized and compared to the results for the Coulomb blockade regime in Table 6.1. Within the considerable measurement error, all results for the Fano regime agree. But compared to the Coulomb regime, the total capacitance in the Fano regions has doubled. This is attributed to an increased dot diameter and to decreased tunnelling barriers at higher plunger gate voltages ($V_G \sim -0.6$ V vs. $V_G \sim -1.15$ V). The latter increase source- and drain capacitances and thus the total capacitance, $C_\Sigma = C_S + C_D + \dots$

The diamond-shaped structures in the nonlinear conductance measurements are in good agreement with the two-channel model of Fano

	from ΔV_{SD}		from slopes	
	U (meV)	$C_{\Sigma,SD}$ (aF)	α_G	$C_{\Sigma,\alpha}$ (aF)
Region 1 ($q < 0$)	0.3	535	0.029	550
Region 2 ($q = 0$)	0.3	535	0.027	590
Region 3 ($q > 0$)	0.3	535	0.024	670
regular CB	0.6	270	0.045	270

Table 6.1: Parameters extracted from the “Coulomb diamonds” in the three Fano regions from Figure 6.5 in comparison to the regular Coulomb-blockade regime at $V_G \sim -1.15$ V. The results for the Coulomb regime are taken from Table 4.1 on page 62.

resonances in SETs introduced in section 6.1.3. They demonstrate that the Fano resonances depend on V_{SD} and V_G in the same way as Coulomb resonances: The non-resonant background conductance channel is not considerably influenced by a finite source-drain voltage V_{SD} . The resonant channel, however, is from Coulomb resonances and thus strongly depends on V_{SD} . Coulomb resonances exhibit a similar diamond pattern in nonlinear conductance (chapter 4.3). By the interference of both channels the resonance lineshape is changed from Coulomb to Fano, but the positions of the resonances in V_{SD} and V_G remain unaffected. Hence, instead of diamonds formed by peaks we observe diamonds which are formed by asymmetric structures or most strikingly “anti”-diamonds.

In the discussion on Kondo physics at finite source-drain voltages on page 91 we found that the singlet states between electrons on the quantum dot and in the leads are destroyed by bias voltages of a few hundred microvolt due to decoherence. In interference phenomena like the Fano resonances discussed here coherence is also an issue. An increased decoherence would result in the interference to be destroyed. Then equation 6.13 instead of 6.12 increasingly governs the total conductance. The Fano resonances would gradually develop into Coulomb resonances superimposed on the non-resonant background conductance.

We do not observe decoherence with increasing bias voltage, our system is robust in this respect. This is in contrast to the results of Kobayashi and coworkers who investigated Fano resonances in a quan-

tum dot embedded into one arm of an Aharonov-Bohm ring [120]. With a ring circumference of $L \sim 4 \mu\text{m}$ their system is rather large compared to an electron mean free path of $l_e \sim 8 \mu\text{m}$ in their heterostructure which imposes a lower limit on the phase coherence length at low temperature. A small bias voltage in their experiment is sufficient to destroy the coherence between the two Fano channels. With an electronic quantum dot diameter of $L \sim 250 \text{ nm}$ our system is much smaller than theirs. In addition the mean free path of $l_e \sim 13 \mu\text{m}$ is slightly larger in our heterostructure. The larger ratio of the dimensions of our system to the mean free path explains the increased robustness with respect to V_{SD} in our experiment.

Discussion of the temperature dependencies

The Fano resonances in our experiment vanish with increasing temperature while the background conductance remains essentially unaffected. This indicates a strong temperature dependence of the resonant transmission channel, while the background transmission depends only little on temperature.

We have determined the amplitude and width of an anti-resonance in region (2) at $V_G = -0.598 \text{ V}$. Figure 6.10(a) shows fits of equation 6.5 to the anti-resonance for various temperatures between $T = 70 \text{ mK}$ and 500 mK . For higher temperatures the overlap with neighboring anti-resonances becomes too strong for a fit to a single anti-resonance to make sense. In the fits we assumed a constant non-resonant background transmission of $a_{nr}^2 = A_{Exp} + B_{Exp} = 1.75 e^2/h$.

As illustrated by Figure 6.10(b), the lineshape parameter q indeed remains unaffected by a change in temperature as already realized earlier. In analogy to the discussion on nonlinear conductance we conclude that temperatures of $T \sim 0.5 \text{ K}$ do not introduce decoherence between the two Fano channels. A loss of coherence would lead to a transition from Fano to Coulomb lineshapes. Kobayashi and coworkers observed such a transition at $T \sim 0.2 \text{ K}$ in their larger structure. Hence with respect to decoherence our small Fano system is more robust not only against finite bias voltages (previous section) but also against an increase in temperature.

We have also analyzed the width (FWHM) of the anti-resonance as a

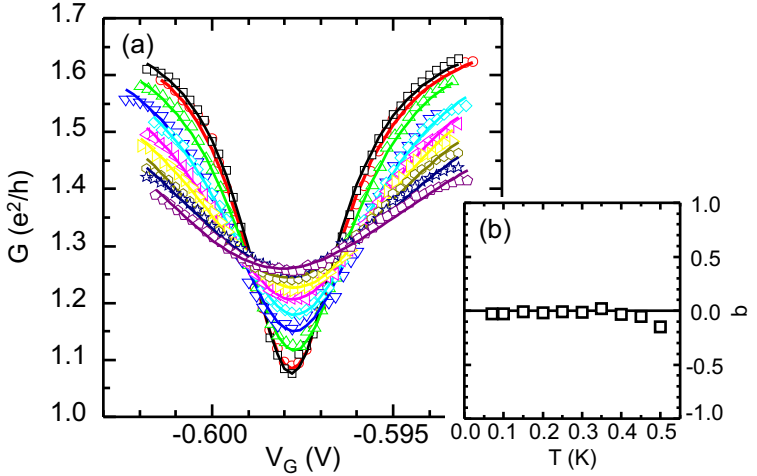


Figure 6.10: (a) Fits to a Fano anti-resonance for temperatures between $T = 70$ mK and 500 mK. (b) Fano asymmetry parameter q versus temperature extracted from the fits.

function of temperature in analogy to the classical analysis of Coulomb resonances in chapter 4.2. In Figure 6.11(a) we present the linewidths extracted from the fits in Figure 6.10. The linear dependence of the squared FWHM on T^2 is in agreement with the Coulomb regime and thus confirms that the resonant channel is from Coulomb blockade. From the slope in Figure 6.11(b) we extract a lever arm of $\alpha \approx 0.015$ in rough agreement with the result from the nonlinear conductance measurements.

We have extracted the parameters of the two-channel model from the fits in the same way as in section 6.2.2. Here we are interested in the temperature dependence of the resonant channel. Figure 6.11(b) shows its transmission probability which apart from saturation at low and high temperatures decreases logarithmically with increasing temperature. To confirm this result, we have also determined the amplitudes of the anti-resonances with respect to the background, $\Delta G = G_{Peak} - G_{Valley}$. Compared to our four-parameter fits, this analysis is more simple and reliable. It could be employed for temperatures of

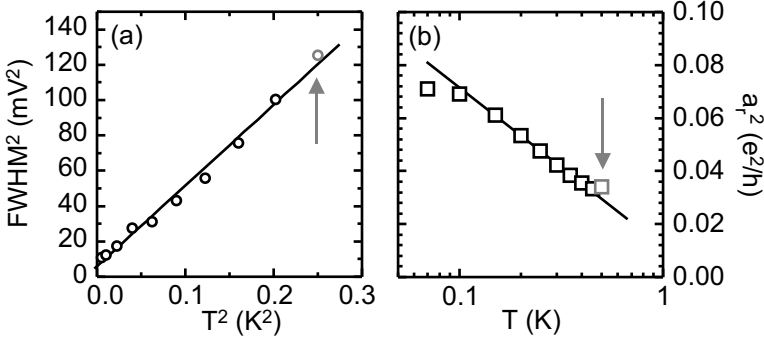


Figure 6.11: (a) Amplitude of the resonant channel in the two-channel model as a function of logarithmic temperature extracted from the fits in Figure 6.10. (b) Quadratic peak widths (FWHM) from the fits versus quadratic temperature. For both graphs, the data becomes unreliable at high temperatures as marked by the arrows because of the beginning overlap of the peaks in the resonant channel.

up to $T = 1$ K. Results for four anti-resonances and a Coulomb-like resonances at still higher coupling for comparison are shown in Figure 6.12. The qualitative characteristics of resonance and anti-resonances are the same and agree with the result from the fit. As for the fit, the high temperature results have to be interpreted with caution because of the overlap of neighboring peaks.

Göres *et al.* in Reference [20] speculated about an influence of Kondo physics in their Fano experiment because of the logarithmic temperature dependence of ΔG . Although we observe a similar temperature dependence in our experiment we cannot confirm their speculations because of the strong overlap of our resonances. This is clarified in the inset in Figure 6.12 which shows a calculation of ΔG for a quantum dot in the finite temperature regime (chapter 2.4) considering the overlap of neighbor Coulomb resonances. The dotted curve illustrates a saturation at low temperatures due to reaching the low temperature limes (see again chapter 2.4). The result qualitatively agrees with our data without considering a Kondo effect. Overlapping Coulomb resonances in the non-resonant channel are sufficient to explain our results.

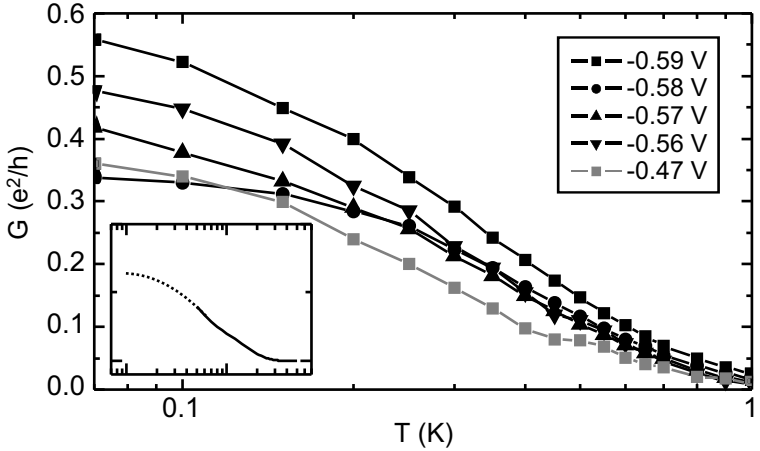


Figure 6.12: Modulation amplitudes $\Delta G = G_{Peak} - G_{Valley}$ of several resonances as a function of temperature T . The amplitude of Fano anti-resonances is shown in black, the grey trace corresponds to a Coulomb-like resonance at even stronger coupling for comparison. The respective plunger gate voltages V_G are listed in the legend. Inset: Qualitative conductance modulation amplitude for Coulomb resonances in the finite temperature regime from chapter 2.4 as a function of temperature. The dotted curve sketches the saturation at low temperatures.

We conclude that for temperatures of up to 1 K no decoherence is introduced. We have confirmed our two-channel model of a temperature dependent Coulomb-like resonant channel interfering with a temperature independent non-resonant channel.

6.2.4 Tuning Fano resonances in small magnetic fields

In this section we investigate the influence of a perpendicular magnetic field B on the Fano resonances. If the Fano channels are arranged in such a way that the magnetic flux penetrates an area between the channels, a magnetic field will affect the phase shift between these paths and thus change the interference pattern. This is in analogy to the Aharonov-Bohm effect [119, 31] and is manifested in a modified

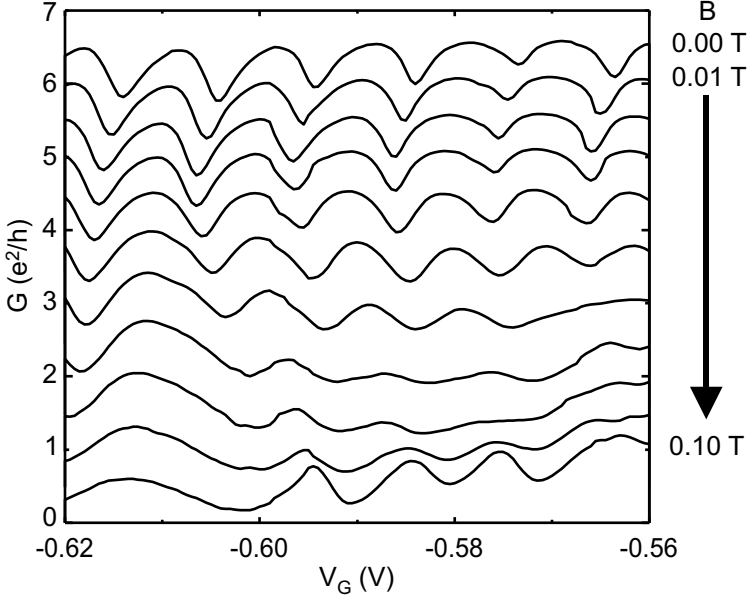


Figure 6.13: Linear conductance G in region (2) as a function of gate voltage V_G for magnetic fields between $B = 0$ T and 100 mT in steps of 10 mT. The gate voltage range of region (2) with symmetric Fano anti-resonances is shown.

Fano asymmetry parameter q . E. g., for a variation of the non-resonant phase φ_{nr} from 0 to π , q changes from ∞ to 0 and resonances become anti-resonances. For intermediate phase shifts the lineshapes become asymmetric. This lineshape variation is periodic with a periodicity ΔB . Considering a circular area with radius r between the channels, the oscillation period is

$$\Delta B = \frac{\phi_0}{\pi r^2}. \quad (6.20)$$

$\phi_0 = h/e$ is the magnetic flux quantum. In classical Aharonov-Bohm experiments with ring structures the ring diameter can be determined from the oscillation period. We analyze our data in this context.

In Figure 6.13 we present measurements of Fano anti-resonances in

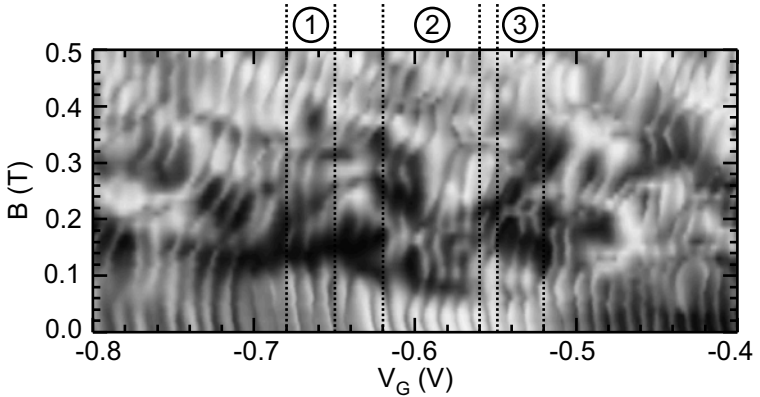


Figure 6.14: Grey scale plot of the linear conductance as a function of magnetic field B and gate voltage V_G . The regions (1)–(3) from Figure 6.5 are marked.

region (2) for magnetic fields up to 0.1 T. The gate voltage position of the anti-resonances slightly varies with increasing B , but the general lineshape and thus q remains unaffected up to 60 mT. Then the anti-resonances vanish, and finally at 100 mT a new sequence of peaks emerges. We cannot clearly distinguish whether these new structures consist of resonances or anti-resonances.

Considering $\Delta B = 60$ mT as a lower bound for one quarter oscillation period, i. e. $\Delta\varphi_{nr} = \pi/2$, we determine $d = 150$ nm as an upper bound for the diameter of the area enclosed by the two channels. $\Delta\varphi_{nr} = \pi/2$ corresponds to a transition of symmetric Fano resonances to asymmetric ones, e. g. from $q = 0$ to $q = 1$. Thus this phase shift would be clearly visible. Because the diameter of $d = 150$ nm we determine is smaller than the approximate electronic dot diameter of $d_{el} = 250$ nm (chapter 3) we rule out that the non-resonant background channel somehow circumvents the dot. A circumvention of the dot would result in a greater area enclosed by the two channels. This result of a small Fano system is in agreement with its robustness against decoherence which also suggests a very compact and small system.

The variation of the anti-resonance positions in gate voltage inhibits

to clearly follow a resonance as function of magnetic field. Such a variation of a peak position is already known from chapter 4.4.2 for high magnetic fields. The mechanism behind this phenomenon is related to the internal electronic structure of a quantum dot in a magnetic field. Figure 6.14 shows these shifts for a larger range of gate voltage and magnetic field. The shifts are rather complicated, in the Coulomb as well as in the Fano regime. Their observation in the Fano regime confirms our identification of the resonant conductance channel with Coulomb oscillations in the SET. Unfortunately they also prevent to clearly examine the evolution of the phase shift between the Fano channels reflected in q .

6.3 Background transmission channel

So far we have understood our Fano system quite well and have shown that the resonant channel exhibits all the features typical of Coulomb blockade in a SET. The non-resonant background transmission channel, however, remains puzzling. In this section we present some model calculations considering different evolutions of the complex background transmission to demonstrate its influence on the Fano resonances. Furthermore, we discuss possible origins of the background transmission channel.

6.3.1 Model calculations of Fano resonances

Based on the model introduced in chapter 6.1.3, we have simulated the transmission of a quantum dot in the Fano regime for two given evolutions of the non-resonant background conductance. We have first anticipated a background transmission amplitude and phase shift resembling the results from section 6.2.2. Thereafter, we investigate a continuous background amplitude and phase evolution, namely a wide resonance which varies so slowly that it can be considered nearly constant over each Coulomb resonance.

Model (1) for a non-resonant background conductance

In this section we have chosen the background transmission to reproduce the results from section 6.2.2. Transmission amplitude and phase shift of the background channel are shown in Figure 6.15(a). They reflect the step-like behavior suggested in Figure 6.5(b). The transmission of the Coulomb channel, a series of uniform Coulomb resonances with the respective phase evolution, is depicted in Figure 6.15(b). According to Reference [122] the phase varies from $\varphi_r = -\pi/2$ to $\pi/2$ for each Coulomb resonance with a phase lapse of π in between. From these components we have calculated the total transmission amplitude including interference according to equation 6.12. The result is shown in Figure 6.15(c).

In the total transmission amplitude at each Coulomb-resonance position a Fano resonance is observed. For a background phase shift of $\varphi_{nr} = 0$ or equivalently 2π and $T_{nr} = 0.5$ we observe Breit-Wigner-type Coulomb resonances. At higher energies, for $\varphi_{nr} = 3\pi/2$ and $T_{nr} = 1$, we find asymmetric Fano resonances with $q < 0$. $\varphi_{nr} = \pi$ and $T_{nr} = 2$ lead to anti-resonances ($q = 0$) and $\varphi_{nr} = \pi/2$ and $T_{nr} = 1$ to asymmetric Fano resonances with $q > 0$. Finally, for $\varphi_{nr} = 0$ and $T_{nr} = 0$ we get symmetric Coulomb resonances again. Thus the calculation reproduces the lineshapes observed in the experiment. In this way we explain the variation of the Fano parameter q with the evolution of the background transmission T_{nr} and phase shift φ_{nr} .

Model (2) for a non-resonant background conductance

As an alternative to the calculation from the previous section we have considered a non-resonant background conductance resembling a broad resonance. This model is no contradiction in itself because the resonance in the background channel varies slowly enough to be considered constant (and thus non-resonant) over each comparably narrow Coulomb resonance. The smooth evolution of the background channel might be feasible considering the alternative, smooth variation of q in Figure 6.5(b).

Figure 6.16 shows the results of our calculation in analogy to Figure 6.15. The resonant channel is the same as in the previous section, but

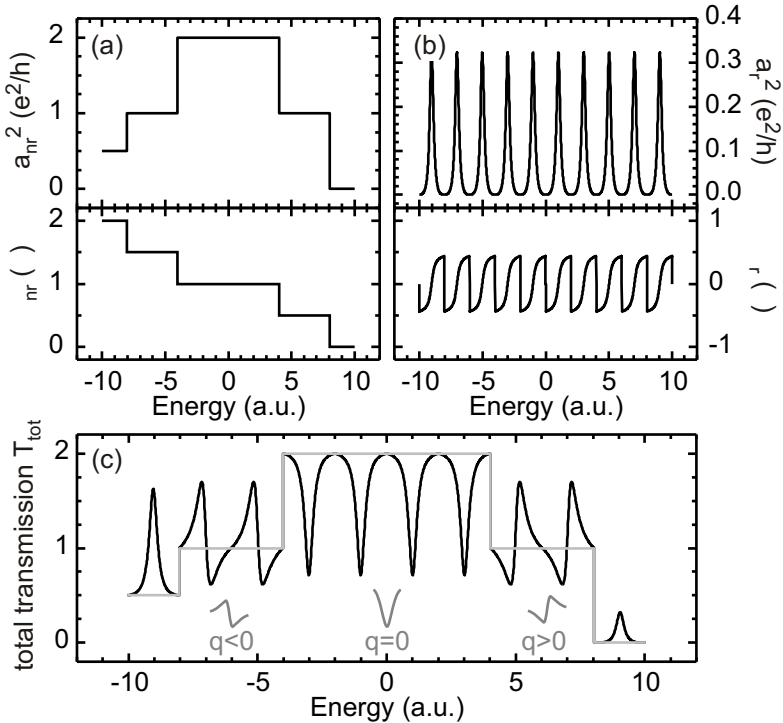


Figure 6.15: Model calculation (1) of Fano resonances and anti-resonances with a background transmission resembling the results from Figure 6.6. (a) shows transmission amplitude and phase of the non-resonant background channel, (b) of the resonant channel, and (c) the resulting total transmission probability proportional to the conductance. In (c), the background transmission amplitude from (a) is shown in grey for comparison.

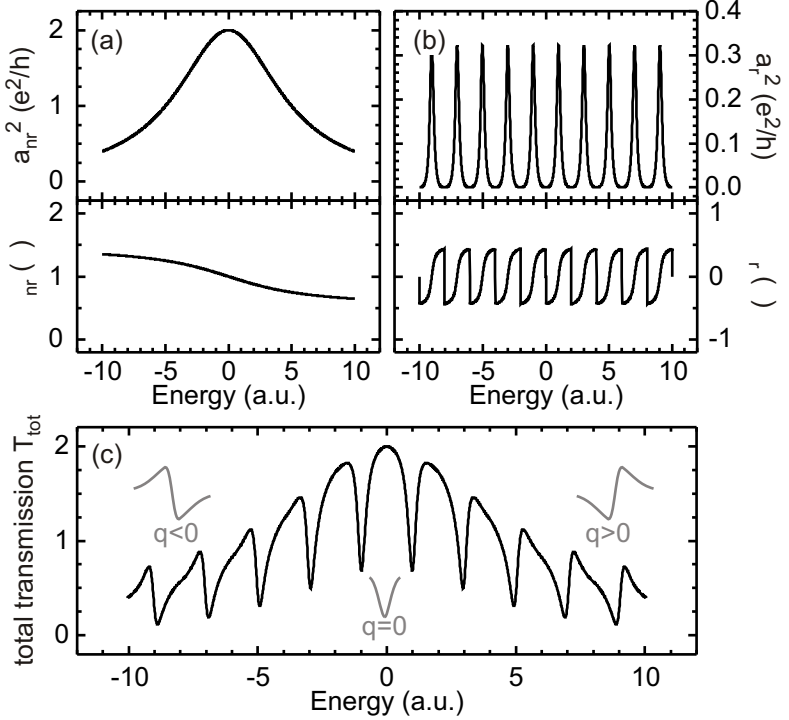


Figure 6.16: Model calculation (2) of Fano resonances and anti-resonances similar to Figure 6.15 but considering a wide resonance in the background transmission. (a) Transmission amplitude and phase of the background channel, (b) the same for the resonant channel, (c) resulting total transmission probability.

the (virtually) non-resonant background channel exhibits an extremely broad resonance. Its phase is assumed to vary from $\varphi_{nr} = 3\pi/4$ to $\pi/2$. These parameters reproduce the correct overall variation of the Fano lineshapes in the total transmission with Fano parameters of $q < 0$, $q = 0$ and $q > 0$. The details of the experimental data in Figure 6.5, however, are better reproduced by the background transmission used in calculation (1), although the model considered here seems more natural and appealing.

Influence of Kondo-type resonances instead of Coulomb resonances in the resonant channel

In the above calculations, we have considered Coulomb-type resonances in the resonant channel. Since the quantum dot under study in this chapter also shows a Kondo effect (chapter 5), we will briefly consider how this would influence the total transmission lineshape. In the Kondo regime, the transmission of the resonant channel changes from Coulomb to Kondo type with a different amplitude and phase evolution [128, 123, 124]. In the unitary limit the phase evolves linearly from $-\pi/2$ to $\pi/2$ when a Kondo resonance including *both* former Coulomb peaks is crossed. Interference with a non-resonant transmission channel leads to characteristic Fano-Kondo resonances predicted by Hofstetter *et al.* [129]. Fano-Kondo resonances are wider than Coulomb-deduced Fano resonances as a Kondo resonance extends over a complete Coulomb valley. As they are related to a Kondo effect, they also strongly depend on temperature and collapse when reaching T_K . Fano-Kondo resonances become most clearly visible when the unitary limit is reached, a condition by far not reached in the Kondo effect in our dot. Since our two-channel model deduced from Coulomb-blockade describes the experimental resonance lineshape very well and because of the lack of a strong temperature dependence, we believe that a Kondo effect cannot play a major role in our Fano experiment.

6.3.2 Origin of the non-resonant transmission channel

The puzzle about the exact origin of the non-resonant background transmission channel in our experiment has not yet been solved. Here

we discuss conceivable scenarios:

Channels bypassing the dot in the plane of the 2DES

From lithography there is no second conductance channel circumventing the dot in the plane of the 2DES. Considering the transport measurements in a perpendicular magnetic field from section 6.2.4, this scenario becomes even more unlikely as we found that the dimensions of our Fano system in the plane of the 2DES are very small, $d \leq 150$ nm. Thus we can rule out a second path that circumvents the dot.

Dot split into two smaller droplets

It is not unlikely that quantum dots split into several smaller droplets due to the potential created by nearby donors or impurities. This is discussed for example in Reference [55]. However, the clear measurements from chapters 4 and 5 evidence that our structure is very clean. The Fano regime discussed in this chapter is observed at even higher gate voltages than the previous Coulomb and Kondo regimes. Therefore the influence of impurities at the bottom of the dot potential should be decreased. Furthermore, the increased number of electrons at higher gate voltages improves screening. Thus we also exclude a splitting of the dot into smaller droplets due to impurities.

Cotunnelling

Due to the high plunger gate voltages employed in the Fano regime the tunnel barriers are comparably low in this regime. This effect increases the probability of cotunnelling which could be a likely origin of a second transmission channel. In the cotunnelling regime, however, an increased temperature is expected to further increase cotunnelling in contrast to our experimental findings. In addition, at $V_G \sim -0.45$ V we observe regular Coulomb resonances with a low background conductance indicating only a small cotunnelling contribution, if any (Figure 6.4 on page 111). This gate voltage is more positive than those applied in the Fano regime, thus if cotunnelling plays a role it is expected to increase and not to decrease. Cotunnelling is not a likely origin of the non-resonant transmission channel.

Second subband in the 2DES

The properties of the heterostructure from which the sample was fabricated could also influence the formation of a non-resonant conductance channel. In the triangular potential well in the z -direction of our heterostructure only the ground state is expected to be occupied (chapter 3.1 and appendix C), i. e. one two-dimensional subband in the 2DES is occupied. But at sufficiently high electron densities occupation also of the second subband of the heterostructure starts. This could provide a second channel through the quantum dot. As the electronic wave functions for the second subband are centered deeper in the heterostructure and therefore farther away from the charged top gate electrodes this channel could be non-resonant. Screening from electrons in the above first subband is another effect flattening the potential created by the top gates and making the channel in the second subband less resonant. However, for the Fano resonances to emerge the electronic wave functions must split between the two subbands at the first tunnel barrier and join again at the second one. It is not clear how this splitting works.

To clarify whether a second subband might be occupied in our heterostructure we have simulated its band structure for various gate voltages V_{gate} . Details on the simulation are found in appendix C. Figure 6.17 shows that not only the electron density n_e but also the occupation of the second subband is varied as a function of V_{gate} . In the simulation, at $V_{gate} = -0.14$ V the energy E_2 of the second subband crosses the Fermi level E_F . This is where its occupation starts for increasing V_{gate} . Due to unknown concentrations of dopants and background impurities the simulation is not completely reliable. In particular, we cannot deduce the exact gate voltage for the population of the second subband in the experiment. It is possible that the second subband comes into play at just the plunger gate voltages where the Fano resonances set in.

We have also employed Hall and Shubnikov-de Haas measurements in which the electron density was increased by illumination and application of positive backgate voltages. When the occupation of the second subband starts this is visible in Hall density, mobility and the emergence of a second Shubnikov-de Haas oscillation periodicity [130].

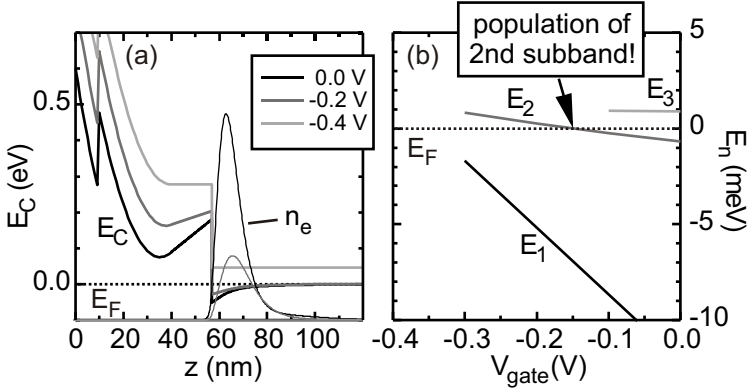


Figure 6.17: Simulated band structures of our heterostructure showing an occupation of the second subband as a function of the voltage V_{gate} of a top gate electrode. (a) Conduction band offset E_C (thick lines), Fermi level $E_F = 0$ (dotted line) and resulting electron densities n_e (thin lines) for V_{gate} as indicated in the legend. (b) Energies E_n of the n th subband versus V_{gate} with respect to the Fermi energy $E_F = 0$.

In our measurements we found some indications of a second subband but no clear evidence [131].

Rapid ballistic traversal of the dot

Göres *et al.* proposed the non-resonant conductance channel in their quantum dot to be related to electrons traversing the dot ballistically [20]. Due to Heisenberg's uncertainty relation $\Delta E \Delta t \geq \hbar$, at a sufficiently small charging energy a ballistic electron might rapidly traverse the dot despite Coulomb blockade.

We check whether this model is a possible explanation for the second channel in our dot: The charging energy in the Fano regime is $U = 300 \mu\text{eV}$ (table 6.1 on page 119). With a bulk 2DES electron density $n_e = 3.7 \cdot 10^{15} \text{ m}^{-2}$ we get a Fermi velocity of $v_F = \hbar \sqrt{2\pi n_e} / m^* = 2.5 \cdot 10^5 \text{ m/s}$, and considering that the ballistic electrons have to travel roughly the lithographic dot diameter of $d = 380 \text{ nm}$ (chapter 3.2) we

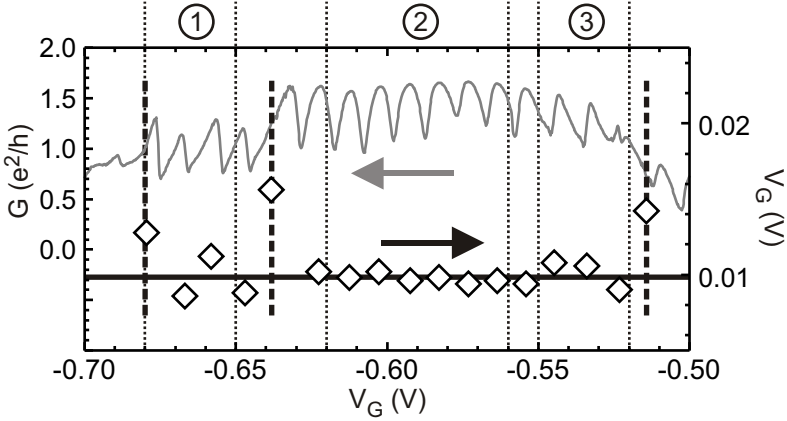


Figure 6.18: Distances between successive resonances in plunger gate voltage. The resonances are nearly equally spaced (thick black line) except at the positions marked by the dashed lines. The original linear conductance data (grey) is shown for comparison with the Fano lineshapes. Regions (1) to (3) are marked as in Figure 6.5.

get $\Delta E \Delta t = U d / v_F \approx 0.1h$. Because the real electron density in the dot and thus v_F is much smaller than in the bulk 2DES, we assume $\Delta E \Delta t \sim h$. Hence, it is possible for an electron to traverse our dot irrespective of Coulomb blockade in the Fano regime. In the Kondo and Coulomb regimes the charging energy is larger which keeps this channel closed.

The properties of the non-resonant background conductance channel reflected in q change at the borders of regions (1), (2) and (3). As illustrated in Figure 6.18, we observe a disturbed periodicity of the Fano resonances which is a signature of a charge reconfiguration on the dot at the left border of region (1), between regions (1) and (2), and at the right border of region (3). A reconfiguration of the charge distribution on the dot influences the potential landscape the rapid ballistic electrons in the non-resonant channel have to cross. It thus explains the jumps in the background transmission and in q between region (1)–(3) shown in Figure 6.5. The closure of the second conductance channel at

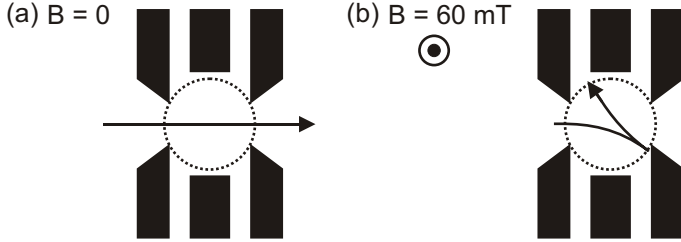


Figure 6.19: Trajectory of a rapid ballistic electron (a) at zero magnetic field and (b) at finite perpendicular magnetic field. Due to the magnetic field the ballistic path is effectively blocked.

$V_G \sim -0.5$ V might be due to a charge reconfiguration blocking this path through the dot completely. However, between regions (2) and (3) there is a jump in the background transmission which cannot be explained with a clear charge reconfiguration on the dot.

We do not expect any influence of temperatures $T < 1$ K on a ballistic non-resonant channel based on this mechanism. This is consistent with our experimental results where we did not observe any influence of temperature on the non-resonant channel (chapter 6.2.3).

In a magnetic field the ballistic electron trajectory is bent. Electrons traversing the dot on a straight trajectory at $B = 0$ are deflected at finite B as illustrated in Figure 6.19. Instead of leaving the dot at the exit tunnel barrier they are reflected by the neighboring walls of the confinement potential. Thus they are multiply reflected within the dot. Due to their extended stay in the dot they have to respect charging energy which effectively blocks the non-resonant channel. In chapter 6.2.3 we identified a typical magnetic field scale of $B \sim 100$ mT for changes in the Fano resonance pattern. This corresponds to a cyclotron radius of $l_{cycl} = \hbar k_F / eB = 1 \mu\text{m}$. So the magnetic field scale of changes in the non-resonant transmission is roughly consistent with what is expected for a ballistic electron in a dot with $d = 380$ nm. Illustration 6.19 resembles these dimensions.

To conclude, the model of a rapid ballistic traversal of the dot is consistent with our data.

6.4 Conclusions

We have studied Fano resonances in the conductance of our quantum dot as a function of plunger gate voltage in the extremely strong coupling regime. In contrast to previous works the resonances were stable and reproducible over a large gate voltage range. We were able to continuously tune the system from the Coulomb regime of weak dot-lead coupling and the Kondo regime of intermediate coupling to the Fano regime of extremely strong coupling. We observed three different regions in the Fano regime, each characterized by a unique lineshape and Fano parameter q . The lineshapes vary from asymmetric resonances ($q \sim -1$) to symmetric anti-resonances ($q = 0$) and back to asymmetric resonances ($q \sim 1$). The Fano symmetry parameter q up to $T = 1$ K is independent of temperature.

We explained the Fano resonances as an interference phenomenon of two transmission channels through the dot, a resonant channel from Coulomb blockade and a non-resonant one. We developed a two-channel model which was employed in the quantitative analysis of our data to verify that the resonant channel is from Coulomb blockade and to reveal information on the non-resonant conductance channel.

Interestingly, our Fano system is quite stable with respect to decoherence introduced by a finite bias voltage or by an increased temperature. We attribute the vanishing of the Fano resonances at further increased temperatures to broadening of the Coulomb resonances in the resonant channel alone and not to a reduced interference due to decoherence. This stability is strikingly demonstrated in the Fano anti-diamonds, inverted Coulomb diamonds observed in conductance measurements versus V_{SD} and V_G . The stability of our system is a consequence of the compactness of the Fano system with small spatial dimensions. Measurements in a perpendicular magnetic field confirm this thesis.

We discuss and assess several explanations for the non-resonant channel and find two likely alternatives, namely the involvement of a second subband in the heterostructure and a rapid ballistic channel not respecting charging energy. The latter could be a consequence of the reduced charging energy of the dot in the extremely strong coupled regime.

7 Summary and conclusions

This thesis covers three regimes of electronic transport through quantum dots. The regimes are distinguished by the coupling of the dot to the leads, and although each regime exhibits its own characteristic physics we can continuously tune our dots between them.

All experiments are based on single-electron tunnelling transistors (SETs) fabricated by a combination of optical and electron-beam lithography from a GaAs/AlGaAs heterostructure. The heterostructure forms a two-dimensional electron system 57 nm below the surface. By application of negative voltages to metallic split-gate electrodes atop the heterostructure we create a zero-dimensional quantum dot that is tunnel coupled to the two-dimensional leads. Tunnel coupling, internal energy levels, and the number of electrons confined in this device are tuned by the variation of the gate voltages and a perpendicular magnetic field. The temperature provides an additional means to influence this system.

In the weak coupling regime, transport in our SET is governed by Coulomb blockade and the unperturbed electronic spectrum of the dot. We determine the relevant parameters of our sample by temperature dependent and nonlinear conductance measurements in this well understood regime. We find a number of electrons confined on the quantum dot of $N \approx 150$. This number is varied by $\Delta N = 75$ by tuning the plunger gate voltage. Emphasis is put on magneto-transport spectroscopy in high magnetic fields where the electrons in the dot are organized in Landau levels. After isolating the influence of the emitter Fermi level on the magneto-conductance we determine the filling factor of the dot. We observe a redistribution of charges between Landau levels on the dot as a function of magnetic field. For certain fields, the emitter effectively becomes spin polarized leading to spin-blockade in

transport through the dot. After reaching filling factor one in the dot at high magnetic fields, the redistribution of charge between Landau levels stops and we observe infrequent transitions between maximum and lower density droplet states.

At strong coupling between dot and leads the Kondo effect and hence correlations between dot and lead electrons dominate transport. At zero magnetic field, we have thoroughly characterized this Kondo effect and found out that it extends over many subsequent Coulomb valleys, showing that electron spins in our dot are aligned according to Hund's rule. We have found the Kondo effect to be modulated in magneto-transport measurements similar to those in the Coulomb regime. Particularly between filling factor 3 and 4 this leads to an extremely regular, chessboard-like magneto-conductance which is modulated by the addition of single magnetic flux quanta. In contrast to previous studies, we observe Kondo physics in the high- as well as in the low-conductance tiles of the chessboard-like magneto-conductance with a modulation given only by the splitting of the Kondo peaks. The transitions are rather abrupt. The structure of the Kondo effect is in this regime more complicated than expected for a single electron with spin $1/2$, demonstrating that the electronic state of the dot is governed by many-particle correlations.

The modulated Kondo effect is suppressed when the emitter becomes spin polarized. By linking spin blockade to the coincident suppression of the Kondo effect we prove for the first time that the Kondo effect is a spin phenomenon relying on the presence of both spin orientations in the emitter.

Finally, we have shown that a SET may exhibit tunable Fano resonances at further enhanced coupling. In our sample these resonances were exceptionally stable and reproducible which enabled their thorough investigation. We interpret our Fano resonances in a simple two-channel model as an interference phenomenon between a resonant channel and an alternative, non-resonant conductance channel. We quantitatively analyze the properties of both channels as functions of temperature, magnetic field, plunger gate and bias voltage. The resonant channel comes from Coulomb blockade and exhibits typical characteristics, most strikingly Coulomb diamonds which are turned into anti-diamonds by tuning the second channel. We propose two possible

origins for the non-resonant channel, namely a second subband in the 2DES and a rapid ballistic traversal of the dot irrespective of charging energy due to Heisenberg's uncertainty principle. Transmission and phase of the non-resonant channel as functions of plunger gate voltage evolve in a non-continuous, step-like manner, pointing to reconfigurations of the charge distribution on the dot as a likely cause. They are not influenced by the other parameters. Our Fano system is very small as the phase of the background channel is not affected by a small magnetic field. This is confirmed by the robustness of the system with respect to decoherence introduced by a finite source-drain voltage or an increased temperature $T \leq 1$ K.

The observation of Coulomb, Kondo and Fano regimes in a single device demonstrates the wide and continuous tunability of split-gate SETs. This has allowed to control and study a correlated, mesoscopic many-electron system. After being the objective of active research for several years, in the future the Kondo effect might increasingly become a tool to gain further insight into the structure of such systems. The Fano regime of SETs has been neglected for a long time but might open new opportunities to study the transmission phase of electronic wave functions in addition to the established amplitude measurements.

A Symbols and notations

Symbols

α, α_i	lever arm (for gate i)
A	area
\vec{A}	magnetic vector potential, $B = \vec{\nabla} \times \vec{A}$
a_r, a_{nr}	transmission amplitudes of the resonant quantum dot and the non-resonant background channel
A_r, A_{nr}	squared transmission amplitudes of the resonant quantum dot and the non-resonant background channel
A_{Exp}	Fano fit parameter, $f_{Exp} = A_{Exp} \cdot f_{Fano} + B_{Exp}$
B, \vec{B}	magnetic field, in this thesis always applied perpendicular to the sample
B_{Exp}	Fano fit parameter, $f_{Exp} = A_{Exp} \cdot f_{Fano} + B_{Exp}$
C	capacitance
C_Σ	total capacitance of a quantum dot
ϵ_0	dielectrics constant
ϵ_r	relative dielectrics constant, in GaAs $\epsilon_r = 12.4$
ϵ, E	energy
ϵ_0	resonance energy
ϵ_i	energy for electronic dot level i due to quantum mechanical confinement
ϵ_n	electronic energy level in a magnetic field with Landau level index n
$\delta\epsilon$	detuning from resonance, $\delta\epsilon = \epsilon - \epsilon_0$
$\tilde{\epsilon}$	normalized detuning from resonance, $\tilde{\epsilon} = \delta\epsilon/(\Gamma/2)$

A Symbols and notations

$\Delta\varepsilon_i$	spacing of electronic dot energy levels i and $i + 1$, $\varepsilon_{i+1} - \varepsilon_i$
$\Delta\varepsilon$	constant spacing of electronic dot energy levels
e	elementary charge
E_F	Fermi energy
E_n	energy of the n th subband in the heterostructure
E_N	total energy of a quantum dot containing N electrons
f_{BW}	Breit-Wigner function, $f_{BW}(\tilde{\varepsilon}) = 1/(\tilde{\varepsilon}^2 + 1)$
f_{Exp}	function used to fit Fano resonances, $f_{Exp} = A_{Exp} \cdot$ $f_{Fano} + B_{Exp}$
f_{Fano}	Fano function, $f_{Fano}(\tilde{\varepsilon}) = (\tilde{\varepsilon} + q)^2/(\tilde{\varepsilon}^2 + 1)$
Γ	intrinsic resonance linewidth
g, g_{GaAs}	Landé g-Factor, in GaAs $g_{GaAs} = -0.44$
g_S	degeneracy due to spin
G	source-drain conductance at zero bias ($V_{SD} = 0$)
\mathcal{G}	degeneracy
h, \hbar	Planck constant, $\hbar = h/2\pi$
H	Hamiltonian
I	current
k_B	Boltzmann constant
k_F	Fermi wave vector, in a 2DES $k_F = \sqrt{2\pi n_e}$
λ_F	Fermi wavelength, $\lambda_F = 2\pi/k_F$
l_B	magnetic length, $l_B = \sqrt{\hbar/eB}$
l_{cycl}	cyclotron radius, $l_{cycl} = \hbar k_F/eB$
l_e	electron mean free path
μ_e	electron mobility of the 2DES
μ_B	Bohr's magneton
μ_N	chemical potential of a N -electron quantum dot
μ_S, μ_D	chemical potentials in source and drain reservoirs
m	orbital quantum number
m_e	mass of an electron
m^*, m_{GaAs}	effective mass of an electron, in GaAs $m_{GaAs} =$ $0.067m_e$
ν	filling factor $\nu = n_e/n_L$
n	Landau level index (neglecting Zeeman energy)
N	number of electrons on a quantum dot

n_e	electron density of a 2DES
n_L	degeneracy of a Landau level, $n_L = g_S \cdot eB/h$
ϕ_0	magnetic flux quantum, $\phi_0 = h/e$
φ_r, φ_{nr}	phase shifts of the resonant dot and the non-resonant background transmission channels
$\Psi, \psi, \Phi, \varphi$	wave functions
\vec{p}	momentum
q	parameter characterizing Fano lineshapes
Q	charge
ρ	density of state
ρ_e	resistivity
\vec{r}	position vector
R	ohmic resistance
\vec{S}, S	spin
S_z	z -component of a spin S
T	sample temperature
T_K	Kondo temperature
t_r, t_{nr}	complex transmission amplitudes of the resonant quantum dot and the non-resonant background channel
T_r, T_{nr}	transmission probabilities of the quantum dot and the non-resonant background channel
T_{tot}	total transmission probability
U	charging energy of a quantum dot
V	voltage
V_{ee}	electron-electron interaction potential
V_{ext}	external confinement potential
v_F	velocity of electrons at the Fermi level, $v_F = \hbar k_F/m^*$
ω_c	cyclotron frequency, $\omega_c = eB/m^*$

Notations

2DES	two-dimensional electron system
AC	alternating current
BG	backgate electrode (metalized chip carrier at the back of the sample substrate)

A Symbols and notations

D	drain contact (collector)
DAC	digital to analog converter
DC	direct current
G	plunger gate electrode
<i>h.c.</i>	hermitian conjugate
$\text{Im}(c)$	imaginary part of the complex number c
LDD	lower density droplet
LDOS	local density of states
MBE	molecular beam epitaxy
MDD	maximum density droplet
PMMA	polymethylmetacrylat (chemical used as e-beam resist)
QD	quantum dot
QHE	quantum Hall effect
$\text{Re}(c)$	real part of the complex number c
S	source contact (emitter)
SD	source-drain, e. g. in V_{SD} , I_{SD} , ...
SEM	scanning electron microscope
SET	single-electron transistor

B Sample fabrication and handling

In this appendix the preparation of the samples used in the experiments is described. “Recipes” are given for the most crucial lithography steps as well as some instructions for handling the delicate structures. This section is meant to help in the preparation of similar samples. It shall not replace a general introduction into micro- and nanolithography found e. g. in [45, 46].

Starting point for the fabrication of the samples is a GaAs/AlGaAs heterostructure forming a 2DES below the surface. After cutting the wafer into smaller chips of preferably 4 mm by 4 mm, Hall bars are

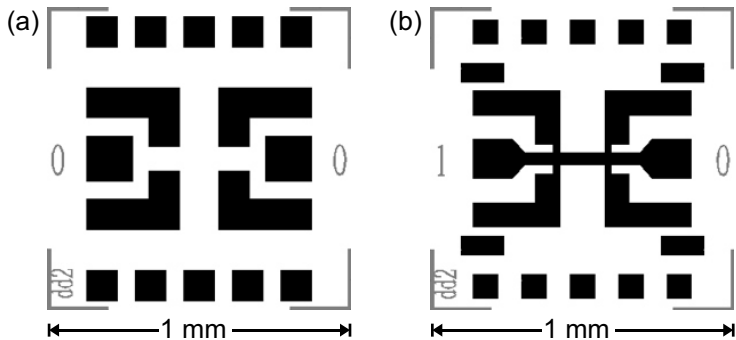


Figure B.1: Mask used for the optical lithography steps, namely (a) evaporation of ohmic contacts and (b) mesa etching. The actual mask contains arrays of 10 by 10 structures which allows to fabricate a large number of structures onto a single chip.

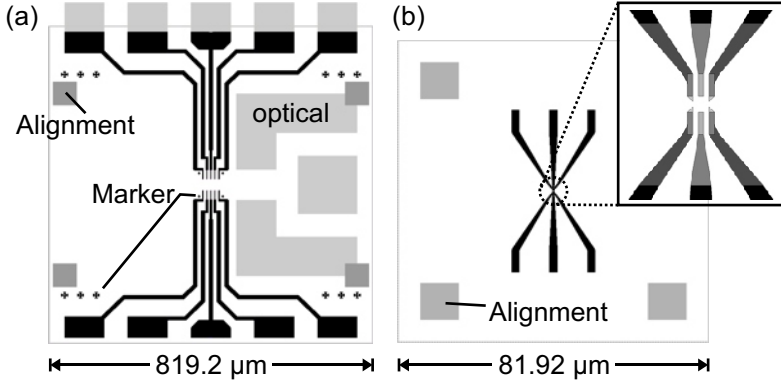


Figure B.2: Patterns used for electron beam lithography: (a) markers and wiring, (b) gates. In (a), some ohmic contacts from the optical lithography are shown for a better orientation. In the inset in (b), different shades of grey represent different exposure doses.

patterned onto these in two optical lithography steps. In the first step, Au/Ge/Ni ohmic contacts are fabricated in a lift-off process using the mask from Figure B.1(a). In the second step the mask from Figure B.1(b) is used for mesa etching. The gate structures are patterned using two electron beam lithography steps which are now explained in more detail.

B.1 Electron beam lithography

For electron beam lithography [46, 47] a LEO 1530 SEM with an Elphy deflection unit was used. As for connecting the bond pads with the actual finger gates a great difference in dimensions has to be overcome, two electron beam lithography steps are employed. The first step is carried out in a SEM writing field of $819.2 \mu\text{m} \times 819.2 \mu\text{m}$ and aligned to the edges of the outer ohmic contacts fabricated in the optical lithography. In this step, wires from the bond pads reaching a few μm onto the Hall bar are produced. Markers to allow the critical alignment of the second lithography step are also written. The extremely small split

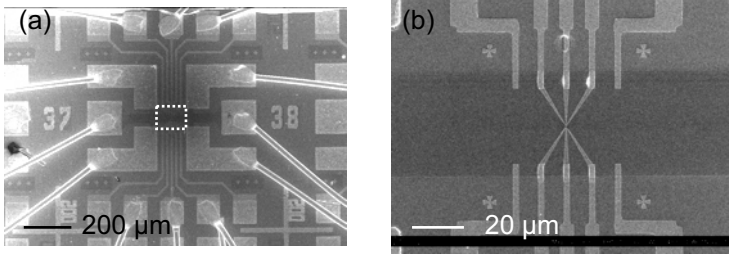


Figure B.3: SEM overview of the sample at magnifications (a) 180x and (b) 2000x. Bond pads and -wires, the Hall bar structure with its ohmic contacts, and gate electrodes are visible.

gate structures on the Hall bar are fabricated in a separate lithography step as the resolution of the SEM is not sufficient to write small structures at the low magnification of the large writing field. Additionally, a thinner metallization is needed for the smaller structures. The split gates are written using a $81.92 \mu\text{m} \times 81.92 \mu\text{m}$ SEM writing field. Both lithography patterns are displayed in Figure B.2. In particular in the pattern for the split gates the proximity effect [46] has to be considered and the exposure dose has to be varied accordingly over the structure.

A detailed listing for the electron beam lithography processing follows:

1. Coarse structure: marker and wiring

Cleaning: Clean the chip with acetone/propanol if necessary.

Coating: Spin coat the sample for 60 s with CoPo resist at 4000 RPM and bake for 10 min at $185 \text{ }^\circ\text{C}$. Add a second layer of 2% PMMA 950K using the same procedure.

Exposure: Write the pattern from Figure B.2(a) using a working field of $819.2 \mu\text{m} \times 819.2 \mu\text{m}$ and the according magnification. An acceleration voltage of 30 kV and a large aperture of $60 \mu\text{m}$ resulting in a beam current of 1 nA was used. All adjustments were optimized for a working distance of 4.0 mm. A useful beam step size for these parameters was 50 nm.

Development: Standard development in methyl isobutyl ketone : propanol in a ratio of 1 : 3 for 60 s, rinse with propanol, and blow dry with nitrogen.

Evaporation: Evaporate 8 nm Cr for adhesion and 60 nm Au onto the sample.

Lift-Off: Put the sample into an acetone bath for 5 min, then remove the waste Au by directing an acetone jet from a pipet onto the sample. Rinse the sample with acetone while removing it from the bath, swiftly switch to propanol and instantly dry clean with nitrogen.

2. Fine structure: gates

Cleaning: Clean the chip with acetone/propanol if necessary.

Coating: Spin coat the sample for 60 s at 4000 RPM with 2% PMMA 200K and bake for 10 min at 185 °C. Add a second layer of 2% PMMA 950K using the same procedure.

Exposure: Write the pattern from Figure B.2(b) using a working field of 81.92 μm x 81.92 μm and the according magnification. An acceleration voltage of 30 kV and the smallest aperture of 7.5 μm resulting in a beam current of approximately 12 pA was applied. Again, a working distance of 4.0 mm was used. A useful beam step size for these parameters was 5 nm in good relation to the dimensions of the pattern.

Development: Development is the same as in the previous lithography step for the coarse structure.

Evaporation: Evaporate 6 nm Cr for adhesion and 30 nm Au onto the sample. The layers are finer than in the previous step to help with the lift-off.

Lift-Off: This step is crucial for the small structures fabricated here. The sample is put into an acetone bath for at least 8 hours. Then the acetone bath is processed in an ultrasonic bath for 2 minutes. Rinse the sample with acetone while removing it from the acetone bath, swiftly switch to propanol and instantly dry clean with nitrogen. This process step has to be adjusted to produce the correct result.

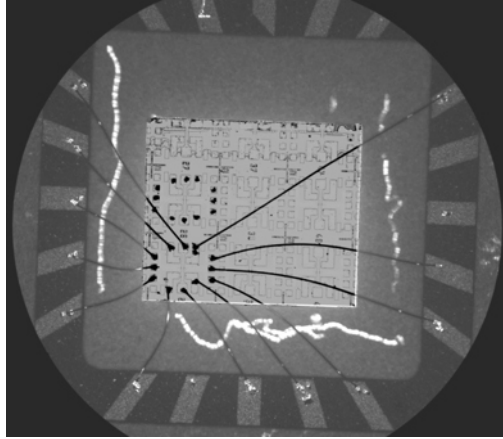


Figure B.4: Sample glued and bonded into a chip-carrier photographed through a light microscope.

Figure B.3 shows the finished structures, illustrating the large difference in scale which has to be overcome. The fine structure of the split gates is shown at a larger magnification in Figure 3.2 on page 33.

B.2 Mounting

The chips are split into smaller pieces containing some few samples and glued into chip-carriers using conductive silver paint (Figure B.4). The pads of one sample are then bonded to the carrier using $17.5\ \mu\text{m}$ gold wire. Starting with bonding, precautions against electrostatic discharges have to be taken (see next section).

B.3 Sample handling

Although an experimental detail, the handling of samples containing small metallic gate electrodes is a major challenge which may cause great frustration. A bonded sample is very susceptible to electrostatic

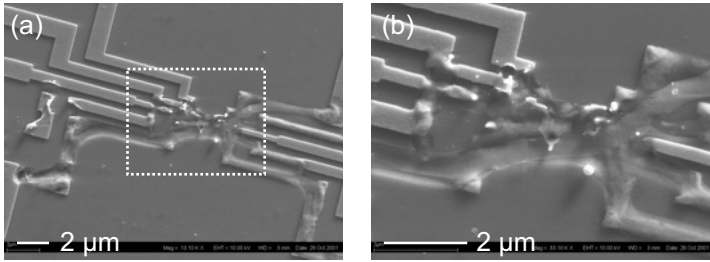


Figure B.5: Sample destroyed by electrostatic discharge. (a) Due to the discharge, in the centre of the structure all metallic gate electrodes have been evaporated. Apparently there is a trench on the sample surface along the path of the main discharge. (b) Magnification of (a) as marked.

discharge which results in a destruction of the gate electrodes as illustrated in Figure B.5. It is difficult to find out in which step such a destruction occurs, particularly as problems are not always visible under a light microscope, and not all samples seem to show the same degree of sensitivity to discharges. These are the most important precautions taken:

1. All work is performed on a conducting, grounded cloth and wearing an anti-static wrist strap.
2. The contacts connecting the 2DES are bonded first.
3. Bonded samples are stored on antistatic foam.
4. The cryostat itself and all lines to the chip-carrier holder are grounded prior to mounting the sample and during the whole process of cooling down.

C Parameters of heterostructure 1129

C.1 Characterization of the heterostructure

All samples discussed in this work are based on heterostructure 1129 grown by D. Reuter and A. D. Wieck at Ruhr-Universität Bochum. It was characterized in (quantum) Hall measurements [44] at low temperature of $T = 350$ mK. Hall and longitudinal resistance are shown

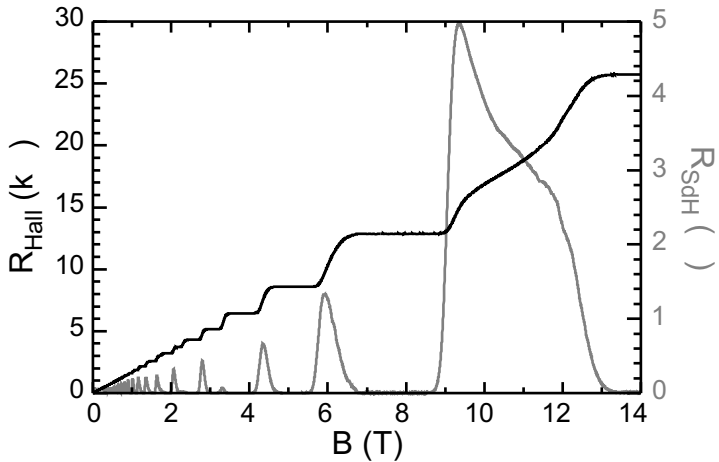


Figure C.1: Quantum Hall effect in heterostructure 1129 with conductance plateaus in the Hall resistance R_{Hall} and Shubnikov-de Haas oscillations in the longitudinal resistance R_{SdH} .

Material	Thickness	Doping concentration
GaAs:Si	10 nm	$0.85 \cdot 10^{18} \text{ cm}^{-3}$
$\text{Al}_{0.33}\text{Ga}_{0.67}\text{As:Si}$	30 nm	$0.85 \cdot 10^{18} \text{ cm}^{-3}$
$\text{Al}_{0.33}\text{Ga}_{0.67}\text{As}$	17 nm	-
GaAs	600 nm	-

Table C.1: Parameters for the self-consistent band structure calculation of heterostructure 1129.

in Figure C.1. We extract an electron density of $n_e = 3.7 \cdot 10^{15} \text{ m}^{-2}$ and a mobility of $\mu_e = 130 \text{ m}^2/\text{Vs}$.

C.2 Self-consistent Poisson-Schrödinger band structure calculation

The band structure of heterostructure 1129 was numerically calculated using a semi-classical Schrödinger-Poisson solver developed by G. Snider at the University of Notre Dame [132, 133, 134]. This computer program first solves the Poisson equation in one dimension for a given layer sequence and a known doping profile. In heterostructure 1129 a triangular potential well forms in the resulting conduction band profile. In this potential well the Schrödinger equation is solved in a second step.

Although a full three-dimensional simultaneous solution of the Schrödinger and Poisson equations considering even gate voltages would in principle be feasible [135], such a calculation is beyond the scope of this work for the extremely high computational effort and also for the limited accuracy of the result. Uncertainties in the exact composition of the sample considering every impurity atom lower the confidence in such calculations. Therefore the semi-classical and one-dimensional solution presented here is a good compromise between effort and attainable accuracy.

The parameters for the calculation are given in table C.1. The exact doping concentration is unknown when growing the heterostructure and was adjusted to give the correct charge density of the 2DES known

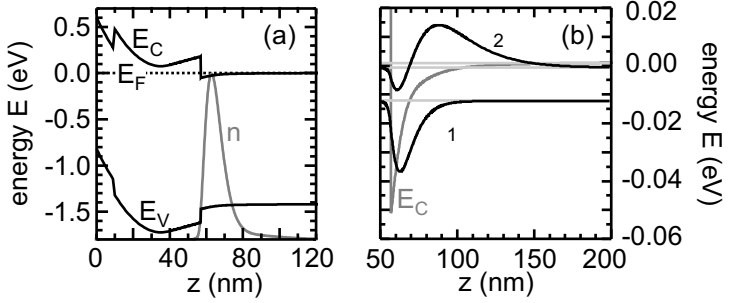


Figure C.2: Heterostructure 1129: (a) Calculated valence and conduction band profiles E_V and E_C and charge density n . (b) The Schrödinger equation was solved in the triangular well in the conduction band. Two bound states (grey) lie below the Fermi level E_F and a third one (also grey) above. The wave functions for the occupied states are shown in black.

from the Hall measurements in C.1.

Figure C.2 shows the numerically determined band structure of heterostructure 1129. The 2DES is formed in the triangular potential well. For the chosen parameters 2 subbands below the Fermi level are occupied. The occupation of the second subband depends critically on the parameters of the calculation. From this calculation it is not sure whether or not the second subband plays a role in transport, because the exact shape of the triangular potential well and thus the energy of the second subband is determined by the unknown background doping concentration.

D Additional data on sample 1129-8-7.3

In this appendix we report on additional data on sample 1129-8-7.3. This data is from the same sample and cooldown as the measurements presented chapters 4 and 5.

D.1 Coulomb peaks in high magnetic fields

We present additional data on Coulomb-peak positions and amplitudes at very high magnetic fields in complement to the discussion on maximum density droplets (MDDs) in chapter 4.4.4. The plunger gate voltage is tuned to extremely high values of $V_G \sim -0.5$ V since only in this regime the tunnel coupling is sufficiently strong to observe electronic transport despite high magnetic fields.

Figure D.1 shows Coulomb-peak positions and amplitudes versus B in continuation of Figure 4.18. We attribute the vanishing of regular cusps at $B \sim 9.2$ T to the formation of a MDD ($\nu_{dot} = 1$) and the following less frequent features to transitions to and between lower density droplets (LDDs). In the vicinity of $B = 11.5$ T the conductance of the quantum dot becomes too small to be distinguished from noise.

D.2 Transitions in the chessboard Kondo conductance

In chapter 5.4.3 the conductance of a quantum dot in the Kondo regime for dot filling factors $\nu_{dot} < 4$ is analyzed. It resembles a chessboard

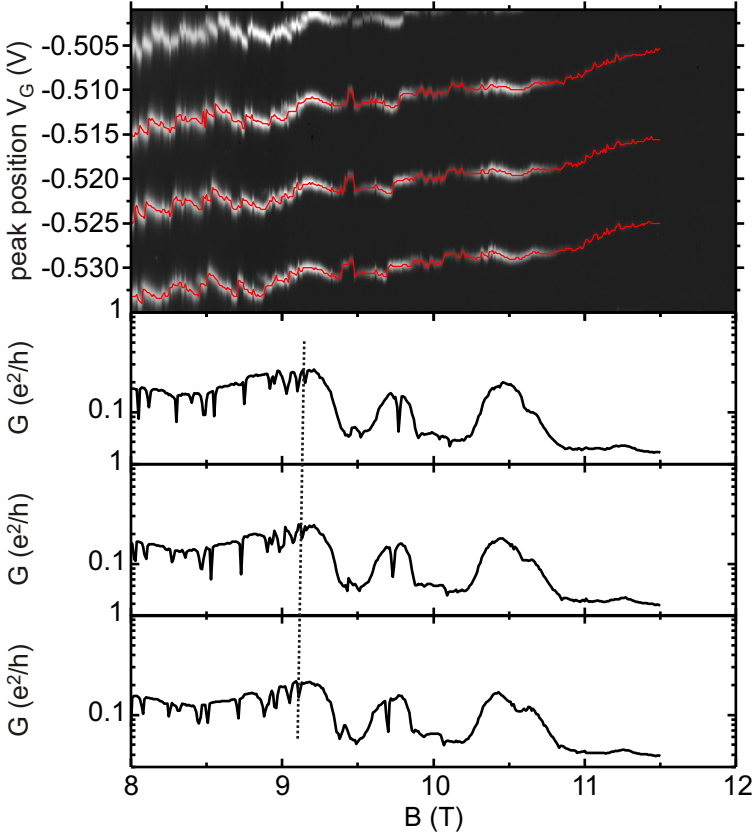


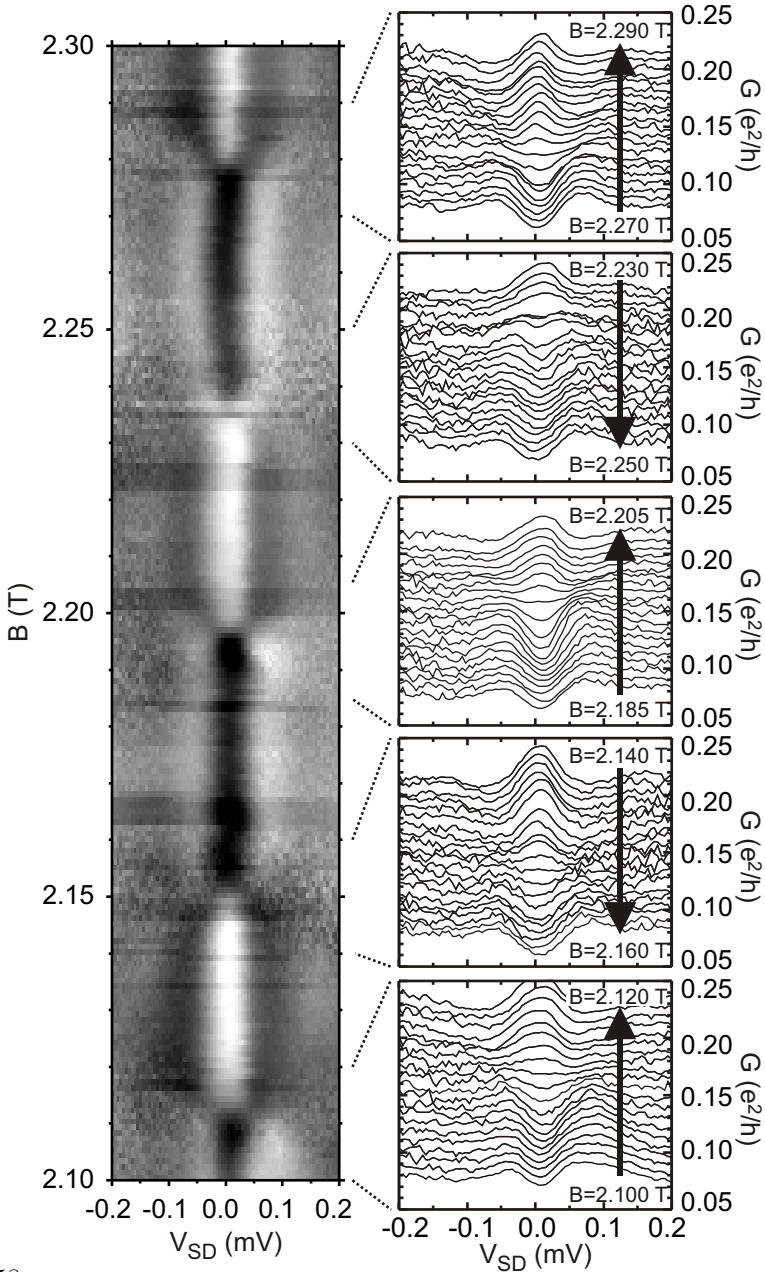
Figure D.1: Coulomb-peak positions and amplitudes versus B at extremely high magnetic fields. The grey scale plot shows the linear conductance on a logarithmic scale from $G = 0.03 e^2/h$ (black) to $0.25 e^2/h$ (white). The dotted line at $B \sim 9.2$ T marks the formation of a maximum density droplet corresponding to $\nu_{dot} = 1$. At still higher magnetic fields we observe transitions to LDD states until in the vicinity of $B = 11.5$ T the signal vanishes.

Figure D.2: (next page) Analysis of the abruptness of the transition between the two situations of a zero-bias and a split Kondo peak. Left: Differential conductance. Right: Cuts along the V_{SD} axis sampled every 1 mT and offset for clarity.

pattern if plotted versus B and V_G in grey scale. In this appendix we present additional data on the transitions between the high- and low-conductance tiles in this regime, i. e. on the transitions between dot ground states exhibiting single and split Kondo peaks.

In Figure D.2 the switching of the Kondo effect as a function of magnetic field is shown. The transition between single-peak and split-peak Kondo effects is obviously very abrupt over a range of a few millitesla. A variation of the splitting at the transition, e. g. a merging of the two peaks, is not observed, although it cannot clearly be ruled out. The single peak seems to vanish while simultaneously the split peaks emerge and vice versa. On the analyzed magnetic field range the splitting of the Kondo peaks in low-conductance tiles is constant. Because of the small magnetic field range a variation due to a changed Zeeman energy would not be visible. The abruptness of the modulation shows that two ground states exhibiting different Kondo effects alternate.

Figure D.3 shows the differential conductance as a function of magnetic field, both for zero bias voltage and at the positions of the split Kondo peaks. For zero bias voltage the transition seems to be sharper than for finite source-drain voltage. This could be due to an increased dephasing at finite bias voltages. Apparently the transition from high- to low- conductance tiles seems to be wider than the opposite transition. The data is not clear enough to reliably analyze these transitions.



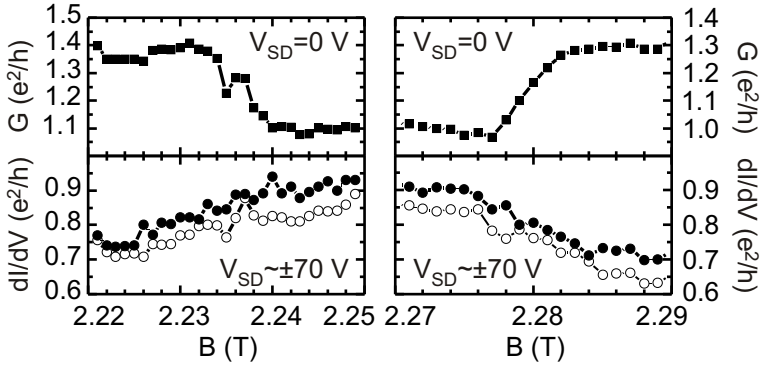


Figure D.3: Differential conductance at zero and finite source-drain bias voltage as marked by the dotted lines in Figure 5.13 as a function of magnetic field. Transitions between high- and low-conductance tiles are shown.

D Additional data on sample 1129-8-7.3

Bibliography

- [1] L. P. Kouwenhoven, C. M. Marcus, P. L. McEuen, S. Tarucha, R. M. Westerveld, and N. S. Wingreen, in *Mesoscopic Electron Transport*, Vol. 345 of *Series E*, edited by L. L. Sohn, L. P. Kouwenhoven, and G. Schön (Kluwer, Dordrecht, 1997), pp. 105–214.
- [2] L. P. Kouwenhoven, D. G. Austing, and S. Tarucha, *Few-electron quantum dots*, Rep. Prog. Phys. **64**, 701 (2001).
- [3] M. A. Kastner, *The single-electron transistor*, Rev. Mod. Phys. **64**, 849 (1992).
- [4] M. A. Nielsen and I. L. Chuang, *Quantum computation and quantum information* (Cambridge University Press, Cambridge, England, 2000).
- [5] D. Loss and D. P. DiVincenzo, *Quantum computation with quantum dots*, Phys. Rev. A **57**, 120 (1998).
- [6] L. M. K. Vandersypen, R. Hanson, L. H. W. van Beveren, J. M. Elzerman, J. S. Greidanus, S. D. Franceschi, and L. P. Kouwenhoven, *Quantum Computing and Quantum Bits in Mesoscopic Systems* (Kluwer, Dordrecht, 2002).
- [7] R. Dingle, H. L. Störmer, A. C. Gossard, and W. Wiegmann, *Electron mobilities in modulation-doped semiconductor heterojunction superlattices*, Appl. Phys. Lett. **33**, 665 (1978).
- [8] T. Ando, A. B. Fowler, and F. Stern, *Electronic properties of two-dimensional systems*, Rev. Mod. Phys. **54**, 437 (1982).

- [9] C. W. J. Beenakker and H. van Houten, in *Solid State Physics*, edited by H. Ehrenreich and D. Turnbull (Academic Press, San Diego, 1991), Vol. 44.
- [10] J. Kondo, *Progr. Theor. Phys.* **32**, 37 (1964).
- [11] L. I. Glazman and M. E. Raikh, *Resonant Kondo transparency of a barrier with quasilocal impurity states*, *JETP Lett.* **47**, 452 (1988).
- [12] T. K. Ng and P. A. Lee, *On-Site Coulomb Repulsion and Resonant Tunneling*, *Phys. Rev. Lett.* **61**, 1768 (1988).
- [13] D. Goldhaber-Gordon, H. Shtrikman, D. Mahalu, D. Abusch-Magder, U. Meirav, and M. A. Kastner, *Kondo effect in a single-electron transistor*, *Nature (London)* **391**, 156 (1998).
- [14] S. M. Cronenwett, T. H. Oosterkamp, and L. P. Kouwenhoven, *A Tunable Kondo Effect in Quantum Dots*, *Science* **281**, 540 (1998).
- [15] J. Schmid, J. Weis, K. Eberl, and K. v. Klitzing, *A quantum dot in the limit of strong coupling to reservoirs*, *Physica B* **256**, 182 (1998).
- [16] F. Simmel, R. H. Blick, J. P. Kotthaus, W. Wegscheider, and M. Bichler, *Anomalous Kondo Effect in a Quantum Dot at Nonzero Bias*, *Phys. Rev. Lett.* **83**, 804 (1999).
- [17] S. Sasaki, S. de Franceschi, J. M. Elzerman, W. G. van der Wiel, M. Eto, S. Tarucha, and L. P. Kouwenhoven, *Kondo effect in an integer-spin quantum dot*, *Nature (London)* **405**, 764 (2000).
- [18] J. Nygård, D. H. Cobden, and P. E. Lindelof, *Kondo physics in carbon nanotubes*, *Nature (London)* **408**, 342 (2000).
- [19] U. Fano, *Effects of Configuration Interaction on Intensities and Phase Shifts*, *Phys. Rev.* **124**, 1866 (1961).
- [20] J. Göres, D. Goldhaber-Gordon, S. Heemeyer, M. A. Kastner, H. Shtrikman, D. Mahalu, and U. Meirav, *Fano resonances in electronic transport through a single-electron transistor*, *Phys. Rev. B* **62**, 2188 (2000).

-
- [21] I. G. Zacharia, D. Goldhaber-Gordon, G. Granger, M. A. Kastner, Y. B. Khavin, H. Shtrikman, D. Mahalu, and U. Meirav, *Temperature dependence of Fano line shapes in a weakly coupled single-electron transistor*, Phys. Rev. B **64**, 155311 (2001).
- [22] U. Meirav and E. B. Foxman, *Single-electron phenomena in semiconductors*, Semicond. Sci. Technol. **11**, 255 (1996).
- [23] J. Weis, *Electrical Transport Through Quantum Dot Systems* (to be published, 2002).
- [24] T. Chakraborty, *Quantum dots: a survey of the properties of artificial atoms*, 1. ed. (Elsevier, Amsterdam, 1999).
- [25] M. A. Kastner, *Transport spectroscopy of a confined electron system under a gate tip*, Physics Today (January) 24 (1993).
- [26] R. C. Ashoori, *Electrons in artificial atoms*, Nature (London) **379**, 413 (1996).
- [27] L. Kouwenhoven and C. Marcus, *Quantum Dots*, Physics World (June) 35 (1998).
- [28] T. A. Fulton and G. J. Dolan, *Observation of Single-Electron Charging Effects in Small Tunnel Junctions*, Phys. Rev. Lett. **59**, 109 (1987).
- [29] U. Meirav, M. A. Kastner, and S. J. Wind, *Single-Electron Charging and Periodic Conductance Resonances in GaAs Nanostructures*, Phys. Rev. Lett. **65**, 771 (1990).
- [30] M. A. Reed, J. N. Randall, R. J. Aggarwall, R. J. Matyi, T. M. Moore, and A. E. Wetsel, *Observation of discrete electronic states in a zero-dimensional semiconductor nanostructure*, Phys. Rev. Lett. **60**, 535 (1988).
- [31] Schwabl, *Quantenmechanik*, 4. Auflage (Springer, Berlin, Heidelberg, New York, 1993).
- [32] V. Fock, Z. Phys. **47**, 446 (1928).

- [33] C. G. Darwin, Proc. Camb. Phil. Soc. **27**, 86 (1930).
- [34] P. L. McEuen, E. B. Foxman, J. Kinaret, U. Meirav, M. A. Kastner, N. S. Wingreen, and S. J. Wind, *Self-consistent addition spectrum of a Coulomb island in the quantum Hall regime*, Phys. Rev. B **45**, 11419 (1992).
- [35] D. B. Chklovskii, B. I. Shklovskii, and L. I. Glazman, *Electrostatics of edge channels*, Phys. Rev. B **46**, 4026 (1992).
- [36] K. Lier and R. R. Gerhardts, *Self-consistent calculations of edge channels in laterally confined two-dimensional electron systems*, Phys. Rev. B **50**, 7757 (1994).
- [37] T. Inoshita, A. Shimizu, Y. Kuramoto, and H. Sakaki, *Correlated electron transport through a quantum dot: The multiple-level effect*, Phys. Rev. B **48**, 14725 (1993).
- [38] S. de Franceschi, S. Sasaki, J. M. Elzerman, W. G. van der Wiel, S. Tarucha, and L. P. Kouwenhoven, *Electron Cotunneling in a Semiconductor Quantum Dot*, Phys. Rev. Lett. **86**, 878 (2001).
- [39] C. W. J. Beenakker, *Theory of Coulomb-blockade oscillations in the conductance of a quantum dot*, Phys. Rev. B **44**, 1646 (1991).
- [40] G. Breit and E. Wigner, *Capture of Slow Neutrons*, Phys. Rev. **49**, 519 (1936).
- [41] E. B. Foxman, U. Meirav, P. L. McEuen, M. A. Kastner, O. Klein, P. A. Beld, and D. M. Abusch, *Crossover from single-level to multilevel transport in artificial atoms*, Phys. Rev. B **50**, 14193 (1994).
- [42] S. Pedersen, *Aharonov-Bohm Experiments in Mesoscopic Systems*, PhD thesis, Ørsted Laboratory, Niels Bohr Institute fAFG, University of Copenhagen, Copenhagen, Denmark, 2001.
- [43] *Properties of Aluminium Gallium Arsenide*, edited by S. Adachi (INSPEC, Gunma University, Japan, 1993).

-
- [44] K. v. Klitzing, G. Dorda, and M. Pepper, *New Method for High-Accuracy Determination of the Fine-Structure Constant Based on Quantized Hall Resistance*, Phys. Rev. Lett. **45**, 494 (1980).
- [45] *Halbleiter-Technologie: Eine Einführung in die Prozesstechnik von Silizium und III-V-Verbindungen*, edited by H. Beneking (Teubner-Verlag, Stuttgart, Germany, 1991).
- [46] M. A. McCord and M. J. Rooks, in *Handbook of microlithography, micromachining and microfabrication*, edited by P. Rai-Choudhury (SPIE Optical Engineering Press, Bellingham, Wash., 1997), pp. 139–249.
- [47] *Introduction to Microlithography*, 2nd ed., edited by L. F. Thompson, C. G. Willson, and M. J. Bowden (American Chemical Society, Washington, DC, 1994).
- [48] F. Pobell, *Matter and Methods at Low Temperatures*, 2nd ed. (Springer, Berlin, Heidelberg, New York, 1996).
- [49] J. Weis, R. J. Haug, K. v. Klitzing, and K. Ploog, *Transport spectroscopy of a confined electron system under a gate tip*, Phys. Rev. B **46**, 12837 (1992).
- [50] Y. Y. Wei, J. Weis, K. v. Klitzing, and K. Eberl, *Single-electron transistor as an electrometer measuring chemical potential variations*, Appl. Phys. Lett. **71**, 2514 (1997).
- [51] P. C. Main, A. S. G. Thornton, R. J. A. Hill, S. T. Stoddart, T. Ihn, L. Eaves, K. A. Benedict, and M. Henini, *Landau-Level Spectroscopy of a Two-Dimensional Electron System by Tunneling through a Quantum Dot*, Phys. Rev. Lett. **84**, 729 (2000).
- [52] M. Ciorga, A. S. Sachrajda, P. Hawrylak, C. Gould, P. Zawadzki, S. Jullian, Y. Feng, and Z. Wasilewski, *Addition spectrum of a lateral dot from Coulomb and spin-blockade spectroscopy*, Phys. Rev. B **61**, R16315 (2000).
- [53] P. L. McEuen, E. B. Foxman, U. Meirav, M. A. Kastner, Y. Meir, and N. S. Wingreen, *Transport spectroscopy of a Coulomb island in the quantum Hall regime*, Phys. Rev. Lett. **66**, 1926 (1991).

- [54] P. Hawrylak, C. Gould, A. Sachrajda, Y. Feng, and Z. Wasilewski, *Collapse of the Zeeman gap in quantum dots due to electronic correlations*, Phys. Rev. B **59**, 2801 (1999).
- [55] M. Keller, *Der Kondo-Effekt in Quantendots bei hohen Magnetfeldern*, PhD thesis, Max-Planck-Institut für Festkörperforschung, Stuttgart, Germany, 2001.
- [56] J. Schmid, J. Weis, K. Eberl, and K. v. Klitzing, *Absence of Odd-Even Parity Behavior for Kondo Resonances in Quantum Dots*, Phys. Rev. Lett. **84**, 5824 (2000).
- [57] U. F. Keyser, *Nanolithography with an atomic force microscope: quantum point contacts, quantum dots and quantum rings*, PhD thesis, Universität Hannover, 2002.
- [58] T. Heinzel, D. A. Wharam, J. P. Kotthaus, G. Böhm, W. Klein, G. Tränkle, and G. Weimann, *Periodic modulation of Coulomb-blockade oscillations in high magnetic fields*, Phys. Rev. B **50**, 15113 (1994).
- [59] M. Ciorga (unpublished).
- [60] A. H. MacDonald, S. R. E. Yang, and M. D. Johnson, *Quantum Dots in Strong Magnetic Field: Stability Criteria for the Maximum Density Droplet*, Aust. J. Phys. **46**, 345 (1993).
- [61] C. de C. Chamon and X. G. Wen, *Sharp and smooth boundaries of quantum Hall liquids*, Phys. Rev. B **49**, 8227 (1994).
- [62] O. Klein, C. de C. Chamon, D. Tang, D. M. Abusch-Magder, U. Meirav, X. G. Wen, and M. A. Kastner, *Exchange Effects in an Artificial Atom at High Magnetic Fields*, Phys. Rev. Lett. **74**, 785 (1995).
- [63] O. Klein, D. Goldhaber-Gordon, C. de C. Chamon, and M. A. Kastner, *Magnetic-field dependence of the level spacing of a small electron droplet*, Phys. Rev. B **53**, 4221 (1996).

- [64] T. H. Oosterkamp, J. W. Janssen, L. P. Kouwenhoven, D. G. Austing, T. Konda, and S. Tarucha, *Maximum-Density Droplet and Charge Redistributions in Quantum Dots at High Magnetic Fields*, Phys. Rev. Lett. **82**, 2931 (1999).
- [65] A. S. Edelstein, in *Encyclopedia of Physics*, 2nd edition, edited by R. G. Lerner *et al.* (VCH Publishers, New York, NY and others, 1991), p. 608.
- [66] L. P. Kouwenhoven and L. I. Glazman, *Revival of the Kondo effect*, Phys. World 33 (January 2001).
- [67] J. P. Franck, F. D. Manchester, and D. L. Martin, Proc. Roy. Soc. **A263**, 494 (1961).
- [68] K. G. Wilson, Rev. Mod. Phys. **47**, 773 (1975).
- [69] H. Bethe, Z. Phys. **71**, 205 (1931).
- [70] N. Andrei, *Diagonalization of the Kondo Hamiltonian*, Phys. Rev. Lett. **45**, 379 (1980).
- [71] P. B. Wiegmann, JETP Lett. **31**, 392 (1980).
- [72] A. C. Hewson, *The Kondo Problem to Heavy Fermions* (Cambridge University Press, Cambridge, UK, 1993).
- [73] G. D. Mahan, *Many-Particle Physics*, 3rd ed. (Kluwer Academic/Plenum Publishers, New York, USA, 2000).
- [74] P. W. Anderson, *Localized Magnetic States in Metals*, Phys. Rev. **124**, 41 (1961).
- [75] J. R. Schrieffer and P. A. Wolff, *Relation between the Anderson and Kondo Hamiltonians*, Phys. Rev. **149**, 491 (1966).
- [76] F. D. M. Haldane, *Scaling Theory of the Asymmetric Anderson Model*, Phys. Rev. Lett. **40**, 416 (1978).
- [77] J. D. Schmid, *The Kondo Effect in Quantum Dots*, PhD thesis, Max-Planck-Institut für Festkörperforschung, Stuttgart, Germany, 2000.

- [78] A. Kawabata, *On the Electron Transport through a Quantum Dot*, J. Phys. Soc. Japan **60**, 3222 (1991).
- [79] D. C. Ralph and R. A. Buhrman, *Observations of Kondo Scattering without Magnetic Impurities: A Point Contact Study of Two-Level Tunneling Systems in Metals*, Phys. Rev. Lett. **69**, 2118 (1992).
- [80] A. L. Yeyati, F. Flores, and A. Martín-Rodero, *Transport in Multilevel Quantum Dots: From the Kondo Effect to the Coulomb Blockade Regime*, Phys. Rev. Lett. **83**, 600 (1999).
- [81] J. Park, A. N. Pasupathy, J. I. Goldsmith, C. Chang, Y. Yaish, J. R. Petta, M. Rinkoski, J. P. Sethna, H. D. Abruña, P. L. McEuen, and D. C. Ralph, *Coulomb blockade and the Kondo effect in single-atom transistors*, Nature (London) **417**, 722 (2002).
- [82] W. G. van der Wiel, S. de Franceschi, T. Fujisawa, J. M. Elzerman, S. Tarucha, and L. P. Kouwenhoven, *The Kondo Effect in the Unitary Limit*, Science **289**, 2105 (2000).
- [83] Y. Meir, N. S. Wingreen, and P. A. Lee, *Low-Temperature Transport Through a Quantum Dot: The Anderson Model Out of Equilibrium*, Phys. Rev. Lett. **70**, 2601 (1993).
- [84] N. S. Wingreen and Y. Meir, *Anderson model out of equilibrium: Noncrossing-approximation approach to transport through a quantum dot*, Phys. Rev. B **49**, 11040 (1994).
- [85] J. König, H. Schoeller, and G. Schön, *Zero-Bias Anomalies and Boson-Assisted Tunneling Through Quantum Dots*, Phys. Rev. Lett. **76**, 1715 (1996).
- [86] J. König, J. Schmid, H. Schoeller, and G. Schön, *Resonant tunneling through ultrasmall quantum dots: Zero-bias anomalies, magnetic-field dependence, and boson-assisted transport*, Phys. Rev. B **54**, 16820 (1996).
- [87] T. A. Costi, A. C. Hewson, and V. Zlatić, *Transport coefficients of the Anderson model via the numerical renormalization group*, J. Phys.: Condens. Matter **6**, 2519 (1994).

- [88] A. L. Chudnovskiy and S. E. Ulloa, *Kondo and mixed-valence regimes in multilevel quantum dots*, Phys. Rev. B **63**, 165316 (2001).
- [89] D. Goldhaber-Gordon, J. Göres, M. A. Kastner, H. Shtrikman, D. Mahalu, and U. Meirav, *From the Kondo Regime to the Mixed-Valence Regime in a Single-Electron Transistor*, Phys. Rev. Lett. **81**, 5225 (1998).
- [90] T. A. Costi, *Kondo Effect in a Magnetic Field and the Magnetoresistivity of Kondo Alloys*, Phys. Rev. Lett. **85**, 1504 (2000).
- [91] S. Tarucha, D. G. Austing, Y. Tokura, W. G. van der Wiel, and L. P. Kouwenhoven, *Direct Coulomb and Exchange Interaction in Artificial Atoms*, Phys. Rev. Lett. **84**, 2485 (2000).
- [92] W. Hofstetter and H. Schoeller, *Quantum Phase Transition in a Multilevel Dot*, Phys. Rev. Lett. **88**, 016803 (2002).
- [93] W. G. van der Wiel, S. de Franceschi, J. M. Elzerman, S. Tarucha, L. P. Kouwenhoven, J. Motohisa, F. Nakajima, and T. Fukui, *Two-stage Kondo effect in a Quantum Dot at High Magnetic Field*, Phys. Rev. Lett. **88**, 126803 (2002).
- [94] M. Pustilnik and L. I. Glazman, *Kondo Effect in Real Quantum Dots*, Phys. Rev. Lett. **87**, 216601 (2001).
- [95] D. Giuliano and A. Tagliacozzo, *Spin Fractionalization of an Even Number of Electrons in a Quantum Dot*, Phys. Rev. Lett. **84**, 4677 (2000).
- [96] M. Pustilnik, Y. Avishai, and K. Kikoin, *Quantum Dots with Even Number of Electrons: Kondo Effect in a Finite Magnetic Field*, Phys. Rev. Lett. **84**, 1756 (2000).
- [97] M. Pustilnik and L. I. Glazman, *Conduction through a Quantum Dot near a Singlet-Triplet Transition*, Phys. Rev. Lett. **85**, 2993 (2000).
- [98] M. Pustilnik and L. I. Glazman, *Kondo effect induced by a magnetic field*, Phys. Rev. B **64**, 045328 (2001).

- [99] M. Eto and Y. V. Nazarov, *Enhancement of Kondo Effect in Quantum Dots with an Even Number of Electrons*, Phys. Rev. Lett. **85**, 1306 (2000).
- [100] W. Izumida, O. Sakai, and S. Tarucha, *Tunneling through a Quantum Dot in Local Spin Singlet-Triplet Crossover Region with Kondo Effect*, Phys. Rev. Lett. **87**, 216803 (2001).
- [101] C. Tejedor and L. Martín-Moreno, *Kondo effect in multielectron quantum dots at high magnetic fields*, Phys. Rev. B **63**, 035319 (2001).
- [102] C. Tejedor and L. Martín-Moreno, *Chessboard magnetoconductance of a quantum dot in the Kondo regime*, cond-mat/0203115 (2002).
- [103] M. Keller, U. Wilhelm, J. Schmid, J. Weis, K. v. Klitzing, and K. Eberl, *Quantum dot in high magnetic fields: Correlated tunneling of electrons probes the spin configuration at the edge of the dot*, Phys. Rev. B **64**, 033302 (2001).
- [104] C. Fühner, U. F. Keyser, R. J. Haug, D. Reuter, and A. D. Wieck, *Flux-quantum-modulated Kondo conductance in a multielectron quantum dot*, Phys. Rev. B **66**, 161305(R) (2002).
- [105] M. A. Kastner and D. Goldhaber-Gordon, *Kondo physics with single electron transistors*, Solid State Communications **119**, 245 (2001).
- [106] J. Kroha (unpublished).
- [107] A. Rosch, J. Kroha, and P. Wölfle, *Kondo Effect in Quantum Dots at High Voltage: Universality and Scaling*, Phys. Rev. Lett. **87**, 156802 (2001).
- [108] S. Ulloa (unpublished).
- [109] M. Stopa (unpublished).
- [110] U. Fano and J. W. Cooper, *Line Profiles in the Far-uv Absorption Spectra of the Rare Gases*, Phys. Rev. **137**, A1364 (1965).

-
- [111] J. A. Simpson and U. Fano, *Classification of Resonances in the Electron Scattering Cross Section of Ne and He*, Phys. Rev. Lett. **11**, 158 (1963).
- [112] F. Cerdeira, T. A. Fjeldly, and M. Cardona, *Effect of Free Carriers on Zone-Center Vibrational Modes in Heavily Doped p-type Si. II. Optical Modes*, Phys. Rev. B **8**, 4734 (1973).
- [113] J. Faist, F. Capasso, C. Sirtori, K. W. West, and L. N. Pfeiffer, *Controlling the sign of quantum interference by tunnelling from quantum wells*, Nature (London) **390**, 589 (1997).
- [114] H. Schmidt, K. L. Campman, A. C. Gossard, and A. Imamoglu, *Tunneling induced transparency: Fano interference in intersubband transitions*, Appl. Phys. Lett. **70**, 3455 (1997).
- [115] V. Madhavan, W. Chen, T. Jamneala, M. F. Crommie, and N. S. Wingreen, *Tunneling into a Single Magnetic Atom: Spectroscopic Evidence of the Kondo Resonance*, Science **280**, 567 (1998).
- [116] R. Landauer, *Electrical transport in open and closed systems*, Z. Phys. B **68**, 217 (1987).
- [117] M. Büttiker, IBM J. Res. Dev. **32**, 63 (1988).
- [118] J. U. Nöckel and A. D. Stone, *Resonance line shapes in quasi-one-dimensional scattering*, Phys. Rev. B **50**, 17415 (1994).
- [119] Y. Aharonov and D. Bohm, *Significance of Electromagnetic Potentials in the Quantum Theory*, Phys. Rev. **115**, 485 (1959).
- [120] K. Kobayashi, H. Aikawa, S. Katsumoto, and Y. Iye, *Tuning of the Fano Effect through a Quantum Dot in an Aharonov-Bohm Interferometer*, Phys. Rev. Lett. **88**, 256806 (2002).
- [121] A. Yacoby, M. Heiblum, D. Mahalu, and H. Shtrikman, *Coherence and Phase Sensitive Measurements in a Quantum Dot*, Phys. Rev. Lett. **74**, 4047 (1995).

- [122] R. Schuster, E. Buks, M. Heiblum, D. Mahalu, V. Umansky, and H. Shtrikman, *Phase measurement in a quantum dot via a double-slit interference experiment*, Nature (London) **385**, 417 (1997).
- [123] Y. Ji, M. Heiblum, D. Sprinzak, D. Mahalu, and H. Shtrikman, *Phase Evolution in a Kondo correlated system*, Science **290**, 779 (2000).
- [124] Y. Ji, M. Heiblum, and H. Shtrikman, *Transmission Phase of a Quantum Dot with Kondo Correlation near the Unitary Limit*, Phys. Rev. Lett. **88**, 076601 (2002).
- [125] A. Fuhrer, S. Lüscher, T. Ihn, T. Heinzel, K. Ensslin, W. Wegscheider, and M. Bichler, *Energy spectra of quantum rings*, Nature (London) **413**, 822 (2001).
- [126] U. F. Keyser, C. Fühner, S. Borck, R. J. Haug, M. Bichler, G. Abstreiter, and W. Wegscheider, *Kondo effect in a few-electron quantum ring*, cond-mat/0206262 (2002).
- [127] K. Kobayashi, H. Aikawa, S. Katsumoto, and Y. Iye, in *Proceedings of the 26th International Conference on the Physics of Semiconductors*, Institute of Physics (IoP, 2002).
- [128] U. Gerland, J. von Delft, T. A. Costi, and Y. Oreg, *Transmission Phase Shift of a Quantum Dot with Kondo Correlations*, Phys. Rev. Lett. **84**, 3710 (2000).
- [129] W. Hofstetter, J. König, and H. Schoeller, *Kondo Correlations and the Fano Effect in Closed Aharonov-Bohm Interferometers*, Phys. Rev. Lett. **87**, 156803 (2001).
- [130] H. L. Störmer, A. C. Gossard, and W. Wiegmann, *Observation of intersubband scattering in a 2-dimensional electron system*, Solid State Commun. **41**, 707 (1982).
- [131] N. Maire (unpublished).

- [132] G. L. Snider, I.-H. Tan, and E. L. Hu, *Electron states in mesa-etched one-dimensional quantum well wires*, J. of Applied Physics **66**, 2849 (1990).
- [133] I.-H. Tan, G. L. Snider, and E. L. Hu, *A self-consistent solution of Schrödinger-Poisson equations using a nonuniform mesh*, J. of Applied Physics **66**, 4071 (1990).
- [134] G. L. Snider, *1D Schrödinger-Poisson solver*, Department of Electrical Engineering, University of Notre Dame, Notre Dame, IN, 2002 (<http://www.nd.edu/~gsnider/>).
- [135] A. Kumar, *Self-consistent calculations on confined electrons in three-dimensional geometries*, Surface Science **263**, 335 (1992).

Bibliography

Danksagung

Diese Arbeit wäre ohne die Unterstützung einer Vielzahl von Personen nicht zustande gekommen. Meinem Doktorvater Prof. Dr. R. J. Haug danke ich für die Möglichkeit, in seiner Gruppe zu promovieren. Seine engagierte Betreuung und seine wichtigen Anregungen haben diese Arbeit sehr bereichert. Prof. Dr. M. Oestreich danke ich für die Übernahme des Koreferats.

“Die Bochumer” um Dr. D. Reuter und Prof. Dr. A. D. Wieck haben mit hochwertigen Heterostrukturen eine tragfähige Basis für meine Experimente geschaffen. In die Geheimnisse der Elektronenstrahl-Lithographie haben mich an der PTB Martin Blöcker und Dr. F. Ahlers eingeweiht. M. Stopa hat sich spontan bereit erklärt, die Ladungsverteilung in meinen Proben zu simulieren. Ihnen allen gilt mein Dank.

Meinem Mitstreiter Dr. U. F. Keyser im “Kon+do”-Team bin ich zu besonderem Dank verpflichtet. Die vielen Diskussionen mit ihm, seine ständigen guten Fragen und seine Hilfe waren für das Gelingen dieser Arbeit sehr wertvoll.

Universitär Hoofdcent Dr. Uli Zeitler und Dr. Frank Hohls danke ich für interessante Diskussionen und ihre kompetente Hilfe in technisch-experimentellen wie physikalischen Fragen sowie für die Durchsicht des Manuskriptes (F. H.). Für das Korrekturlesen möchte ich mich auch bei Dr. Isabella Hapke-Wurst bedanken. Niels Maire hat mir mit der Durchführung einiger Messungen zur Besetzung des zweiten Subbandes geholfen.

Für die gute Infrastruktur in der Abteilung Nanostrukturen möchte ich Yvonne Griep im Sekretariat und Klara Tetzlaff in der Heliumversorgung besonders danken. Auch die Mitarbeiter der Feinmechanikwerkstatt, stellvertretend seien Herr Lehmann und Herr Klaus genannt, standen mir stets mit Rat und Tat zur Seite.

Die ausgezeichnete Arbeitsatmosphäre im Institut ist neben den schon genannten “lieben Kollegen” auch den “Ados” P. König, H. W. Schumacher und P. Hullmann, T. Schmidt, den “JuDos” A. Nauen und J. Regul sowie J. Köneman, K.-M. Händel, J.-M. Becker, G. Sukhodub, F. Schulze-Wischeler, C. Fricke, A. Mühle und M. Rogge zu verdanken.

Vor allem gilt mein Dank meinen Eltern und meinem Bruder Thomas für ihre finanzielle und ideelle Unterstützung. Ihnen widme ich diese Dissertation.